2013

Crystal Growth and an Investigation of Structural Stability: Synthesis, Structure, and Physical Properties of Yb(Mn,M)xAl12-x (M = Fe, Ru; x < 2.5) and LnMnxGa3 (Ln = Ho-Tm; x < 0.15)

Bradford Wesley Fulfer
Louisiana State University and Agricultural and Mechanical College, bfulfe1@lsu.edu

CRYSTAL GROWTH AND AN INVESTIGATION OF STRUCTURAL STABILITY: SYNTHESIS, STRUCTURE, AND PHYSICAL PROPERTIES OF $Yb(Mn,M)_xAl_{12-x}$ (M = Fe, Ru; $x < 2.5$) AND $LnMn_xGa_3$ (Ln = Ho-Tm; $x < 0.15$)

A Dissertation

Submitted to the Graduate Faculty of the
Louisiana State University and
Agricultural and Mechanical College
in partial fulfillment of the
requirements for the degree of
Doctor of Philosophy

in

The Department of Chemistry

by
Bradford Wesley Fulfer
B.S., Abilene Christian University, 2004
August 2013

To my family, thank you for your unconditional love and support.
To my incredible wife Kristen, thank you for bearing with me and loving me. I do not have words to express what you mean to me.
To GOD, thank you for the overwhelming abundance of blessing that is my life.

ACKNOWLEDGEMENTS

Throughout my graduate career there have been many people who have positively impacted my studies and my life. At this point I wish to acknowledge these people.

To my father and mother, Ken and Cindy Fulfer, I wish to express a lifetime of gratitude. Through their constant teaching, guidance, and support I am here today. I would not be the person I am today without them. I also wish to acknowledge my brother Bryant Fulfer, for the constant companionship and camaraderie he has provided to me as only a brother can. To my uncle, Danny L. Mann Jr., thank you for your support. I'll always appreciate my "blind old uncle" for being a constant source of insight and wisdom, and levity.

Special thanks are reserved for my research advisor Dr. Julia Y Chan. I would not be where I am today if it were not for her patience, guidance, and advice. She allowed me to grow and learn as a scientist, and where other people might have given up on me, she continued to push me to achieve my goal of obtaining a Ph.D. She has allowed me to present my results on numerous occasions, the most notable occasions being at the national meeting of the American Crystallography Association in New Orleans in the summer of 2011, the Gordon Research Conference for Solid State Chemistry at Colby Sawyer College in New Hampshire in the summer of 2012, and the national meeting of the American Chemical Society in New Orleans in the spring of 2013. These opportunities challenged me and helped introduce me to the wide world of solid state chemistry, and I am very grateful for them. Finally, she provided countless opportunities for me to identify my calling, which I believe to be teaching. By encouraging me to participate in chem. demos, presentations, and by even allowing me on a few occasions to help her teach some of her classes, she opened my eyes to teaching. For all these reasons, and for

many more, I am deeply grateful. I wish her the very best in the future as she begins a new phase of her career in Dallas.

There are multiple people in the Chemistry and Physics departments at LSU who have helped me immensely during my time here. Thanks to my committee members Drs. George Stanley, Andrew Maverick, and David P. Young, for their patience and professionalism through all the different submissions of various paperwork and documents. Special thanks go to my collaborators: Dr. Frank Fronczek (Chemistry, LSU) who is a boundless source of information about crystallography, Dr. Gregory McCandless (Chemistry, LSU) who has on many occasions assisted me with crystallographic data collection as well as structural modeling and refinement, and Drs. David P. Young (Physics, LSU), Shane Stadler (Physics, LSU), and John DiTusa (Physics, LSU), for multiple collaborative opportunities that have enriched me scientifically. Special thanks are also in order for Dr. Neel Haldolaarachchige and Joseph Prestigiacomo for their invaluable assistance with the measurements of electrical and magnetic properties for many of my compounds.

Finally, my enduring and heartfelt thanks go out to many former and current members of Dr. Chan's research group, or "Chanites" as we have been entitled. I sincerely thank Drs. Melissa Menard, Brenton Drake, W. Adam Phelan, and Michael Kangas for setting examples for me when I first joined the group. They initiated me into the realm of solid state chemistry and patiently showed me what good research looks like. For Dr. Devin C. Schmitt and (soon-to-be Dr.) Gregory Morrison are reserved my deepest and most heartfelt gratitude. I count them as respected colleagues, but also as brothers and friends. I will never forget the many ways they have enriched my life scientifically and personally, and I will forever be grateful for them. To the current members of the Chan group LaRico Treadwell, Pilanda McDougald, and Luis Reyes,

thank you for your questions and companionship. You “newbies” have taught me that you only truly understand something when you can explain it to someone else. Last, but certainly not least, my sincere thanks go to “Young” Jacob McAplin, my close coworker and friend. His synthetic work has been invaluable to me, and I am indebted to him for how he has helped me throughout my career at LSU.

TABLE OF CONTENTS

ABSTRACT

The contents of this dissertation describe the crystal growth, crystal structures, and physical properties of ternary intermetallic aluminides and gallides. These compounds are grown in an effort to determine how controlling reaction ratios using the flux growth method can impact chemical structure and physical properties. Three specific examples are given where slight changes in reaction ratios leads to crystalline products that adopt various structure types.

Ln$Mn_{2+x}Al_{10-x}$ (*Ln* = Gd, Yb) crystals adopt the $CaCr_2Al_{10}$ and $ThMn_{12}$ structure types. We compare *Ln*$Mn_{2+x}Al_{10-x}$ compounds adopting the $CaCr_2Al_{10}$ and $ThMn_{12}$ structure types, and outline synthesis methods to obtain each polymorph. Magnetic susceptibility measurements show paramagnetic behavior down to 3 K for both $CaCr_2Al_{10}$- and $ThMn_{12}$-type compounds, with observed magnetic moments of 1.3 μ_B for compounds adopting the $CaCr_2Al_{10}$ structure type to 4.2 μ_B for those adopting the $ThMn_{12}$ structure type. Compounds of both structure type exhibit metallic resistivity, with upturns at low temperature attributed to Kondo scattering.

Single crystals of $Yb(Mn,M)_xAl_{12-x}$ (M = Fe, Ru; $x \leq 2.5$) adopt three structure types, the $ThMn_{12}$ structure type, and two structural derivatives, the $CaCr_2Al_{10}$ structure type and the $YbFe_2Al_{10}$ structure type, depending on the starting amount of Mn relative to M. We outline the synthetic parameters used to obtain products in all three structure types and specifically address how stabilizing products in one structure type over another is a function of Mn:M reaction ratios. $Yb(Mn,Fe)_xAl_{12-x}$ compounds exhibit paramagnetic behavior down to 2 K, as well as metallic resistivity down to ~ 50 K. Below 50 K, $Yb(Mn,Fe)_xAl_{12-x}$ compounds exhibit upturns in resistivity that indicate the onset of Kondo interactions.

Finally, single crystals of $LnMn_xGa_3$ (Ln = Ho-Tm; $0 < x < 0.15$) crystallize in a variant of the $AuCu_3$ structure type (space group $Pm\bar{3}m$) where Mn partially occupies the body center of

the unit cell. These "stuffed" $AuCu_3$-type $LnMn_xGa_3$ compounds are presented as intermediates between $AuCu_3$- and Y_4PdGa_{12}-type compounds. $HoMn_xGa_3$ and $ErMn_xGa_3$ order antiferromagnetically, with effective moments decreasing as a function of Mn concentration and T_N increasing as a function of Mn concentration. $TmGa_3$ orders antiferromagnetically at ~ 4.2 K while $TmMn_xGa_3$ ($x > 0$) are paramagnetic down to 1.8 K.

CHAPTER 1: INTRODUCTION

Solid state and materials chemistry is a broad field of chemistry that continues to garner increasing interest worldwide. From a historical perspective, research in solid state chemistry has been driven by technological demands, like the development of metal tools in early human history, or more recently the development and utilization of ultra high purity silicon. This connection between solid state chemistry and technological advancement continues to make research in the field exciting and relevant. Topics such as high temperature superconductivity, the thermoelectric effect, and the magnetocaloric effect ensure that research in the field of solid state chemistry remains significant in the development of new technologies.

Materials in the solid state generally fall into two categories; amorphous or non-crystalline solids, where there is no long-range structural order, and crystalline solids, which exhibit long-range structural order. Crystalline solids may be further categorized into polycrystalline and single-crystalline solids. Polycrystalline solids consist of multiple small crystals arranged in various orientations throughout a given sample, whereas in single-crystalline samples the periodicity of the crystal structure is unbroken through the entire sample. Grain boundaries, dislocations, and other crystal defects are present in large amounts for polycrystalline solids and are present in very small amounts for single-crystalline samples. The importance, then, of obtaining single-crystalline materials lies in uncovering the intrinsic physical characteristics of a given solid material. Crystal defects, if they are present in sufficient quantities as in polycrystalline materials, can have a large effect on the physical properties of a given system. If the crystalline defects are minimized, as they are for single-crystalline materials, the physical properties of a given sample may then be attributed solely to the phase. By uncovering the intrinsic physical properties of a given solid in its single-crystalline form,

inferences may be made to correlate the properties of that material to certain aspects of its structure. The growth of single crystals is often necessary when a new structure type is discovered to determine the intrinsic properties of materials. Thus, structure-property relationships are discovered, and desirable properties may then be sought by targeting specific structural motifs in known crystal structures or by identifying similar structural motifs in new crystal structures. In this fashion, the growth of high quality crystalline materials fuels discovery and advancement in areas such as condensed-matter physics and the development and improvement of materials-based technologies.

The need for single-crystalline materials was highlighted in a report published in 2009 by the National Research Council of The National Academies.[1] The report identified the growth of single-crystalline materials as an extremely important component of research in condensed-matter physics and also addressed the decline of discovery and growth of crystalline matter in United States industry and academia as detrimental technological and economic progress. Finally, multiple recommendations were made to encourage further discovery and synthetic efforts in the United States. These recommendations included ideas such as increasing funding for crystal growth in a coordinated fashion across multiple government funding agencies, developing multidisciplinary centers focused on the discovery and growth of crystalline matter, and cultivating training programs in the discovery and growth of crystalline matter.

The demand for high quality crystalline materials and the study of structural preferences sets the scope for the body of work presented in this dissertation. Given the importance of single-crystalline materials in the advancement of condensed-matter physics and technology, there remain multiple challenges in the field of crystal growth. One key challenge for crystal growers is predicting how synthetic variables, such as reaction ratios or temperature parameters,

will affect the formation of crystalline products. In order to synthesize a specific material with a specific atomic composition and arrangement, many different parameters must be accounted for, and variability in any of those parameters may alter the results of the synthesis. The work presented here may be described as a study in the effect of changing reaction parameters, specifically, reaction ratios, on the formation of crystalline solids. Three examples will be given to illustrate the effects that changing these reaction parameters can have on the resultant crystalline products. All of these examples concern the synthesis of intermetallic crystals containing lanthanide elements, transition metals, and main group elements. Lanthanides are typically incorporated into intermetallic compounds due to their propensity to exhibit interesting magnetic or electronic phenomena, while transition metals may or may not be magnetic in intermetallic compounds.

The first example involves Ln-Mn-Al (Ln = Gd, Yb) compounds crystallizing in the closely related $ThMn_{12}$[2] and $CaCr_2Al_{10}$[3] structure types. The $CaCr_2Al_{10}$ structure type may be viewed as a substitutional derivative of the $ThMn_{12}$ structure type, and we demonstrate that compounds in one structure type may be preferentially obtained over compounds in the other structure type based on the amount of Mn in the reaction ratio. We show that these subtle changes in the structures of the products are also reflected in the magnetic properties of these compounds.

For the second example we examine the effects of adding a second transition metal such as Fe or Ru to the $Ln(M,Al)_{12}$. These compounds crystallize in the $ThMn_{12}$ and $CaCr_2Al_{10}$ structure types, and also in the structurally related $YbFe_2Al_{10}$[4] structure type. The structure types adopted by the various products are determined specifically by the reaction ratio of Mn to either Fe or Ru, with reaction ratios containing more Fe or Ru crystallizing in the $YbFe_2Al_{10}$

structure type, and reaction ratios containing more Mn crystallizing in the $ThMn_{12}$ or $CaCr_2Al_{10}$ structure types.

The final example involves $LnMn_xGa_3$ (Ln = Ho-Tm) compounds. By changing the amount of Mn in the reaction ratios we may synthesize crystals of $LnMn_xGa_3$ in the $AuCu_3$[5] structure type or in a variant of the $AuCu_3$ structure type. These variants of the $AuCu_3$ structure type contain Mn which is "stuffed" in an octahedral hole in the body center of the unit cell. These "stuffed" compounds represent a middle ground between $LnGa_3$ compounds adopting the $AuCu_3$ structure type, and Ln_4MGa_{12} (M = Cr, Fe)[6-7] compounds adopting the Y_4PdGa_{12}[8] structure type. The magnetic properties of these stuffed compounds are different from those of the $LnGa_3$ as a result of the large degree of local disorder created by the incorporation of Mn into the $LnGa_3$ structure.

The growth method of choice for the crystals discussed in this document is the flux growth technique. In flux growth synthesis, metallic or metalloid elements that melt at relatively low temperatures such as aluminum (m.p. 660 °C), gallium (m.p. 29 °C), tin (m.p. 232 °C), lead (m.p. 327 °C), etc., are employed as solvents for all other metals in the reaction. When the flux metal melts, it facilitates diffusion of other elements that melt at much higher temperatures. The flux growth method has several key advantages over other solid state synthesis techniques. One advantage is that the relatively low temperatures employed in flux growth allow for the growth of compounds via kinetically dominated pathways, rather than thermodynamically dominated pathways. This means that products obtained from metal fluxes may not be otherwise obtained using higher temperature synthesis. Additionally, the rapid heating and cooling associated with high temperature synthesis methods leads to the formation of polycrystalline samples, whereas single crystals may be easily obtained from molten metal fluxes.

Using the flux growth technique, we explore the phase stability of lanthanide- and transition metal-containing aluminide and gallide intermetallic compounds of the $ThMn_{12}$, $CaCr_2Al_{10}$, $YbFe_2Al_{10}$, and $AuCu_3$ structure types. The flux growth technique allows us to study the structural competition between compounds as a function of reaction stoichiometry, and also allows us to grow relatively large single crystals. We may then investigate the magnetic and electrical transport properties of these compounds to draw general conclusions about how subtle changes in reaction ratios influence the formation of compounds in the solid state, and how subtle differences in structure or chemical composition correlate to the physical properties of those compounds.

References

(1) Council, N. R. *Frontiers in Crystalline Matter: From Discovery to Technology*; The National Academies Press: Washington, DC, 2009.

(2) Florio, J. V.; Rundle, R. E.; Snow, A. I. *Acta Cryst.* **1952**, *5*, 449.

(3) Cordier, G.; Czech, E.; Ochmann, H.; Schäfer, H. *J. Less-Common Met.* **1984**, *99*, 173.

(4) Niemann, S.; Jeitschko, W. *Z. Kristallogr.* **1995**, *210*, 338.

(5) Sedstrom, E. *Ann. Phys-Berlin* **1924**, *75*, 549.

(6) Slater, B. R.; Bie, H.; Stoyko, S. S.; Bauer, E. D.; Thompson, J. D.; Mar, A. *J. Solid State Chem.* **2012**, *196*, 409.

(7) Drake, B. L.; Grandjean, F.; Kangas, M. J.; Okudzeto, E. K.; Karki, A. B.; Sougrati, M. T.; Young, D. P.; Long, G. J.; Chan, J. Y. *Inorg. Chem.* **2010**, *49*, 445.

(8) Vasilenko, L. O.; Noga, A. S.; Grin, Y. N.; Koterlin, M. D.; Yarmolyuk, Y. P. *Russ. Metall.* **1988**, 216.

CHAPTER 2. CRYSTAL GROWTH AND MAGNETIC PROPERTIES OF Ln-Mn-Al (Ln = Gd, Yb) COMPOUNDS OF THE $CaCr_2Al_{10}$ AND $ThMn_{12}$ STRUCTURE TYPES*

2.1 Introduction

Ternary lanthanide (Ln) transition-metal (M) aluminide compounds adopting the $ThMn_{12}$ structure type have been the subject of intense research efforts for decades as part of a search for materials exhibiting interesting magnetic ground states or transport properties.[1-6] These compounds crystallize in the space group *I*4/*mmm* with the general formula $Ln(M,X)_{12}$ (M = V-Fe, Ni, Zn; X = main group element). A related structure type, $CaCr_2Al_{10}$, can also be adopted for $LnMn_2Al_{10}$ compounds with Ln = Y, La-Nd, Sm, and Gd-Dy,[7-8] as well as for $LnRe_2Al_{10}$ compounds for Ln = Ce-Nd and Sm.[7]

The physical properties of Ln-M-Al compounds of the $ThMn_{12}$ structure type are strongly dependent on the transition metal. For example, $GdFe_4Al_8$ orders antiferromagnetically around 26 K due to Gd^{3+} while the iron sublattice orders in an antiferromagnetic fashion independently around 170 K. Meanwhile, $GdMn_4Al_8$, $GdCr_4Al_8$, and $GdCu_4Al_8$ order ferromagnetically at < 2 K, 7 K, and 35 K, respectively,[9] which is attributed to ordering of the lanthanide sublattice. The magnetic properties of $ThMn_{12}$-type Ln-M-Al compounds also show strong dependence on the relative concentration of the transition metal. Polycrystalline $GdMn_4Al_8$ does not order down to 2 K, but $GdMn_6Al_6$ orders antiferromagnetically below 36 K, due seemingly to the increased amount of Mn.[9] Similarly $GdCr_4Al_8$ orders antiferromagnetically below 7 K, whereas $GdCr_6Al_6$ orders ferromagnetically at much higher temperature (~175 K) and exhibits a saturation magnetization value of 8.2 μ_B/f.u. (Gd^{3+} = 7.0 μ_B), indicating the presence of magnetically ordered Cr.[9]

---

* Reprinted with permission from Fulfer, B. W.; Haldolaarachchige, N.; Young, D. P.; Chan, J. Y., Crystal growth and magnetic properties of Ln-Mn-Al (Ln = Gd, Yb) compounds of the $CaCr_2Al_{10}$ and $ThMn_{12}$ structure types. *J. Solid State Chem.* **2012,** *194*, 143-150.

The magnetic behavior of a transition metal in any given intermetallic compound is very much dependent on the structure type of that compound. An example is the magnetic behavior of Mn in $LnMn_4Al_8$ (ordered $ThMn_{12}$-type) and $LnMn_{2+x}Al_{10-x}$ (disordered $CaCr_2Al_{10}$-type) compounds. Susceptibility measurements of $LaMn_{2+x}Al_{10-x}$ compounds show that Mn carries a magnetic moment,[8] whereas $LaMn_4Al_8$ displays temperature independent Pauli paramagnetism down to 4.1 K.[10] $GdMn_{2+x}Al_{10-x}$, another $CaCr_2Al_{10}$-type compound, orders ferromagnetically with ordering temperatures increasing as the Mn concentration increases (T_C = 16 K, μ_{eff} = 8.0(2) μ_B/f.u. for x = 0.21, T_C = 25 K, μ_{eff} = 7.7(2) μ_B/f.u. for x = 0.39).[8] However, $GdMn_4Al_8$, adopting the $ThMn_{12}$-type, exhibits antiferromagnetic correlations (θ = -8.5 K).[9] While these compounds have very similar structures, they exhibit differing magnetic properties within a range of Mn concentration. Therefore these systems present an opportunity to investigate atomic site preferences with the goal of understanding the effect of chemistry on the properties of these compounds. Herein, the synthesis and structural characterization of $Ln(Mn,Al)_{12}$ (Ln = Gd, Yb) adopting the $ThMn_{12}$ structure type and $LnMn_{2+x}Al_{10-x}$ (Ln = Gd, Yb) of the $CaCr_2Al_{10}$ structure type are presented. The magnetic and transport properties of $YbMn_{2+x}Al_{10-x}$ single crystals are also discussed.

2.2 Experimental

2.2.1 Synthesis

Ln (Gd and Yb), Mn, and Al (> 99.9%) were combined in reaction ratios from 1:9:20 to 1:9:45 Ln:Mn:Al for $ThMn_{12}$-type analogues, and from 1:5:20 to 1:2:30 for $CaCr_2Al_{10}$-type analogues, and were placed into alumina crucibles. The crucibles were placed in fused silica tubes, which were subsequently evacuated, backfilled with ~1/4 atm of Ar, and sealed. Mn and

Al ratios (9:20 to 2:30 Mn:Al) were varied to study the impact of concentration on structure stabilization and on crystal growth.

2.2.1.1 $ThMn_{12}$-type $Ln(Mn,Al)_{12}$ (Ln = Gd, Yb)

The reaction vessel containing the Gd analogue was heated to 1200 °C at a rate of 100 °C/h and held at 1200 °C for 12 h. The sample was subsequently cooled to 1060 °C at a rate of 1 °C/h, then removed from the furnace and centrifuged to separate the crystals from excess Al flux. The reaction containing the Yb analogue was placed in a furnace, heated to 950 °C at a rate of 30 °C/h, and held at 950 °C for 72 h. The sample was then cooled to 750 °C at a rate of 30 °C/h, after which the sample was removed from the furnace and centrifuged. The rod-like single crystals appeared to be air-stable over a period of several weeks and were etched in weak solutions of NaOH and HCl (~ 0.1-0.2 M).

2.2.1.2 $CaCr_2Al_{10}$-type $LnMn_2Al_{10}$ (Ln = Gd, Yb)

The reactions that formed the $CaCr_2Al_{10}$ structure type were heated to 950 °C at a rate of 50 °C/h and held for 24 h. The sample was cooled to 850 °C at a rate of 5 °C/h, removed from the furnace, and centrifuged. Silver-colored rod-like crystals up to 5 mm long were recovered from the bottom of the crucible. Variations on growth stoichiometries, discussed later, were attempted to observe any relationship between initial reaction ratios and reaction product stoichiometries. These crystals also appeared to be air-stable, and were etched in weak solutions of NaOH and HCl (~ 0.1-0.2 M).

2.2.2 Structure Determination

Crystals of $Ln(Mn,Al)_{12}$ ($ThMn_{12}$-type) or $LnMn_{2+x}Al_{10-x}$ ($CaCr_2Al_{10}$-type) were cut to sizes appropriate for data collection (referenced in Tables 2.1a and 2.2a) and mounted to glass

Table 2.1a. Crystallographic parameters for $ThMn_{12}$-type $Ln(Mn,Al)_{12}$ (Ln = Gd, Yb)

Crystal data			
Formula	**$GdMn_{3.76(4)}Al_{8.24(4)}$**	**$YbMn_{2.55(4)}Al_{9.45(4)}$**	**$YbMn_{2.92(4)}Al_{9.08(4)}$**
Nominal ratio (Ln:Mn:Al)	1:1:3	1:9:45	1:9:20
Space group	*I4/mmm*	*I4/mmm*	*I4/mmm*
a (Å)	8.8780(5)	8.9760(3)	8.9400(9)
c (Å)	5.1190(3)	5.1110(3)	5.1020(9)
V (Å^3)	403.47(4)	411.79(3)	407.77(9)
Z	2	2	2
Crystal size (mm)	0.04 x 0.04 x 0.04	0.05 x 0.05 x 0.05	0.02 x 0.04 x 0.04
Temperature (K)	294	294	294
Density (g cm^{-3})	4.719	4.581	4.729
θ Range (°)	3.25-30.02	3.21-30.98	3.22-32.23
μ (mm^{-1})	14.007	16.004	16.784
Data Collection and Refinement			
Collected reflections	507	656	382
Unique reflections	193	216	229
R_{int}	0.0244	0.0194	0.0487
h	$-12 \le h \le 12$	$-12 \le h \le 12$	$0 \le h \le 13$
k	$-8 \le k \le 8$	$-8 \le k \le 9$	$-8 \le k \le 8$
l	$-7 \le l \le 6$	$-7 \le l \le 7$	$0 \le l \le 7$
$\Delta\rho_{max}$ (e Å^{-3})	1.301	1.582	2.310
$\Delta\rho_{min}$ (e Å^{-3})	-0.859	-1.526	-2.211
GoF	1.195	1.133	1.065
Extinction coefficient	0.0211(10)	0.0035(7)	0.0016(4)
[a] $R_1(F)$ for $F_o^2 > 2\sigma(F_o^2)$	0.016	0.017	0.031
[b] $R_w(F_o^2)$	0.035	0.041	0.034

[a] $R_1 = \Sigma||F_o| - |F_c||/\Sigma|F_o|$
[b] $wR_2 = [\Sigma w(F_o^2 - F_c^2)^2/\Sigma w(F_o^2)^2]^{1/2}$; $w = 1/[\sigma^2(F_o^2) + 0.8378P]$, $w = 1/[\sigma^2(F_o^2) + 0.0257P^2 + 0.2980P]$, and $w = 1/[\sigma^2(F_o^2) + 0.0109P^2 + 0.0494P]$ at 294 K for $GdMn_{3.76(4)}Al_{8.34(4)}$, $YbMn_{2.55(4)}Al_{9.45(4)}$, and $YbMn_{2.92(4)}Al_{9.08(4)}$, respectively.

Table 2.1b. Atomic positions and thermal parameters for $ThMn_{12}$-type $Ln(Mn,Al)_{12}$ (Ln = Gd, Yb)

Atom	Wyckoff position	x	y	z	[a] U_{eq} (Å^2)
$GdMn_{3.76(4)}Al_{8.24(4)}$					
Gd	2*a*	0	0	0	0.00506(19)
M1	8*f* (94(1)%Mn+6(1)%Al)	1/4	1/4	1/4	0.0039(3)
Al1	8*i*	0.34193(15)	0	0	0.0069(3)
Al2	8*j*	0.27738(15)	1/2	0	0.0043(3)
$YbMn_{2.55(4)}Al_{9.45(4)}$					
Yb1	2*a*	0	0	0	0.01113(17)
M1	8*f* (64(1)%Mn+36(1)%Al)	1/4	1/4	1/4	0.0106(3)
Al1	8*i*	0.34584(17)	0	0	0.0129(3)
Al2	8*j*	0.28089(18)	1/2	0	0.0135(3)
$YbMn_{2.92(4)}Al_{9.08(4)}$					
Yb1	2*a*	0	0	0	0.0057(2)
M1	8*f* (73(1)%Mn+27(1)%Al)	1/4	1/4	1/4	0.0056(4)
Al1	8*i*	0.3436(2)	0	0	0.0091(5)
Al2	8*j*	0.2814(2)	1/2	0	0.0075(5)

[a] U_{eq} is defined as one-third of the trace of the orthagonalized U_{ij} tensor.

Table 2.1c. Selected interatomic distances (Å) for $Ln(Mn,Al)_{12}$ compounds ($ThMn_{12}$-type)

	$GdMn_{3.76(4)}Al_{8.24(4)}$	$YbMn_{2.55(4)}Al_{9.45(4)}$	$YbMn_{2.92(4)}Al_{9.08(4)}$
Ln environment			
Ln-Al1 (x4)	3.036(2)	3.1043(15)	3.072(2)
Ln-Al2 (x8)	3.234(2)	3.2247(10)	3.214(2)
Ln-*M* (x8)	3.390(2)	3.4211(10)	3.408(2)
M environment			
M-*M* (x2)	2.560(2)	2.5555(10)	2.551(2)
M-Al2 (x4)	2.574(2)	2.5971(14)	2.589(2)
M-Al2 (x4)	2.689(2)	2.7218(13)	2.706(3)

Table 2.2a. Crystallographic parameters for $CaCr_2Al_{10}$-type $LnMn_{2+x}Al_{10-x}$ (Ln = Gd, Yb)

Crystal data					
Formula	$GdMn_{2.21(4)}Al_{9.79(4)}$	$YbMn_{2.06(4)}Al_{9.94(4)}$	$YbMn_{2.10(4)}Al_{9.90(4)}$	$YbMn_{2.17(4)}Al_{9.83(4)}$	$YbMn_{2.27(4)}Al_{9.73(4)}$
Nominal ratio (Ln:Mn:Al)	1:2:30	1:2:30	1:5:20	1:5:40	1:3:20
Space group	*P4/nmm*	*P4/nmm*	*P4/nmm*	*P4/nmm*	*P4/nmm*
a (Å)	12.7730(10)	12.776(4)	12.7738(15)	12.761(2)	12.7483(14)
c (Å)	5.1280(10)	5.1168(10)	5.1172(10)	5.1170(10)	5.1164(12)
V (Å^3)	836.63(19)	835.2(4)	835.0(2)	833.3(2)	831.5(2)
Z	4	4	4	4	4
Crystal size (mm)	0.02 x 0.04 x 0.04	0.04 x 0.10 x 0.10	0.05 x 0.05 x 0.08	0.04 x 0.04 x 0.06	0.10 x 0.16 x 0.20
Temperature (K)	294	294	294	294	294
Density (g cm^{-3})	4.309	4.396	4.418	4.442	4.476
θ Range (°)	2.25-30.96	3.19-30.02	3.19-30.57	3.19-32.53	2.26-29.96
μ (mm^{-1})	12.053	15.052	15.184	15.302	15.485
Data Collection and Refinement					
Collected reflections	2027	2168	2417	1400	2102
Unique reflections	751	691	727	828	697
R_{int}	0.0326	0.0451	0.0247	0.0279	0.0478
h	$-18 \le h \le 18$	$-17 \le h \le 17$	$-18 \le h \le 18$	$0 \le h \le 18$	$-17 \le h \le 17$
k	$-12 \le k \le 12$	$-12 \le k \le 12$	$-12 \le k \le 12$	$-12 \le k \le 13$	$-12 \le k \le 12$
l	$-4 \le l \le 7$	$-7 \le l \le 6$	$-7 \le l \le 7$	$0 \le l \le 7$	$-7 \le l \le 5$
$\Delta\rho_{max}$ (e Å^{-3})	1.656	2.194	1.161	1.517	1.714
$\Delta\rho_{min}$ (e Å^{-3})	-1.097	-2.212	-2.071	-2.300	-1.944
GoF	1.070	1.049	1.097	1.082	1.062
Extinction coefficient	0.0156(8)	0.0034(4)	0.0030(3)	0.00194(16)	0.00085(15)
[a] $R_1(F)$ for $F_o^2 > 2\sigma(F_o^2)$	0.0267	0.0298	0.0245	0.0285	0.0262
[b] $R_w(F_o^2)$	0.0683	0.0758	0.0629	0.0510	0.0481

[a] $R_1 = \Sigma||F_o| - |F_c||/\Sigma|F_o|$

[b] $wR_2 = [\Sigma w(F_o^2 - F_c^2)^2/\Sigma w(F_o^2)^2]^{1/2}$; $w = 1/[\sigma^2(F_o^2) + 0.0379P^2 + 0.0598P]$, $w = 1/[\sigma^2(F_o^2) + 0.0406P^2 + 2.3925P]$, $w = 1/[\sigma^2(F_o^2) + 0.0361P^2 + 0.6001P]$, $w = 1/[\sigma^2(F_o^2) + 0.0196P^2]$, and $w = 1/[\sigma^2(F_o^2) + 0.0115P^2 + 0.2061P]$ at 294 K for $GdMn_{2.21(4)}Al_{9.79(4)}$, $YbMn_{2.09(4)}Al_{9.94(4)}$, $YbMn_{2.10(4)}Al_{9.90(4)}$, $YbMn_{2.16(4)}Al_{9.84(4)}$,and $YbMn_{2.27(4)}Al_{9.73(4)}$, respectively.

Table 2.2b. Atomic positions and thermal parameters for $CaCr_2Al_{10}$-type $LnMn_{2+x}Al_{10-x}$ (Ln = Gd, Yb)

Atom	Wyckoff position	x	y	z	$^{a}U_{eq}$ (Å^2)
$GdMn_{2.21(4)}Al_{9.79(4)}$					
Gd1	2*c*	1/4	1/4	0.51984(8)	0.00762 (17)
Gd2	2*a*	3/4	1/4	0	0.00905 (17)
Mn1	8*i*	1/4	0.50730(4)	0.24956(10)	0.00713(19)
Al1	8*j*	0.07537(8)	*x*	0.4818(2)	0.0102(3)
Al2	8*j*	0.14216(8)	*x*	0.0291(2)	0.0095(3)
M1	8*i* (10(2)%Mn+90(2)%Al)	1/4	0.00833(8)	0.74861(19)	0.0083(3)
Al4	8*h*	0.36149(8)	-*x*	1/2	0.0090(3)
Al5	8*g*	0.42487(8)	-*x*	0	0.0102(3)
$YbMn_{2.06(4)}Al_{9.94(4)}$					
Yb1	2*c*	1/4	1/4	0.52604(9)	0.00360(19)
Yb2	2*a*	3/4	1/4	0	0.00483(19)
Mn1	8*i*	1/4	0.508016(6)	0.25335(12)	0.0017(2)
Al1	8*j*	0.07552(13)	*x*	0.4835(3)	0.0056(4)
Al2	8*j*	0.14321(12)	*x*	0.0353(3)	0.0050(4)
Al3	8*i*(3(3)%Mn+97(3)%Al)	1/4	0.01048(13)	0.7498(2)	0.0016(3)[b]
Al4	8*h*	0. 36233(12)	-*x*	1/2	0.0038(4)
Al5	8*g*	0. 42478(13)	-*x*	0	0.0053(4)
$YbMn_{2.10(4)}Al_{9.90(4)}$					
Yb1	2*c*	1/4	1/4	0.52504(8)	0.00920(16)
Yb2	2*a*	3/4	1/4	0	0.01034(16)
Mn1	8*i*	1/4	0.50789(5)	0.25308(11)	0.00750(18)
Al1	8*j*	0.07571(10)	*x*	0.4838(2)	0.0108(3)
Al2	8*j*	0.14293(9)	*x*	0.0343(3)	0.0100(3)
M1	8*i* (5(1)%Mn+95(1)%Al)	1/4	0.00998(10)	0.7500(2)	0.0082(4)
Al4	8*h*	0.36200(9)	-*x*	1/2	0.0099(3)
Al5	8*g*	0.42480(10)	-*x*	0	0.0099(3)
$YbMn_{2.17(4)}Al_{9.83(4)}$					
Yb1	2*c*	1/4	1/4	0.52390(7)	0.00525(14)
Yb2	2*a*	3/4	1/4	0	0.00659(15)
Mn1	8*i*	1/4	0.50780(6)	0.25266(11)	0.00396(16)
Al1	8*j*	0.07575(10)	*x*	0.4842(2)	0.0068(4)
Al2	8*j*	0.14301(10)	*x*	0.0327(2)	0.0065(3)
M1	8*i* (9(1)%Mn+91(1)%Al)	1/4	0.00956(11)	0.7493(2)	0.0049(4)
Al4	8*h*	0.36203(10)	-*x*	1/2	0.0062(4)
Al5	8*g*	0.42448(10)	-*x*	0	0.0067(4)
$YbMn_{2.27(4)}Al_{9.73(4)}$					
Yb1	2*c*	1/4	1/4	0.52133(8)	0.00949(17)
Yb2	2*a*	3/4	1/4	0	0.01022(18)
Mn1	8*i*	1/4	0.50724(6)	0.25203(19)	0.00783(19)
Al1	8*j*	0.07621(12)	*x*	0.4844(2)	0.0107(4)
Al2	8*j*	0.14255(11)	*x*	0.0297(3)	0.0098(4)
M1	8*i* (14(1)%Mn+86(1)%Al)	1/4	0.00853(11)	0.7487(3)	0.0080(4)
Al4	8*h*	0.36151(11)	-*x*	1/2	0.0106(5)
Al5	8*g*	0.42398(12)	-*x*	0	0.0111(4)

[a]U_{eq} is defined as one-third of the trace of the orthagonalized U_{ij} tensor.
[b]Atomic displacement parameter refined isotropically.

Table 2.2c. Selected interatomic distances (Å) for $LnMn_{2+x}Al_{10-x}$ compounds ($CaCr_2Al_{10}$-type)

	$GdMn_{2.21(4)}Al_{9.79(4)}$	$YbMn_{2.06(4)}Al_{9.94(4)}$	$YbMn_{2.10(4)}Al_{9.90(4)}$	$YbMn_{2.17(4)}Al_{9.83(4)}$	$YbMn_{2.27(4)}Al_{9.73(4)}$
Ln1 environment					
Ln1-Al1 (x4)	3.161(16)	3.160(4)	3.1556(13)	3.1513(14)	3.1389(15)
Ln1-Al2 (x4)	3.182(17)	3.167(4)	3.1698(15)	3.1696(12)	3.1749(16)
Ln1-Al2 (x4)	3.258(17)	3.242(4)	3.2454(15)	3.2417(12)	3.2432(16)
Ln1-Al3/Mn3(x4)	3.302(11)	3.267(4)	3.2750(13)	3.2778(16)	3.2908(15)
Ln1-Mn (x4)	3.567(13)	3.581(3)	3.5761(10)	3.5707(10)	3.5571(10)
Ln2 environment					
Ln2-Al5 (x4)	3.159(16)	3.158(4)	3.1577(13)	3.1484(14)	3.1367(15)
Ln2-Al4 (x8)	3.260(17)	3.266(3)	3.2619(10)	3.2610(10)	3.2536(10)
Ln2-Mn (x4)	3.354(12)	3.351(3)	3.3529(10)	3.3500(10)	3.3527(10)
Ln2-Al3/Mn3(x4)	3.543(12)	3.566(2)	3.5588(10)	3.5521(16)	3.5377(15)
Mn environment					
Mn-Al4 (x2)	2.547(15)	2.528(3)	2.5309(11)	2.5308(14)	2.5358(14)
Mn-Al3/Mn3	2.567(2)	2.551(3)	2.5531(13)	2.5512(13)	2.5491(19)
Mn-Al3/Mn3	2.577(2)	2.588(3)	2.5845(13)	2.5850(13)	2.5831(19)
Mn-Al2 (x2)	2.612(14)	2.617(3)	2.6145(14)	2.6142(14)	2.6109(16)
Mn-Al5 (x2)	2.716(13)	2.720(3)	2.7207(12)	2.7156(13)	2.7113(15)
Mn-Al1 (x2)	2.740(13)	2.738(4)	2.7370(13)	2.7363(14)	2.7302(16)

fibers using epoxy. X-ray diffraction data were collected using a Nonius Kappa CCD diffractometer outfitted with Mo Kα radiation (λ = 0.71073 Å). Crystallographic parameters for $Ln(Mn,Al)_{12}$ (Ln = Gd, Yb) and $LnMn_{2+x}Al_{10-x}$ (Ln = Gd, Yb) are included in Table 2.1a and Table 2.2a, respectively. Structural solutions were obtained using direct methods with SIR97[11] and the resulting model was refined using SHELXL97.[12] All refinements were performed under the assumption of full crystallographic occupancy and subsequently converged with small residual unassigned electron density peaks. Structural models were corrected for extinction and refined with anisotropic atomic displacement parameters. Mn/Al mixing was modeled for specific sites (denoted M1, 8*i* position for $CaCr_2Al_{10}$-type and 8*f* position for $ThMn_{12}$-type). Sample compositions were in good agreement with ICP-OES. Atomic positions and displacement parameters are provided in Tables 2.1b and 2.2b, along with selected interatomic distances in Tables 2.1c and 2.2c. In addition to single crystal X-ray diffraction, powder X-ray diffraction was also used to confirm phase-purity on ground single-crystals using a Bruker AXS D8 Advance diffractometer.

2.2.3 Magnetization and Electrical Transport

Magnetic data were obtained using a Quantum Design Physical Property Measurement System (PPMS). Temperature-dependent magnetic susceptibility was measured under zero-field-cooled (ZFC) conditions from 3 to 300 K under an applied field of 5 T. Field-dependent magnetization measurements were performed at 3 K with field strength up to 9 T. Electrical resistivity data from 3 K to 290 K were obtained via a standard four-probe AC technique using the PPMS.

2.3. Results and Discussion

2.3.1 Synthesis and Structure

Previously reported syntheses of Mn-containing compounds that crystallize in the $ThMn_{12}$ structure type are generally accomplished via arc-melting of all reactants.[1] To the best of our knowledge there are no reports of $ThMn_{12}$-type aluminide single crystals containing Mn that have been grown via self-flux method. We have grown single crystals (~ 4 mm long in some cases) of $GdMn_{3.76(4)}Al_{8.24(4)}$, and $YbMn_{2.55(4)}Al_{9.45(4)}$ and $YbMn_{2.94(4)}Al_{9.06(4)}$ with reaction ratios of 1:1:3 (Gd:Mn:Al), and 1:9:45 and 1:9:20 (Yb:Mn:Al), respectively. Nominal reaction ratios are reiterated in Table 2.1. Additional growths of these compounds were attempted with modified procedures (increase of dwell time, decrease in heating rate, decrease in cooling rate) in order to increase crystal size. The most effective method found to grow large $ThMn_{12}$-type single crystals was utilizing a Ln:Mn molar reaction ratio of approximately 1:10. Decreasing the moles of Mn compared to the moles of Ln (from 1:9 to 1:5 for Yb:Mn) generally resulted in the formation of $CaCr_2Al_{10}$-type crystals instead of $ThMn_{12}$-type crystals. Overall, the presence of excess Al flux ensures high quality single crystals by reducing the amount of Mn-Al binaries

formed. Avoiding Mn-Al binaries ensures more Mn remains in the melt, which can then go towards forming large ternary single crystals.

As a reference for the $ThMn_{12}$ structure type, the compound $Gd(Mn,Al)_{12}$ will be discussed. For the structurally ordered $GdMn_4Al_8$ (Figure 2.1) variant, Gd and Mn occupy the 2*a* and 8*f* sites, respectively, while Al occupies the 8*i* and 8*j* sites. Examples from the literature indicate that it is possible to introduce disorder by altering the amount of Mn present during the formation of these compounds. At low Mn concentrations mixing occurs at the 8*f* site between Mn and Al, whereas at higher Mn concentrations Mn/Al mixing occurs preferentially at the 8*j* site.[9,13]

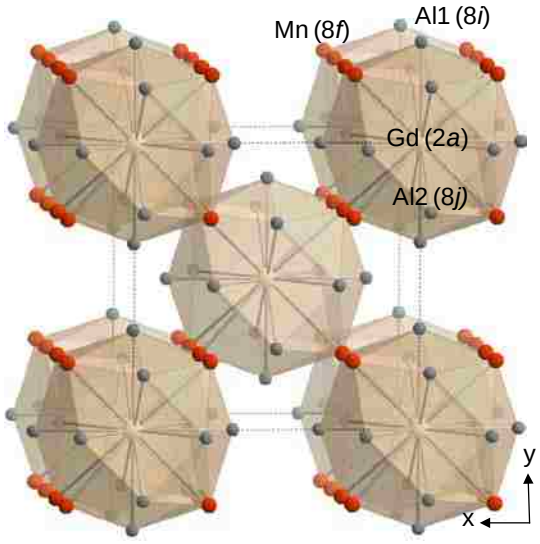

Figure 2.1. Crystal structure of $GdMn_4Al_8$, where Gd atoms are represented by tan spheres, Mn atoms by red, and Al by dark grey.

$LnMn_{2+x}Al_{10-x}$ compounds have been reported as grown via self-flux method for Ln = La and Gd. Varying the concentration of Mn (x) is achieved by altering the amount of Mn in the initial melt (1:2:22 yields x = 0.21(1) and 1:3:22 yields x = 0.39(1) for Gd analogues).[8] Using similar Al-rich melts, we have reproduced good quality single crystals of $GdMn_{2+x}Al_{10-x}$ (x = 0.21(4) for reaction ratio 1:2:30 Gd:Mn:Al) and successfully synthesized $YbMn_{2+x}Al_{10-x}$ (x =

0.06(4), 0.10(4), 0.17(4), and 0.27(4) for reaction ratios of 1:2:30, 1:5:20, 1:5:40, and 1:3:20 Yb:Mn:Al, respectively) analogues adopting the $CaCr_2Al_{10}$ structure type. Nominal reaction ratios are provided in Table 2.2. As stated previously, decreasing the amount of Mn relative to Yb from 1:9 to 1:5 resulted in the formation of crystals adopting the $CaCr_2Al_{10}$ structure type rather than the $ThMn_{12}$ structure type. All other variations in the Yb:Mn reaction ratio (less Mn than 1:5) yielded $YbMn_{2+x}Al_{10-x}$ crystals with refined compositions of x = 0.06 to 0.27. As a general trend, additional Mn content in resultant compounds did follow an increase of the Mn:Al reaction ratio, and it is worth noting that increasing the Mn:Al reaction ratio in some cases led to the formation of $ThMn_{12}$-type compounds rather than $CaCr_2Al_{10}$-type compounds. Improved crystal quality was observed with a decrease of the Mn:Al reaction ratio, as was the case for $ThMn_{12}$-type crystals.

Ternary aluminides forming in the $CaCr_2Al_{10}$ structure type are less well studied than those that adopt the $ThMn_{12}$-type. The $LnMn_{2+x}Al_{10-x}$ (Ln = lanthanide) compounds of the $CaCr_2Al_{10}$ structure type crystallizes in the tetragonal *P*4/*nmm* space group (No. 129). It is important to note that both structurally ordered (x = 0) and disordered variants have been reported in the literature for $LnM_{2+x}Al_{10-x}$ systems (M = transition metal). When comparing $GdMn_2Al_{10}$ (ordered $CaCr_2Al_{10}$-type,[7] Figure 2.2) to $GdMn_4Al_{10}$ (ordered $ThMn_{12}$-type), similarities are immediately recognizable. The local environments for Gd in both structure types appear to be similar; both are 20-coordinate polyhedra with comparable geometrical arrangements of Mn and Al atoms. The difference between the Gd environments for the two structure types is substitutional. Half of the Mn (8*f*) sites in $GdMn_4Al_8$ are substituted by Al atoms for $GdMn_2Al_{10}$. The two separate Gd environments in $GdMn_2Al_{10}$ arise from two

different resulting arrangements of Mn around Gd. This substitution results in doubling the unit cell volume from ~ 400 Å^3 in $GdMn_4Al_8$ to ~ 800 Å^3 in $GdMn_2Al_{10}$.

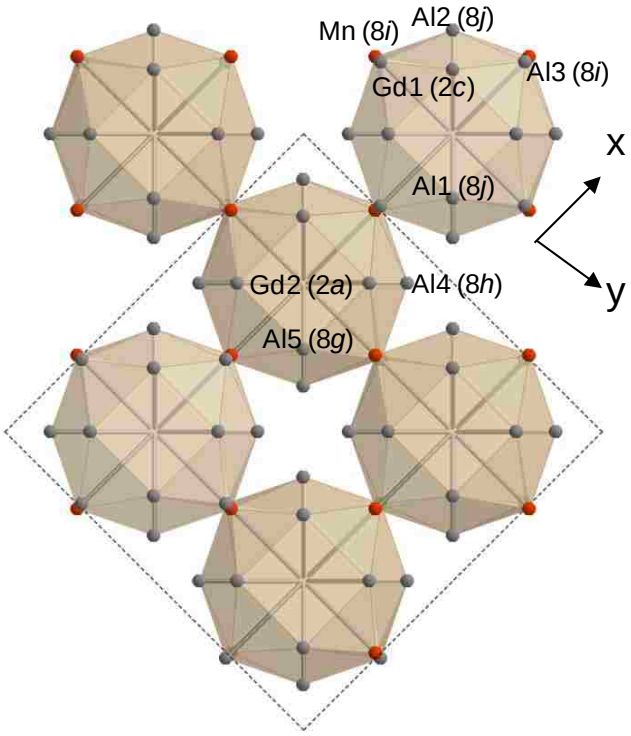

Figure 2.2. Crystal structure of $GdMn_2Al_{10}$ where Gd (2a, 2c) atoms are represented by tan spheres, Mn atoms (8i) by red, and Al (8g, 8h, 8i, and 2x 8j) by dark grey.

2.3.2 Physical Properties

2.3.2.1 $ThMn_{12}$-type

Temperature dependent magnetic susceptibility for single crystalline $YbMn_{2.55}Al_{9.45}$ ($ThMn_{12}$-type) is shown in Figure 2.3. Susceptibility shows paramagnetic behavior down to 3 K. The calculated effective moment is 4.2(4) μ_B/Yb which is close to the moment expected for Yb^{3+} (4.54 μ_B). However, unit cell parameters for $YbMn_{2.55(4)}Al_{9.45(4)}$ are close to those of $GdMn_{3.76(4)}Al_{8.24(4)}$.

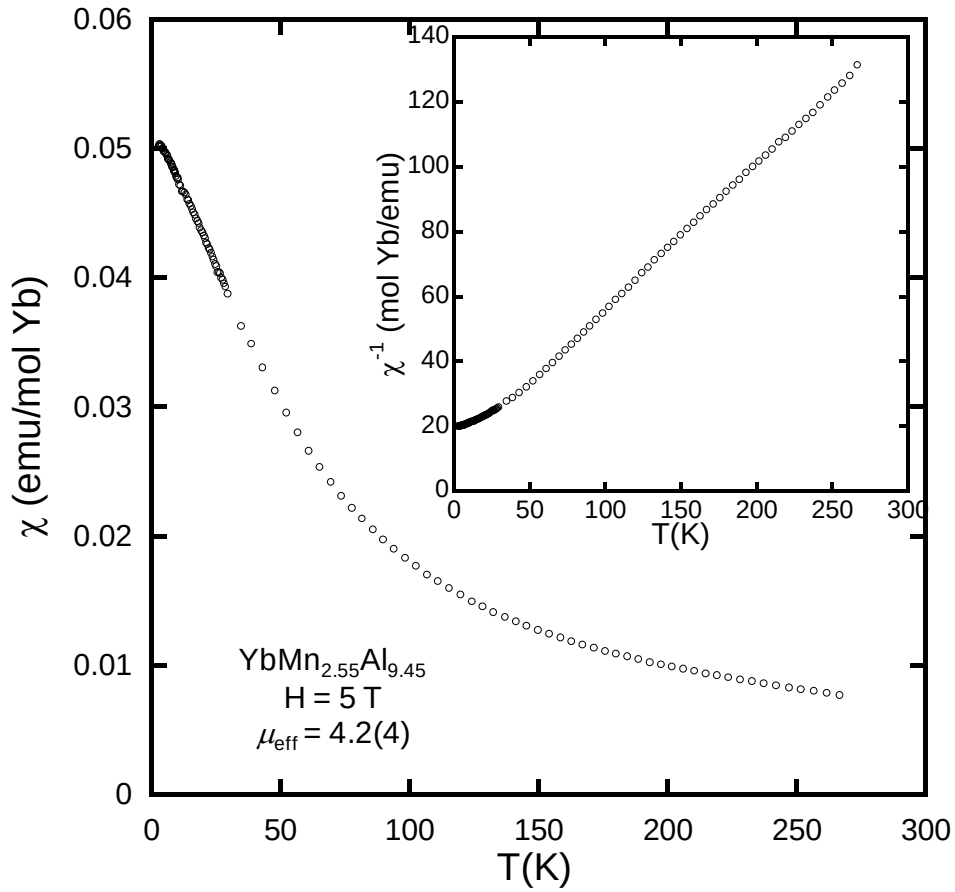

Figure 2.3. Magnetic susceptibility (emu/mol Yb) of $YbMn_{2.55}Al_{9.45}$as a function of temperature.

The electrical resistivity as a function of temperature is shown for single crystalline $YbMn_{2.55(4)}Al_{9.45(4)}$ in Figure 2.4. Electrical resistivity decreases with decreasing temperature at high temperature. At approximately 100 K the resistivity reaches a minimum value, and then increases with decreasing temperature. This feature in the resistivity could be indicative of conduction electrons scattering off localized magnetic moments beginning around 100 K (Kondo effect).

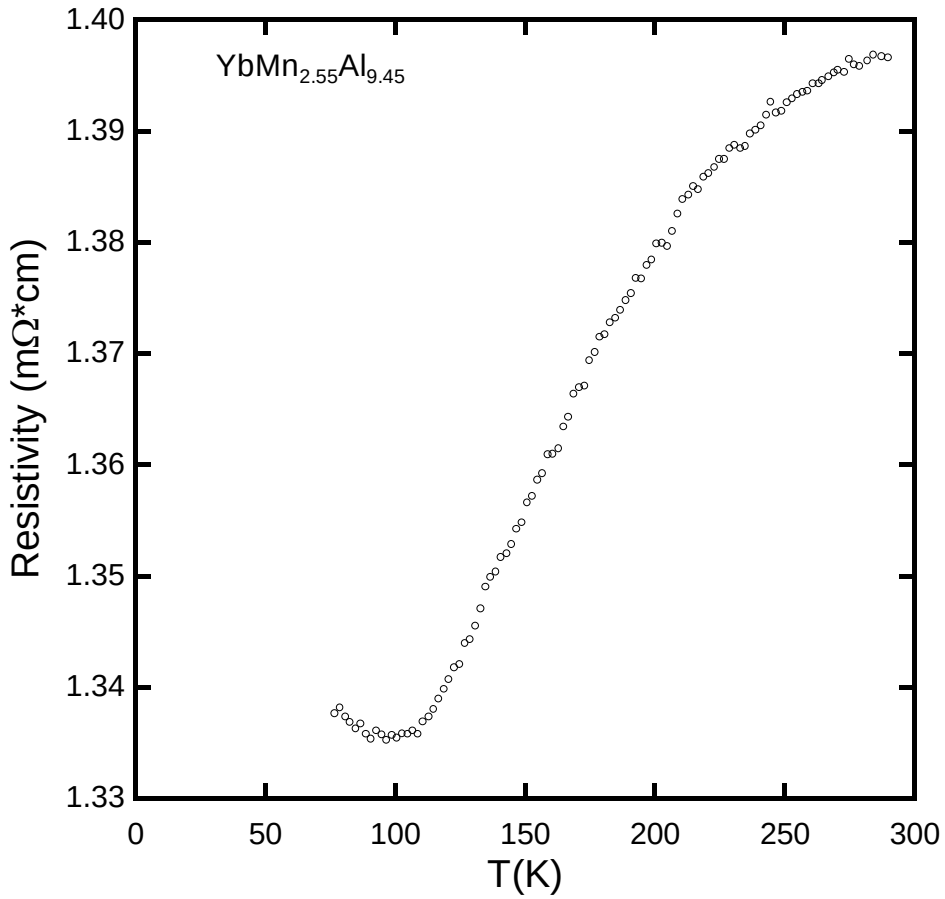

Figure 2.4. Electrical resistivity for $YbMn_{2.55}Al_{9.45}$ as a function of temperature.

2.3.2.2 $CaCr_2Al_{10}$-type

The temperature dependence of the magnetic susceptibility at 5 T for single crystals of $YbMn_{2.06}Al_{9.94}$ and $YbMn_{2.21}Al_{9.91}$ are shown in Figures 2.5 and 2.6, respectively. The magnetic susceptibility was fit to a modified Curie-Weiss equation $\chi(T) = \chi_0 + C/(T-\theta)$, where C represents the Curie constant, θ is the Weiss temperature, and χ_0 is the temperature-independent term. χ_0 was subtracted from the susceptibility, and the values were re-plotted as a function of temperature as shown in Figures 2.5 and 2.6. Similar measurements were also made at 0.1 T, unfortunately the magnetic signal from the samples was too weak to effectively fit to the modified Curie-Weiss law.

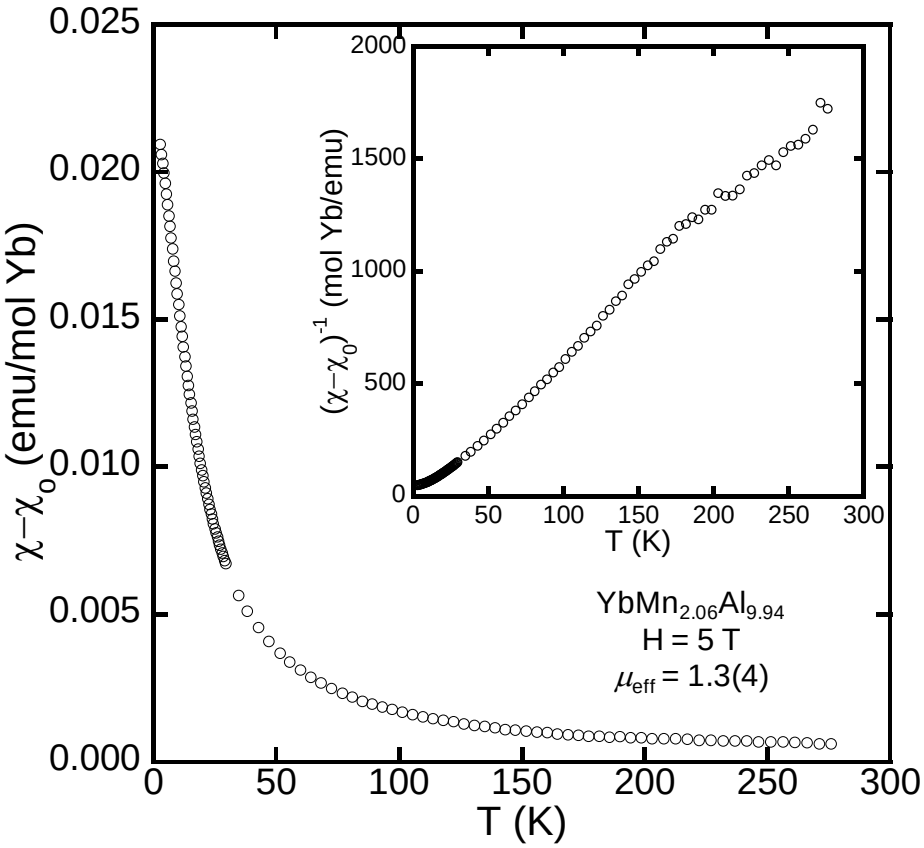

Figure 2.5. Magnetic susceptibility (emu/mol Yb) of $YbMn_{2.06}Al_{9.94}$ as a function of temperature; the inset shows inverse magnetic susceptibility as a function of temperature.

The temperature-dependent magnetic susceptibilities show paramagnetic behavior down to 3 K. The effective moments for the $YbMn_{2+x}Al_{10-x}$ compounds per formula unit were calculated to be 1.3 μ_B (x = 0.06) and 1.54 μ_B (x = 0.21). These moments are far from the calculated effective moment of Yb^{3+} of 4.54 μ_B. Magnetic parameters for the data are summarized in Table 2.4. The reduced magnitude of these calculated moments could be indicative of divalent (non-magnetic) or intermediate valent Yb, which has been documented in the literature.[14-19] One such system that displays a range of Yb valence states is the $YbMn_6Ge_{6-x}Sn_x$ system, which is a solid solution that shows a gradual change from Yb^{3+} for low x values to Yb^{2+} at higher x values. For this system, ytterbium ordering is thought to break down at a valence of ~2.5+.[14]

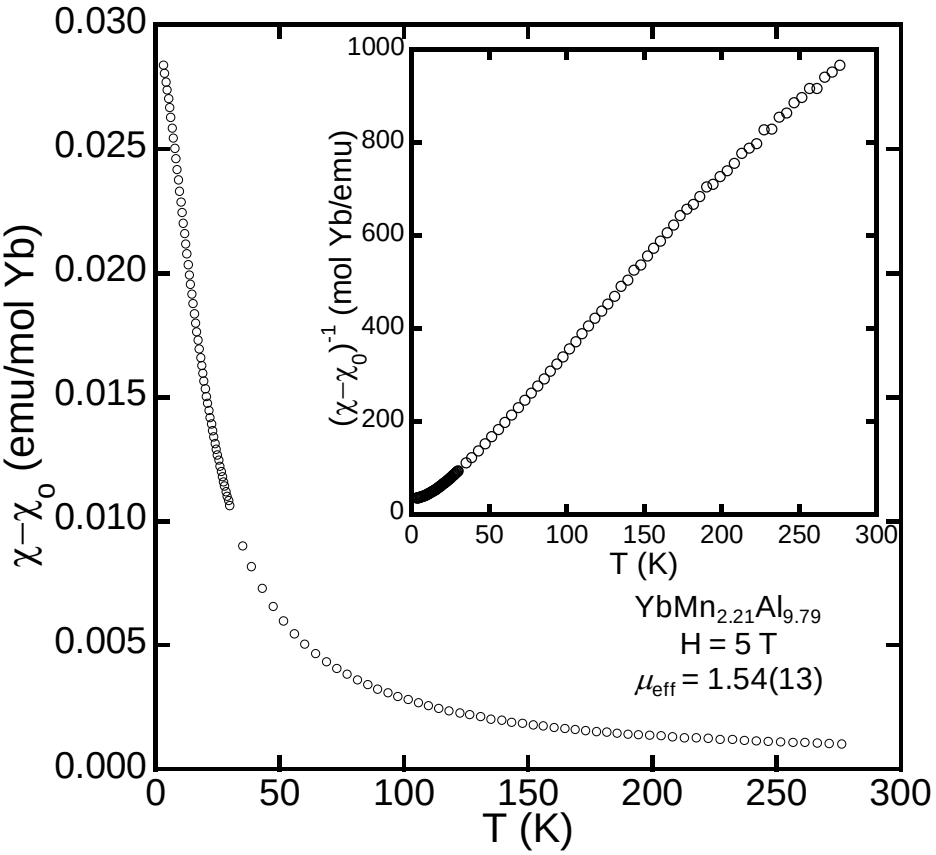

Figure 2.6. Magnetic susceptibility (emu/mol Yb) of $YbMn_{2.21}Al_{9.79}$ as a function of temperature; the inset shows inverse magnetic susceptibility as a function of temperature.

The data for $YbMn_{2+x}Al_{10-x}$ compounds compares well with data for other $LnMn_{2+x}Al_{10-x}$ compounds in literature. The similarities in physical properties between the Yb compounds examined here and the La analogues reported in literature[8] are particularly interesting. $LaMn_{2+x}Al_{10-x}$ compounds reported for x = 0.26(1) and 0.41(3) were fitted with the Curie-Weiss equation in the paramagnetic range (T < 50 K). Effective moments of 1.5(2) μ_B/f.u. (x = 0.26) and 1.9(2) μ_B/f.u. (x = 0.41) were obtained and attributed to the excess Mn carried on the Al 8*i* site. Taking into consideration the fact that the magnetic moment for the Yb analogue reported here is much lower than what is calculated for the Yb^{3+} ion and that the volume of the Yb analogue is close to that of the Gd analogue reported in literature,[8] it is not unreasonable to assert that Yb in this analogue is closer to a divalent state than a trivalent state. This assertion is

Table 2.4. Magnetic properties for $CaCr_2Al_{10}$-type and $ThMn_{12}$-type $YbMn_{2+x}Al_{10-x}$ compounds

Compound	C	χ_o (x 10^{-3})	θ	μ_{eff} (μ_B/f.u.)	Fit Range (K)	Ordering T_N (K)
$YbMn_{2.06}Al_{10.94}$	0.21(2)	1.802(17)	-5(6)	1.3(4)	70-203	PM
$YbMn_{2.21}Al_{10.79}$	0.296(2)	1.735(17)	3.6(3)	1.54(13)	47-165	PM
$YbMn_{2.55}Al_{10.45}$*	2.17(2)	-	-21.0(6)	4.2(4)	48-267	PM

*$ThMn_{12}$-type

supported by recent unpublished work performed on $Ln_6Cr_4Al_{43}$ (Ln = Gd, Yb). Magnetization data show that the Yb compound is diamagnetic, indicating Yb is divalent, while interatomic distances and unit cell volumes for $Gd_6Cr_4Al_{43}$ and $Yb_6Cr_4Al_{43}$ are very similar, as they are for $GdMn_{2+x}Al_{10-x}$ and $YbMn_{2+x}Al_{10-x}$ (Table 2.3). This would explain the magnetic similarities between the La analogues found in literature and the compound reported here with Yb^{2+}. Thus, the magnetic moment observed for the Yb analogue could be solely due to Mn. In fact, when effective moments are calculated per magnetic Mn for the two analogues reported here, the values are 5.2 μ_B/xMn (x = 0.06) and 3.4 μ_B/xMn (x = 0.21). These numbers are close to the calculated spin-only moments of Mn^{3+} (4.9 μ_B) and Mn^{4+} (3.9 μ_B), which lends credence to this argument, although we do not presume to be able to assign specific oxidation states to these Mn atoms.

The possible presence of magnetic Mn in $CaCr_2Al_{10}$-type Ln-Mn-Al compounds is curious, as it stands in contrast with what has been found for ordered $ThMn_{12}$-type Ln-Mn-Al compounds. $ThMn_{12}$-type $LnMn_4Al_8$ compounds tend to order antiferromagnetically as a result of Ln-Ln coupling only. However, as one increases the amount of Mn in $Ln(Mn,Al)_{12}$ compounds, the magnetic behavior of Mn changes.[9] Magnetic data for $GdMn_6Al_6$ show an increase in the magnetic ordering temperature for temperature dependent susceptibility to 36 K.[9] This is attributed to the magnetic moments found on the excess manganese that preferentially

occupies the 8*j* position in the $ThMn_{12}$ structure type.[20] As a result of investigations into the magnetic correlations of Mn atoms in $LnMn_2$ compounds, a critical Mn-Mn nearest neighbor distance of 2.66 Å was postulated, past which magnetic contributions due to Mn could be determined.[21] Though the findings presented here do not reinforce a critical Mn-Mn distance of 2.66 Å, it is thought that increasing the Mn atoms substituted on the 8*i* position corresponds to an increased probability that Mn-Mn distances will reach some critical value, allowing these Mn atoms to carry a moment.

The electrical resistivity as a function of temperature was measured for $YbMn_{2+x}Al_{10-x}$ (x = 0.06, 0.21) single crystals and is shown in Figure 2.7. At temperatures above 35 K the

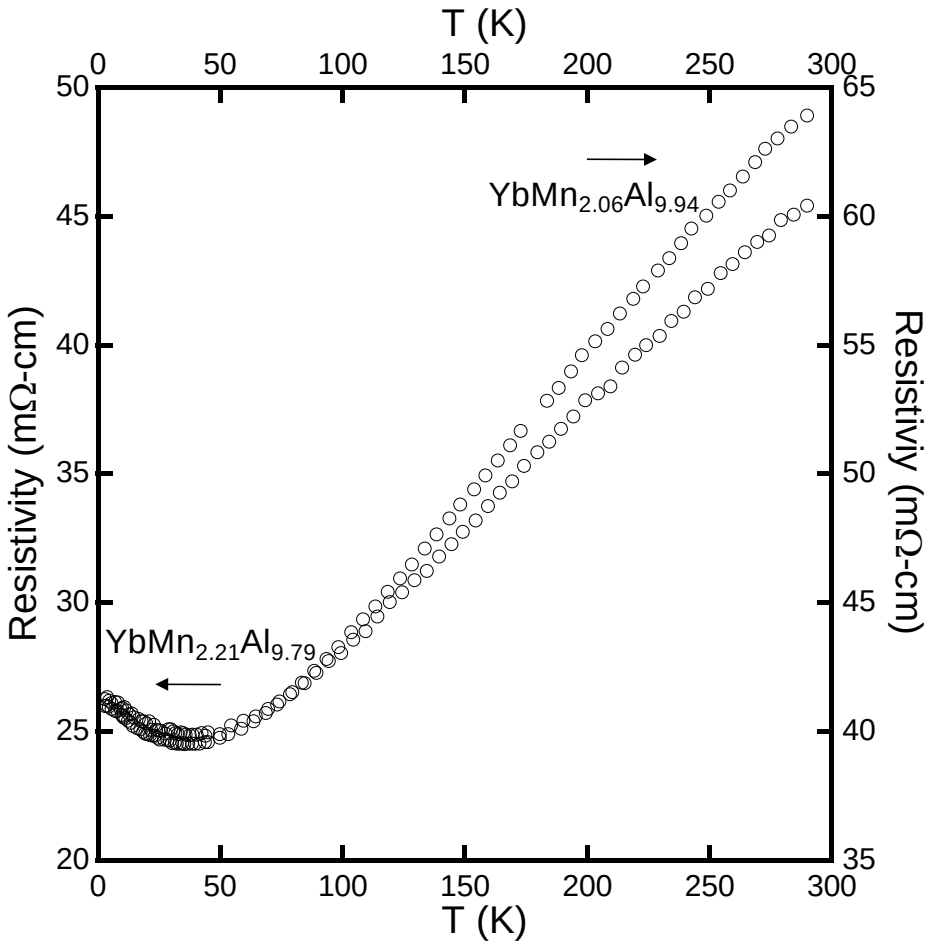

Figure 2.7. Electrical resistivity for $YbMn_{2+x}Al_{10-x}$ (x = 0.06, 0.21) as a function of temperature.

resistivity values shows metallic behavior. At approximately 35 K, there is an upturn in the resistivity that saturates at around 3 K. This feature is followed by an increase in resistivity values with decreasing temperature from the resistivity minimum. Once again, this minimum in the low temperature resistivity is thought to be caused by scattering of conduction electrons off the local magnetic moments on Mn.

2.4. Summary

The synthesis of $Yb(MnAl)_{12}$ adopting the $ThMn_{12}$ structure type and its substitutional derivative of the $CaCr_2Al_{10}$ structure type, have been studied. While the two structure types are very similar, subtle differences are observed in the magnetic susceptibilities of these compounds. Structurally ordered $LnMn_4Al_8$ compounds that adopt the $ThMn_{12}$ structure type have been found to order antiferromagnetically at low temperatures as a result of weak Ln-Ln interactions.[1] These compounds may be synthesized with larger Mn concentrations in which case Mn occupies the 8*f* and 8*j* positions preferentially. In these cases magnetic moments are observed on the additional Mn atoms (in the 8*f* and 8*j* positions). For $LnMn_{2+x}Al_{10-x}$ adopting the $CaCr_2Al_{10}$ structure type, magnetic moments are attributed to Mn atoms on the 8*i* position.

Our work to synthesize $ThMn_{12}$-type Yb-Mn-Al crystals has produced $YbMn_{2+x}Al_{10-x}$ single crystals of the $ThMn_{12}$-type and the $CaCr_2Al_{10}$-type. $YbMn_{2.55(4)}Al_{9.45(4)}$ in the $ThMn_{12}$ structure type displays paramagnetic behavior down to 3 K, as do $YbMn_{2+x}Al_{10-x}$ compounds in the $CaCr_2Al_{10}$-type. The magnetic moment for $YbMn_{2.55(4)}Al_{9.45(4)}$ ($ThMn_{12}$-type) is 4.2(4) μ_B, which is close to the calculated moment for Yb^{3+} (4.54 μ_B). The magnetic moments for the $CaCr_2Al_{10}$-type analogues are 1.3(4) μ_B (x = 0.06(4)) and 1.54(13) (x = 0.21(4)), values well below the calculated moment for Yb^{3+}. This detail, coupled with the corresponding lattice parameters for these compounds, is an indication of ytterbium being either in a divalent or

intermediate valent state. While the possible presence of divalent Yb in these compounds is intriguing due to the implications of manganese carrying a magnetic moment, it is a hypothesis that still requires additional experiments to verify. Utilizing X-ray photoelectron spectroscopy or X-ray absorption near edge spectroscopy would be of interest as far as elucidating the specific roles of ytterbium and manganese in the magnetism of these compounds.

2.5 References

(1) Suski, W.; Gschneidner Jr, K. A.; Eyring, L. In *Handbook on the Physics and Chemistry of Rare Earths*; Gschneidner Jr, K. A., Eyring, L., Eds.; Elsevier: Amsterdam, 1996; Vol. 22, p 143.

(2) Buschow, K. H. J.; Van, V. J. H. N.; Van, d. H. W. W. *J. Less-Common Met.* **1976**, *50*, 145.

(3) Yanson, T. I.; Manyako, N. B.; Bodak, O. I.; Cerny, R.; Gladyshevskii, R. E.; Yvon, K. *J. Alloys Compd.* **1995**, *219*, 219.

(4) Kotur, B. Y.; Palasyuk, A. M.; Bauer, E.; Michor, H.; Hilscher, G. *J. Phys.: Condens. Matter* **2001**, *13*, 9421.

(5) Drake, B. L.; Capan, C.; Cho, J. Y.; Nambu, Y.; Kuga, K.; Xiong, Y. M.; Karki, A. B.; Nakatsuji, S.; Adams, P. W.; Young, D. P.; Chan, J. Y. *J. Phys.: Condens. Matter* **2010**, *22*, 066001/1.

(6) Palasyuk, A. M.; Kotur, B. Y.; Bauer, E.; Michor, H.; Hilscher, G. *J. Alloys Compd.* **2004**, *367*, 205.

(7) Thiede, V. M. T.; Jeitschko, W. *Z. Naturforsch. B* **1998**, *53*, 673.

(8) Sefat, A. S.; Li, B.; Bud'ko, S. L.; Canfield, P. C. *Phys. Rev. B* **2007**, *76*, 174419/1.

(9) Duong, N. P.; Klaasse, J. C. P.; Brück, E.; de Boer, F. R.; Buschow, K. H. J. *J. Alloys Compd.* **2001**, *315*, 28.

(10) Felner, I., Nowik, I. *Phys. Chem. Solids* **1979**, *40*, 1035.

(11) Altomare, A.; Burla, M. C.; Camalli, M.; Cascarano, G. L.; Giacovazzo, C.; Guagliardi, A.; Moliterni, A. G. G.; Polidori, G.; Spagna, R. *J. Appl. Crystallogr.* **1999**, *32*, 115.

(12) Sheldrick, G. *Acta Cryst. A* **2008**, *64*, 112.

(13) Moze, O., Ibberson, R. M., Buschow, K. H. J. *J. Phys.: Condens. Matter* **1990**, *2*, 1677.

(14) Shirotani, I.; Araseki, N.; Shimaya, Y.; Nakata, R.; Kihou, K.; Sekine, C.; Yagi, T. *J. Phys.: Condens. Matter* **2005**, *17*, 4383.

(15) Sarrao, J. L.; Immer, C. D.; Fisk, Z.; Booth, C. H.; Figueroa, E.; Lawrence, J. M.; Modler, R.; Cornelius, A. L.; Hundley, M. F.; Kwei, G. H.; Thompson, J. D.; Bridges, F. *Phys. Rev. B* **1999**, *59*, 6855.

(16) Mazet, T.; Ihou-Mouko, H.; Ryan, D. H.; Voyer, C. J.; Cadogan, J. M.; Malaman, B. *J. Phys.: Condens. Matter* **2010**, *22*, 116005/1.

(17) Stelmakhovych, O.; Stelmakhovych, B.; Uhlirova, K.; Maskova, S.; Havela, L.; Kalychak, Y. *J. Solid State Chem.* **2011**, *184*, 1715.

(18) Wu, G.; Chen, H.; Wu, T.; Xie, Y. L.; Yan, Y. J.; Liu, R. H.; Wang, X. F.; Ying, J. J.; Chen, X. H. *J. Phys.: Condens. Matter* **2008**, *20*, 422201/1.

(19) Zhao, J.-T.; Schnelle, W.; Grin, Y. *J. Solid State Chem.* **2002**, *163*, 113.

(20) Coldea, M.; Coldea, R.; Borodi, G. *IEEE Trans. Magn.* **1994**, *30*, 855.

(21) Wada, H.; Nakamura, H.; Yoshimura, K.; Shiga, M.; Nakamura, Y. *J. Magn. Magn. Mater.* **1987**, *70*, 134.

CHAPTER 3. SYNTHESIS, STRUCTURE, AND MAGNETIC AND ELECTRICAL PROPERTIES OF $Yb(Mn,M)_xAl_{12-x}$ (M = Fe, Ru; $x \leq 2.5$) PHASES[*]

3.1 Introduction

LnM_xAl_{12-x}[1-11] (Ln = Y, La-Sm, Gd-Lu; M = Mn, Fe) compounds crystallizing in the $ThMn_{12}$ structure type[12] and the structurally related $CaCr_2Al_{10}$[13] (Ln = La, Gd, Yb; M = Mn) and $YbFe_2Al_{10}$[14] (Ln = Y, La-Sm, Gd-Lu; M = Fe, Ru) structure types, represent a group of chemically robust compounds.[15-22] These compounds are particularly interesting because they exhibit a rich variety of chemistry and physics. In particular, Ln-M-Al (Ln = lanthanide, M = Mn or Fe) compounds adopting the $ThMn_{12}$ structure type are known to exhibit a wide range of atomic compositions, from being highly rich in transition metal ($LnMn_{12-x}Fe_x$, x = 0-8)[23] to highly Al-rich ($YbMn_{2.55(4)}Al_{9.45(4)}$).[24] When the amount of transition metal is sufficiently reduced (for LnM_xAl_{12-x}, $x \sim 2$) compounds adopt either the $CaCr_2Al_{10}$ structure type or the $YbFe_2Al_{10}$ structure type dependent on the transition metal ($CaCr_2Al_{10}$-type for M = Mn, and $YbFe_2Al_{10}$-type for M = Fe).

Motivation to grow single crystals of ternary LnM_xAl_{12-x} (Ln = lanthanide, M = Mn or Fe) compounds lies in probing a rich variety of physical phenomena.[25] It has been shown that variability of M concentrations in LnM_xAl_{12-x} compounds of the $ThMn_{12}$ structure type can impact their magnetic properties.[8,10,22,26-27] The diverse nature of magnetism in these compounds, in addition to interesting behavior such as negative magnetoresistance,[6] points to complex interplay between possibly competing exchange interactions as exhibited in YFe_xMn_{12-x},[28] $ErFe_xMn_{12-x}$,[29] $DyFe_6Al_6$,[30] and many others.[31-36] In Fe-rich compounds such as $GdFe_6Al_6$

---

[*] Reprinted with permission from Fulfer, B. W.; McAlpin, J. D.; Haldolaarachchige, N.; Young, D. P.; Chan, J. Y., Synthesis, structure, and magnetic and electrical properties of $Yb(Mn,M)_xAl_{12-x}$ (M = Fe, Ru; $x \leq 2.5$) Phases. *Cryst. Growth Des.* **2013,** *13* (4), 1543-1550. Copyright 2013 American Chemical Society.

and $GdFe_4Al_8$ ($ThMn_{12}$ structure), Fe-Fe interactions result in high ordering temperatures (ferromagnetic order at T_C ~ 345 K for $GdFe_6Al_6$[8] and at T_C ~ 172 K for $GdFe_4Al_8$[27]). Alternatively, for $LnFe_2Al_{10}$ ($YbFe_2Al_{10}$-type) compounds with magnetic lanthanides (Ln = Sm-Tm), ordering temperatures are much lower (< 20 K) and magnetic interactions are attributed to the lanthanide sublattice.[15] Magnetic behavior in these compounds show extreme sensitivity to transition metal content.

We aim to understand the structural stability of $Yb(Mn,Fe)_xAl_{12-x}$ compounds of the $CaCr_2Al_{10}$, $ThMn_{12}$, and $YbFe_2Al_{10}$ structure types and $Yb(Mn,Ru)_xAl_{12-x}$ compounds adopting the $CaCr_2Al_{10}$ and $YbFe_2Al_{10}$ structure types by varying the concentration of the transition metals. Additionally, growing single crystals enables the intrinsic characterization of magnetic and electrical properties of these phases. In this manuscript we compare structural stabilities and experimental growth parameters used to obtain compounds in one structure type over another. Magnetic and electric transport properties are also presented and discussed.

3.2 Experimental

3.2.1 Synthesis

Elemental Yb, M (M = Mn and Fe or Ru), and Al (all > 99.9%) were utilized in all growths. Total weights of reactants for all reactions ranged from approximately 1.0-1.2 g. It was necessary to combine elements in reaction ratios of 1:4:30 Yb:M:Al to form compounds adopting the $ThMn_{12}$ structure type while combining elements in reaction ratios of 1:3:30 Yb:M:Al resulted in growth of compounds in the $YbFe_2Al_{10}$ and $CaCr_2Al_{10}$ structure types. The ratios of Mn/Fe and Mn/Ru were varied in reaction ratios of 1:3 Yb:M to study the impact of concentration on structural stability. The elements were combined into an alumina crucible which was then placed in a fused silica tube, evacuated, and backfilled with ~1/4 atm of Ar. The sealed tubes were heated to 1000 °C at 50 °C/h, allowed to dwell for 48 h, cooled to 850 °C at 5

°C/h, and centrifuged to remove excess aluminum. These reactions produced single crystals with rod-like morphologies in the case of $ThMn_{12}$ and $CaCr_2Al_{10}$-type compounds (the longest crystal was approximately 2 mm in length), and cube-like polyhedra for $YbFe_2Al_{10}$-type compounds (the largest crystal was approximately 1.5 mm along a face). All products appeared to be air stable for several months. Single crystals adopting the $YbFe_2Al_{10}$ structure type are stable in dilute (~ 0.1-0.5 M) HCl solution and unstable in dilute (~ 0.1-0.5) NaOH solution used to etch away excess aluminum. Alternatively, single crystals adopting the $CaCr_2Al_{10}$ and $ThMn_{12}$ structure types are stable in dilute NaOH solution.

3.2.2 Structure Determination

Structural characterization and phase identification were conducted via single crystal X-ray diffraction. Phase identification was performed on ground single crystals (before etching) with a Bruker AXS D8 Advance diffractometer equipped with a Cu Kα source (λ = 1.5418 Å) and a Ge monochromator. Samples for single crystal analysis were selected, cut to appropriate size, and mounted on glass fibers with epoxy. Single crystal diffraction data were collected on an Enraf Nonius Kappa CCD single crystal X-ray diffractometer with Mo Kα radiation (λ = 0.72073 Å) at room temperature. Crystal structures were solved by direct methods using SIR97[37] and refined with SHELXL97.[38] The final models were corrected for extinction, and the atomic displacement parameters were modeled anisotropically. Crystallographic parameters and atomic positions are provided for Mn:Fe and Mn:Ru compounds in Tables 3.1a-b and 3.2a-b, respectively, and interatomic distances are provided as supplementary information. Refined occupancies agreed well with results from energy dispersive spectroscopy and inductively coupled plasma optical emission spectroscopy.

Table 3.1a. Crystallographic data for $Yb(Mn,Fe)_xAl_{12-x}$

Crystal data			
Formula	$\mathbf{YbMn_{2.21(5)}Fe_{0.280(5)}Al_{9.51(8)}}$	$\mathbf{YbMn_{2.05(3)}Fe_{0.27(2)}Al_{9.68(3)}}$	$\mathbf{YbMn_{0.82(12)}Fe_{1.18(12)}Al_{10}}$
Nominal ratio (Mn:Fe)	3:1	2.5:0.5	1.5:1.5
Space group	*I4/mmm*	*P4/nmm*	*Cmcm*
Structure type	$ThMn_{12}$	$CaCr_2Al_{10}$	$YbFe_2Al_{10}$
a (Å)	8.968(2)	12.7320(10)	8.9852(10)
b (Å)	8.968(2)	12.7320(10)	10.2040(12)
c (Å)	5.105(2)	5.1123(5)	9.0288(10)
V (Å^3)	410.6(2)	828.72(12)	827.81(16)
Z	2	4	4
Crystal size (mm^3)	0.04 x 0.06 x 0.08	0.05 x 0.08 x 0.10	0.05 x 0.05 x 0.15
Temperature (K)	294(1)	294(1)	294(1)
Density (g cm^{-3})	4.584	4.502	4.444
θ Range (°)	3.21-33.33	2.26-33.12	3.02-34.08
μ (mm^{-1})	16.041	15.661	15.455
Data Collection and Refinement			
Collected reflections	411	2982	1567
Unique reflections	248	881	892
R_{int}	0.0150	0.0216	0.0158
h	$0 \le h \le 13$	$-19 \le h \le 19$	$-13 \le h \le 13$
k	$-9 \le k \le 9$	$-13 \le k \le 13$	$-15 \le k \le 15$
l	$0 \le l \le 7$	$-7 \le l \le 7$	$-13 \le l \le 13$
$\Delta\rho_{max}$ (e Å^{-3})	0.990	1.819	4.217
$\Delta\rho_{min}$ (e Å^{-3})	-1.054	-2.272	-3.122
GoF	1.095	1.046	1.097
Extinction coefficient	0.0017(4)	0.0053(4)	0.0058(3)
[a] $R_1(F)$ for $F_o^2 > 2\sigma(F_o^2)$	0.0177	0.0260	0.0255
[b] $R_w(F_o^2)$	0.0357	0.0664	0.0632

[a] $R_1 = \Sigma||F_o| - |F_c||/\Sigma|F_o|$
[b] $wR_2 = [\Sigma w(F_o^2 - F_c^2)^2/\Sigma w(F_o^2)^2]^{1/2}$; $w = 1/[\sigma^2(F_o^2) + 0.0096P^2 + 3.5053P]$, $w = 1/[\sigma^2(F_o^2) + 0.0427P^2 + 0.6620P]$, and $w = 1/[\sigma^2(F_o^2) + 0.0420P^2 + 2.1159\ P]$, and at 294 K for $YbMn_{2.21(5)}Fe_{0.280(5)}Al_{9.51(8)}$, $YbMn_{2.05(3)}Fe_{0.27(2)}Al_{9.68(3)}$, and $YbMn_{0.82(12)}Fe_{1.18(12)}Al_{10}$, respectively.

3.2.3 Elemental Analysis

Elemental analysis was performed on samples of polished crystals via energy dispersive spectroscopy (EDS) using an EDAX detector equipped to a FEI Quanta 200 scanning electron microscope with an accelerating voltage of 15 kV. Spectra were integrated for at least 30 seconds, and the results from at least 5 spots were averaged to determine relative amounts of transition metals in atomic percentage of at least three different samples per structure type. Relative percentages for the transition metals were determined by normalizing the atomic percent of each transition metal to the total atomic percent for both transition metals. Standard deviation in the measurements of the atomic percentages is reported as uncertainty. The relative atomic

Table 3.1b. Atomic positions for $Yb(Mn,Fe)_xAl_{12-x}$

Atom	Wyckoff position	x	y	z	$^aU_{eq}$ (Å^2)
$YbMn_{2.21(5)}Fe_{0.280(5)}Al_{9.51(8)}$ ($ThMn_{12}$-type)					
Yb	2*a*	0	0	0	0.00706(13)
M	8*f* (55(1)%Mn+38(2)%Al +7(1)%Fe)	1/4	1/4	1/4	0.0065(3)
Al1	8*i*	0.34667(16)	0	0	0.0087(3)
Al2	8*j*	0.28138(18)	1/2	0	0.0099(3)
$YbMn_{2.05(3)}Fe_{0.27(2)}Al_{9.68(3)}$ ($CaCr_2Al_{10}$-type)					
Yb1	2*c*	1/4	1/4	0.52129(7)	0.00993(13)
Yb2	2*a*	3/4	1/4	0	0.01090(14)
M1	8*i* (86(1)%Mn+14(1)%Fe)	1/4	0.50677(4)	0.25191(9)	0.00888(15)
Al1	8*j*	0.07603(9)	*x*	0.4845(2)	0.0119(3)
Al2	8*j*	0.14262(8)	*x*	0.0302(2)	0.0108(3)
M3	8*i* (83(1)%Al+16(1)%Mn)	1/4	0.00861(8)	0.74932(16)	0.0096(3)
Al4	8*h*	0.36130(8)	-*x*	1/2	0.0106(3)
Al5	8*g*	0.42408(9)	-*x*	0	0.0115(3)
$YbMn_{0.82(12)}Fe_{1.18(12)}Al_{10}$ ($YbFe_2Al_{10}$-type)					
Yb	4*c*	0	0.12489(2)	1/4	0.00728(11)
M	8*d* (59(6)%Fe+41(6)%Mn)	1/4	1/4	0	0.00516(16)
Al1	8*g*	0.22716(17)	0.36093(12)	1/4	0.0070(2)
Al2	8*g*	0.34635(17)	0.12746(11)	1/4	0.0075(2)
Al3	8*f*	0	0.15418(13)	0.59546(16)	0.0072(2)
Al4	8*f*	0	0.37423(11)	0.04453(18)	0.0084(3)
Al5	8*e*	0.22808(15)	0	0	0.0062(2)

$^aU_{eq}$ is defined as one-third of the trace of the orthagonalized U_{ij} tensor.

percentages for the Mn and Fe compounds are as follows: compounds adopting the $YbFe_2Al_{10}$ structure type contain 47(4) % Mn to 53(3) % Fe, compounds adopting the $ThMn_{12}$ structure type contain 22(6) % Fe to 78(9) % Mn, and compounds adopting the $CaCr_2Al_{10}$ structure type contain 14(1) % Fe to 86(4) % Mn. The relative atomic percentages for the Mn and Ru compounds are as follows: compounds adopting the $YbFe_2Al_{10}$ structure type contain 23(3) % Mn to 77(11) % Ru, and compounds adopting the $CaCr_2Al_{10}$ structure type contain 11(3) % Ru to 89(17) % Mn.

Table 3.2a. Crystallographic data for $Yb(Mn,Ru)_xAl_{12-x}$

Crystal data			
Formula	$\mathbf{YbMn_{0.44(4)}Ru_{1.56(4)}Al_{10}}$	$\mathbf{YbMn_{0.42(4)}Ru_{1.58(4)}Al_{10}}$	$\mathbf{YbMn_{1.95(4)}Ru_{0.21(4)}Al_{9.85(4)}}$
Nominal ratio (Mn:Ru)	1:1	2:1	5:1
Structure Type	$YbFe_2Al_{10}$	$YbFe_2Al_{10}$	$CaCr_2Al_{10}$
Space group	*Cmcm*	*Cmcm*	*P4/nmm*
a (Å)	9.071(2)	9.0696(12)	12.761(2)
b (Å)	10.225(3)	10.2211(16)	12.761(2)
c (Å)	9.102(2)	9.1028(6)	5.1194(15)
V (Å^3)	844.2(4)	843.9(2)	833.6(3)
Z	4	4	4
Crystal size (mm^3)	0.04 x 0.10 x 0.10	0.04 x 0.10 x 0.17	0.04 x 0.04 x 0.06
Temperature (K)	294(1)	294(1)	294(1)
Density (g cm^{-3})	4.914	4.925	4.515
θ Range (°)	3.00-30.01	3.00-30.04	3.19-30.03
μ (mm^{-1})	15.349	15.363	15.350
Data Collection and Refinement			
Collected reflections	1173	1171	1814
Unique reflections	676	682	700
R_{int}	0.0289	0.0379	0.0497
h	$-12 \le h \le 12$	$-12 \le h \le 12$	$-17 \le h \le 17$
k	$-14 \le k \le 14$	$-14 \le k \le 14$	$-12 \le k \le 12$
l	$-12 \le l \le 12$	$-12 \le l \le 12$	$-7 \le l \le 5$
$\Delta\rho_{max}$ (e Å^{-3})	2.198	3.984	1.579
$\Delta\rho_{min}$ (e Å^{-3})	-1.425	-1.648	-1.325
GoF	1.131	1.110	1.019
Extinction coefficient	0.00422(17)	0.00061(7)	0.0041(3)
[a] $R_1(F)$ for $F_o^2 > 2\sigma(F_o^2)$	0.0253	0.0303	0.0283
[b] $R_w(F_o^2)$	0.0486	0.0469	0.0531

[a] $R_1 = \Sigma||F_o| - |F_c||/\Sigma|F_o|$
[b] $wR_2 = [\Sigma w(F_o^2 - F_c^2)^2/\Sigma w(F_o^2)^2]^{1/2}$; $w = 1/[\sigma^2(F_o^2) + 0.0150P^2]$, $w = 1/[\sigma^2(F_o^2) + 0.0082P^2 + 1.4026P]$, and $w = 1/[\sigma^2(F_o^2) + 0.0144P^2]$ at 294 K for $YbMn_{0.44(4)}Ru_{1.57(4)}Al_{10}$, $YbMn_{0.42(4)}Ru_{1.58(4)}Al_{10}$, and $YbMn_{1.95(4)}Ru_{0.21(4)}Al_{9.85(4)}$, respectively.

3.2.4 Magnetization and Electrical Transport

A Quantum Design Physical Property Measurement System (PPMS) was used to obtain magnetic data. Single crystal samples were thoroughly characterized prior to physical property measurements. A combination of elemental analysis followed by multiple rounds of single crystal X-ray diffraction consisting of unit cell checks taken from multiple points on the crystal, in addition to a full data collection, were utilized to ensure crystal homogeneity. Temperature-dependent magnetic susceptibility was measured under zero-field-cooled (ZFC) conditions from 3 to 300 K with an applied field of 3 T. Electrical resistivity data were collected via a standard four-probe AC technique using the PPMS from 3 K to 300 K.

Table 3.2b. Atomic positions for $Yb(Mn,Ru)_xAl_{12-x}$

Atom	Wyckoff position	x	y	z	$^aU_{eq}$ (Å^2)
$YbMn_{0.44(4)}Ru_{1.56(4)}Al_{10}$ ($YbFe_2Al_{10}$-type)					
Yb	4*c*	0	0.12516(3)	1/4	0.00867(15)
M	8*d* (78(1)%Ru+22(1)%Mn)	1/4	1/4	0	0.0055(2)
Al1	8*g*	0.2235(2)	0.36284(18)	1/4	0.0083(4)
Al2	8*g*	0.3473(2)	0.12890(17)	1/4	0.0093(4)
Al3	8*f*	0	0.15454(18)	0.5982(2)	0.0089(4)
Al4	8*f*	0	0.37536(17)	0.0457(2)	0.0097(4)
Al5	8*e*	0.2259(2)	0	0	0.0084(4)
$YbMn_{0.42(4)}Ru_{1.58(4)}Al_{10}$ ($YbFe_2Al_{10}$-type)					
Yb	4*c*	0	0.12512(5)	1/4	0.01018(16)
M	8*d* (79(1)%Ru+21(1)%Mn)	1/4	1/4	0	0.0066(2)
Al1	8*g*	0.2235(3)	0.3625(2)	1/4	0.0101(5)
Al2	8*g*	0.3471(2)	0.1286(2)	1/4	0.0084(5)
Al3	8*f*	0	0.1545(2)	0.5981(2)	0.0099(5)
Al4	8*f*	0	0.3755(2)	0.0454(3)	0.0105(5)
Al5	8*e*	0.2261(2)	0	0	0.0079(4)
$YbMn_{1.95(4)}Ru_{0.21(4)}Al_{9.85(4)}$ ($CaCr_2Al_{10}$-type)					
Yb1	2*c*	1/4	1/4	0.52340(12)	0.0077(3)
Yb2	2*a*	3/4	1/4	0	0.0084(3)
M1	8*i* (90(1)%Mn+10(1)%Ru)	1/4	0.50696(12)	0.2519(2)	0.0068(3)
Al1	8*j*	0.0757(2)	*x*	0.4841(3)	0.0085(7)
Al2	8*j*	0.1430(2)	*x*	0.0314(4)	0.0098(7)
M3	8*i* (92(1)%Al+8(1)%Mn)	1/4	0.0096(2)	0.7491(4)	0.0055(6)
Al4	8*h*	0.3617(2)	-*x*	1/2	0.0076(7)
Al5	8*g*	0.4241(2)	-*x*	0	0.0099(8)

$^aU_{eq}$ is defined as one-third of the trace of the orthagonalized U_{ij} tensor.

3.3 Results and Discussion

3.3.1 Synthesis and Structure

3.3.1.1 $Ln(Mn,Fe)_xAl_{12-x}$ (Ln = Y, Yb)

Synthesis of $Yb(Mn,Fe)_xAl_{12-x}$ compounds yielded products in three different structure types; the $ThMn_{12}$-type and its two derivatives, the $CaCr_2Al_{10}$-type and the $YbFe_2Al_{10}$-type. $Yb(Mn,Fe)_xAl_{12-x}$ compounds that adopt the $ThMn_{12}$ structure type (Figure 3.1a) designated as compound **1** crystallize in the tetragonal space group *I*4/*mmm* (139). The $ThMn_{12}$ structure type has been extensively studied and is structurally related to the $CaCu_5$ structure type.[39-40] Yb atoms occupy the 2*a* position, while M (Mn, Fe, and Al) occupies the 8*f* position, and Al atoms

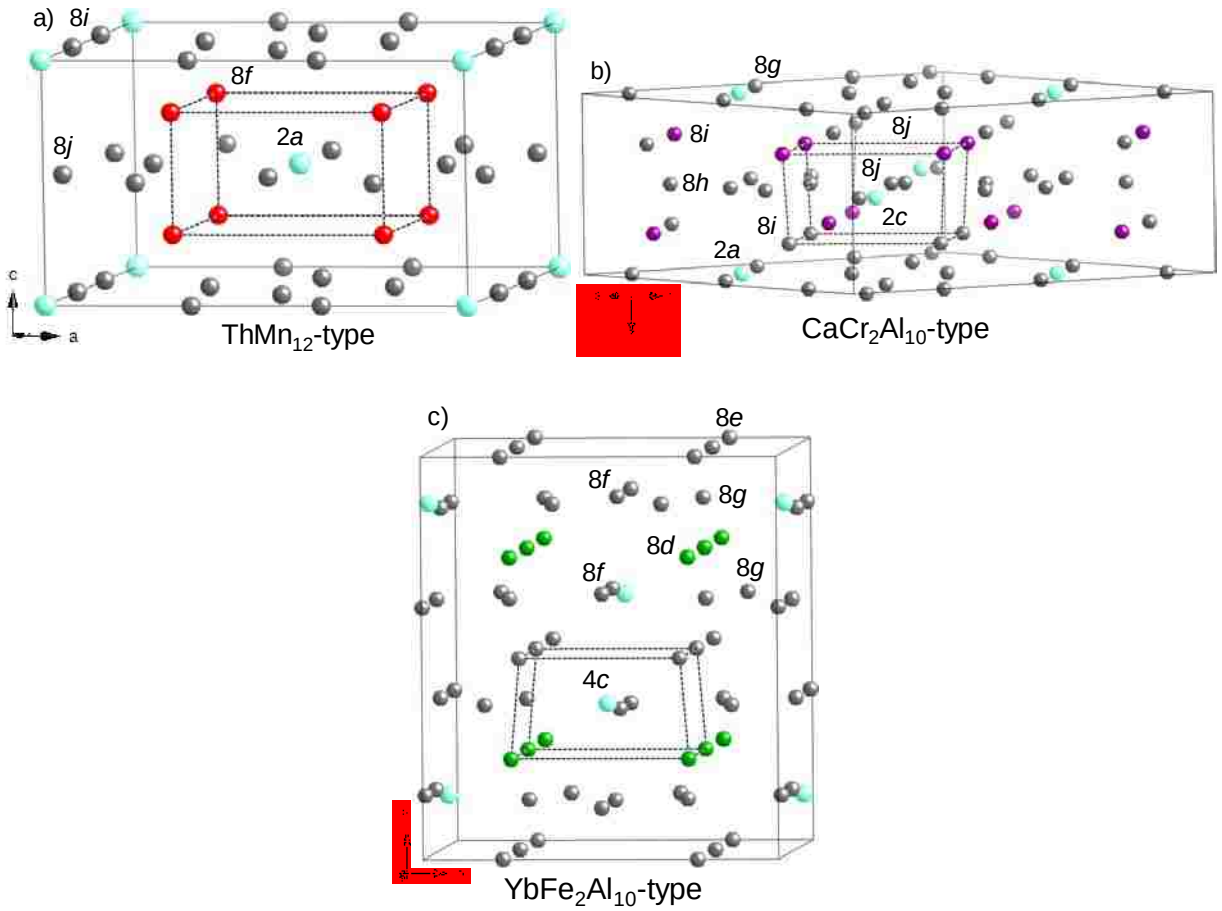

Figure 3.1. a) A representation of the $ThMn_{12}$ structure type. The 2*a* position is depicted by light blue spheres, while the 8*f* position is depicted by red spheres, and the 8*i* and 8*j* positions are shown as dark grey spheres. b) Also shown is a representation of the $CaCr_2Al_{10}$ structure type, where the 2*a* and 2*c* positions depicted by light blue spheres, while an 8*i* position is depicted by purple spheres, and 8*g*, 8*h*, 8*i*, and two 8*j* positions are depicted by dark grey spheres. c) Finally, the $YbFe_2Al_{10}$ structure type is represented, where the 4*c* position is depicted by light blue spheres, while the 8*d* position is depicted by green spheres, and 8*e*, two 8*f*, and two 8*g* positions are depicted by dark grey spheres.

occupy the 8*i* and 8*j* positions. Yb atoms are centered in 20-coordinate polyhedra shown in Figure 3.2a. These polyhedra are face-sharing in the c direction (via square faces consisting of Al atoms on the 8*j* position) and corner-sharing in the a and b directions (via M atoms on the 8*f* positions) to form corner sharing stacks that extend in the crystallographic c-direction. Interatomic distances for the Yb polyhedra are Yb-Al distances of 3.1089(16) Å (2*a*-8*i*) and 3.2108(13) Å (2*a*-8*j*), and Yb-M distances of 3.4179(10) Å (2*a*-8*f*). These distances are well

within expected distances for Yb-Al binaries such as $YbAl_2$ and $YbAl_3$ (~ 2.97-3.26 Å). Comparison of the unit cell volume obtained via single crystal X-ray diffraction (410.6(2) $Å^3$) to previously published data for $LnMn_4Al_8$ compounds shows the volume to be somewhere between what is reported for $NdMn_4Al_8$ (408.9(4) $Å^3$) and $PrMn_4Al_8$ (412.1(4) $Å^3$),[10] suggesting that Yb in this compound could be in a divalent state.

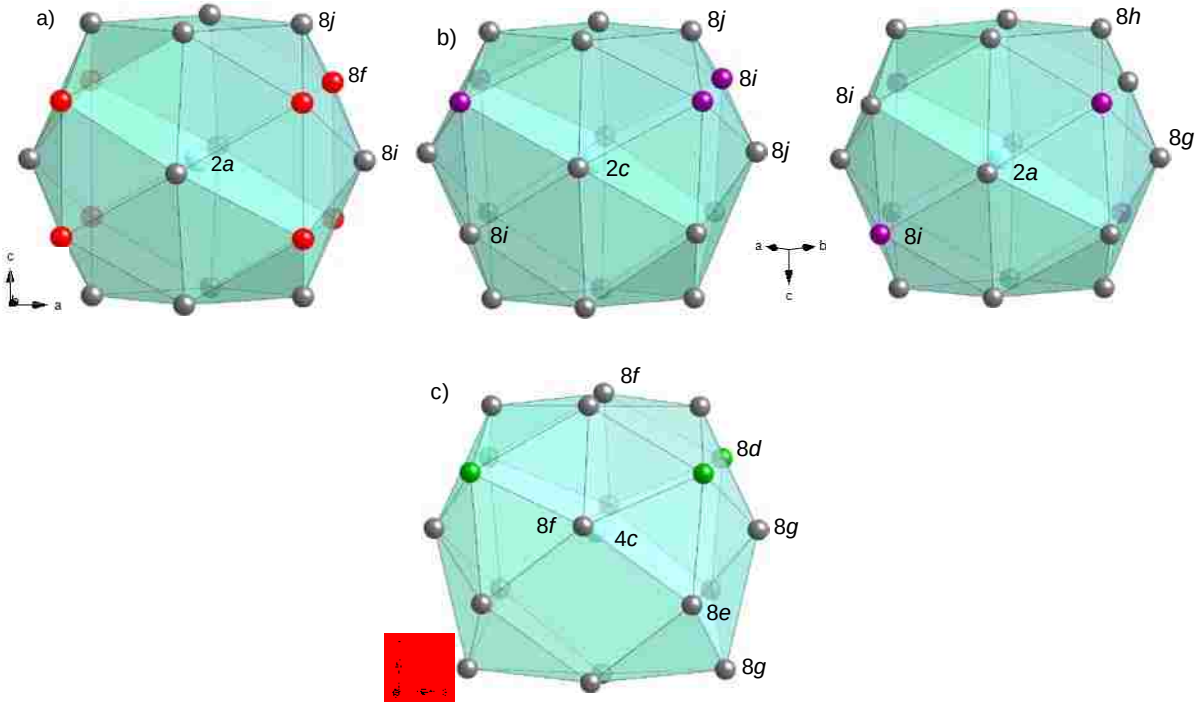

Figure 3.2. Coordination environment of Yb (light blue spheres) in the a) $ThMn_{12}$, b) $CaCr_2Al_{10}$, and c) $YbFe_2Al_{10}$ structure types. Red, purple, and green spheres represent positions that are preferentially occupied by transition metal atoms (given that sufficient amounts of transition metal are present in the reaction).

$Yb(Mn,Fe)_xAl_{12-x}$ compounds adopting the $CaCr_2Al_{10}$ and $YbFe_2Al_{10}$ structure types are variants of the $ThMn_{12}$ structure type. Products that adopt the $CaCr_2Al_{10}$ structure type (Figure 3.1b) designated as compound **2** crystallize in the tetragonal space group *P4/nmm* (129) and can be described as substitutional variants of LnM_4Al_8 ($ThMn_{12}$-type) where half of the M sites become Al sites. Yb atoms occupy the 2*c* and 2*a* positions, M (Mn, Fe, and Al) occupies the 8*i* positions, and Al occupies the two 8*j* sites, one 8*h*, and one 8*g* site. Yb atoms are situated in the

middle of 20-coordinate polyhedra (shown in Figure 3.2b) as with compounds adopting the $ThMn_{12}$ structure type. These polyhedra are face sharing in the c direction (via square faces consisting of Al atoms on the 8*j* positions) and corner sharing in the a and b directions (via M1 and M3 atoms on the 8*i* positions) similar to compounds adopting the $ThMn_{12}$ structure type. Interatomic distances for the Yb polyhedra range from 3.1381(12) Å to 3.5474(15) Å, which reflect the slight distortion of Yb polyhedra from the $ThMn_{12}$ structure to the $CaCr_2Al_{10}$ structure. The unit cell volume is 828.72(12) $Å^3$, which is close to what is reported for $GdMn_{2+x}Al_{12-x}$ compounds (V = 834.8(2) for x = 0.21(4); V = 831.5(2) $Å^3$ for x = 0.39(2)) with similar Mn concentration.[16] This suggests that Yb is in a divalent state in these compounds as well.

Alternatively, products adopting the $YbFe_2Al_{10}$ structure type (Figure 3.1c, designated as compound **3**) crystallize in the orthorhombic space group *Cmcm* (63) and can be described as substitutional and stacking variants of LnM_4Al_8 ($ThMn_{12}$-type). As with $ThMn_{12}$- and $CaCr_2Al_{10}$-type compounds, half the M sites are occupied by Al atoms. Yb atoms occupy the 4*c* position, M (Mn, Fe) atoms occupy the 8*d* site, and Al atoms occupy two 8*g* and 8*f* sites and one 8*e* site. Yb atoms are centered in 20-cordinate polyhedra (shown in Figure 3.2c) that stack in the c direction (via square faces consisting of Al atoms on the 8*e* and 8*f* positions) and are corner-sharing in the a and b directions (via Al atoms on the 8*g* positions). However, these polyhedra stack in a staggered fashion compared to Yb polyhedra in $ThMn_{12}$- and $CaCr_2Al_{10}$-type compounds. The Yb polyhedra distort from the $ThMn_{12}$ and $CaCr_2Al_{10}$ structure types, where shared square faces are parallel, to the $YbFe_2Al_{10}$ structure type, where shared square faces form an angle of approximately 121 ° with the center Yb (shown in Figure 3.3). Interatomic distances for the Yb polyhedra are 3.1121(16) Å to 3.6421(14) Å, which points to increased distortion in

the Yb polyhedra for $YbFe_2Al_{10}$-type compounds relative to $ThMn_{12}$- and $CaCr_2Al_{10}$-type compounds. The unit cell volume for compound **3** (827.81(16) $Å^3$) is larger than that reported for $YbFe_2Al_{10}$ (817.5(3) $Å^3$), which is reported to contain mixed or intermediate valent Yb. Similarly, Yb could be in a divalent state in compound **3**.

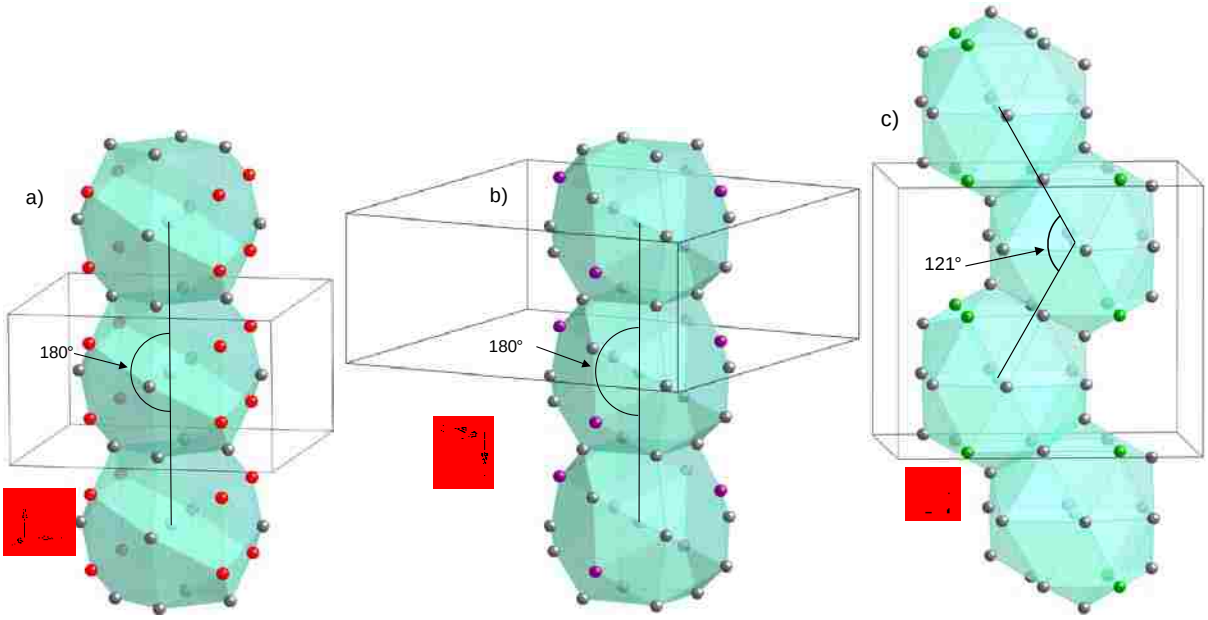

Figure 3.3. Columns of Yb polyhedra (light blue) for the a) $ThMn_{12}$, b) $CaCr_2Al_{10}$, and c) $YbFe_2Al_{10}$ structure types.

By changing the reaction ratios for Mn and Fe it is possible to obtain compounds in one structure type or the other (see Figure 3.4). A reaction ratio of 1:**3:1**:30 (Yb:Mn:Fe:Al) was necessary to obtain $Yb(Mn,Fe)_xAl_{12-x}$ (compound **1**) of the $ThMn_{12}$ structure type. For $YbMn_{2.21(8)}Fe_{0.28(8)}Al_{9.51(8)}$ the occupancies of Mn, Al, and Fe were refined on the 8*f* site resulting in 55(2)% Mn, 38(2)% Al, and 7(2)% Fe (Table 3.1b). Alternatively, reaction ratios of 1:3:30 (Yb:M:Al) were required to obtain compounds crystallizing in the $CaCr_2Al_{10}$ and $YbFe_2Al_{10}$ structure types. The most Mn-rich reaction (1:**2.5:0.5**:30 of Yb:Mn:Fe:Al) was required to grow $Yb(Mn,Fe)_{2+x}Al_{10-x}$ (compound **2**) in the $CaCr_2Al_{10}$ structure type while equal amounts of Mn

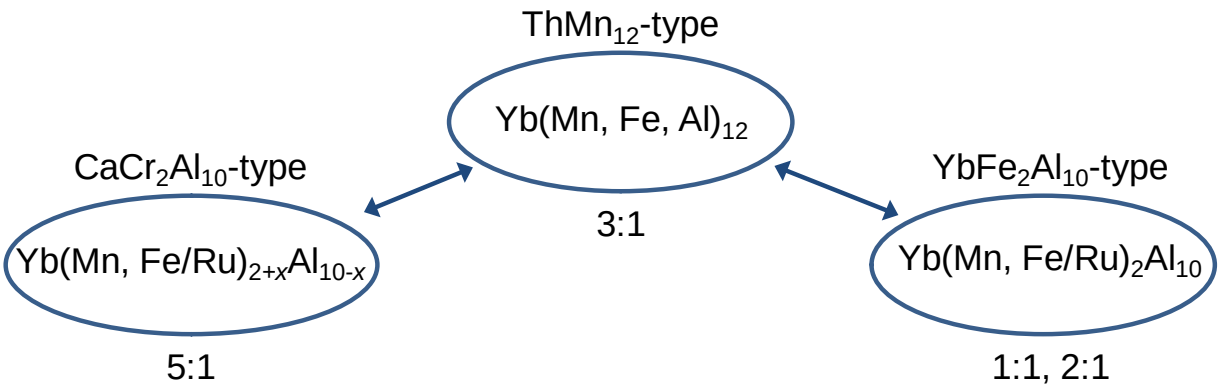

Figure 3.4. A diagram depicting the relationship between reaction ratio and product structure type. Reaction ratios are given in terms of Mn:Fe/Ru.

and Fe were used (1:**1.5:1.5**:30 Yb:Mn:Fe:Al) to grow $Yb(Mn,Fe)_2Al_{10}$ (compound **3**) in the $YbFe_2Al_{10}$ structure type. For compound **2**, refinement of the occupancy of the M 8*i* site and the M3 8*i* site resulted in a calculated stoichiometry of $YbMn_{2.05(3)}Fe_{0.27(2)}Al_{9.68(3)}$ (Table 3.1b), while for compound **3** refinement of the occupancy of the M 8*d* site for led to a calculated stoichiometry of $YbMn_{0.82(12)}Fe_{1.18(12)}Al_{10}$ (Table 3.1b). Results from EDS give Mn:Fe ratios that are in good agreement with these results, and normalized atomic ratios obtained from ICP-OES experiments agree within error with these calculated stoichiometries. Crystallographic data for these compounds are provided in Table 3.1a along with atomic positions in Table 3.1b. Attempts were made to synthesize Y, La, and Ca analogues of the above mentioned compounds resulting in the growth of $Y(Mn,Fe)_2Al_{10}$ analogues of the $YbFe_2Al_{10}$-type.

3.3.1.2 $Yb(Mn,Ru)_xAl_{12-x}$

Multiple attempts to synthesize $Yb(Mn,Ru)_xAl_{12-x}$ compounds adopting the $ThMn_{12}$ structure type with reaction ratios of **1:4**:30 (Yb:M:Al, M = Mn, Ru) were unsuccessful. Using reaction ratios of 1:3:30 (Yb:M:Al) yielded products in the $CaCr_2Al_{10}$ and $YbFe_2Al_{10}$ structure types. Reaction ratios of 1:**1.5:1.5**:30 and 1:**2:1**:30 of Yb-Mn-Ru-Al produced $Yb(Mn,Ru)_2Al_{10}$ with the $YbFe_2Al_{10}$ structure, while the Mn-rich reaction ratio of 1:**2.5:0.5**:30 Yb-Mn-Ru-Al

produced $Yb(Mn,Ru)_{2+x}Al_{10-x}$ with the $CaCr_2Al_{10}$ structure. Refinement of occupancies of the M 8*d* site for the analogues adopting the $YbFe_2Al_{10}$ structure led to calculated stoichiometries of $YbMn_{0.44(4)}Ru_{1.56(4)}Al_{10}$ and $YbMn_{0.42(4)}Ru_{1.58(4)}Al_{10}$ for the 1:**1.5:1.5**:30 and 1:**2:1**:30 reaction stoichiometries, respectively, while refinement of the occupancies of the M 8*i* site and the M3 8*i* site for the analogue adopting the $CaCr_2Al_{10}$ structure led to a calculated stoichiometry of $YbMn_{1.95(4)}Ru_{0.21(4)}Al_{9.85(4)}$. Compositions of Mn:Ru determined from EDS are in good agreement with the structural refinements. Crystals of these compounds were not large enough for physical property measurements. Crystallographic data for these compounds are given in Table 3.2a along with atomic positions in Table 3.2b.

3.3.2 Physical Properties

Temperature dependent magnetic susceptibility is shown for single crystalline samples of compounds **1** ($ThMn_{12}$-type) and **2** ($CaCr_2Al_{10}$-type) in Figure 3.5. The magnetic susceptibility was fit to a modified Curie-Weiss equation $\chi(T)=\chi_o+C/(T-\theta)$ where C represents the Curie constant, θ is the Weiss temperature, and χ_o is the temperature independent contribution to the susceptibility. All magnetic parameters are summarized in Table 3.3. Susceptibilities for both compounds exhibit paramagnetic behavior down to 3 K. The calculated effective moments are 2.11(12) μ_B/f.u. for compound **1** and 1.5(2) μ_B/f.u. for compound **2**, both of which are significantly less than the expected moment for Yb^{3+} (4.54 μ_B). Similar measurements performed on $LaMn_{2+x}Al_{10-x}$ compounds led to the conclusion that Mn carries a moment (μ_{eff} = 1.5(1) when x = 0.26(1); μ_{eff} = 1.9(1) when x = 0.41(3)),[16] and studies on $YbMn_{2+x}Al_{10-x}$ compounds revealed similar magnetic behavior to what is presented here,[24] indicating that Yb

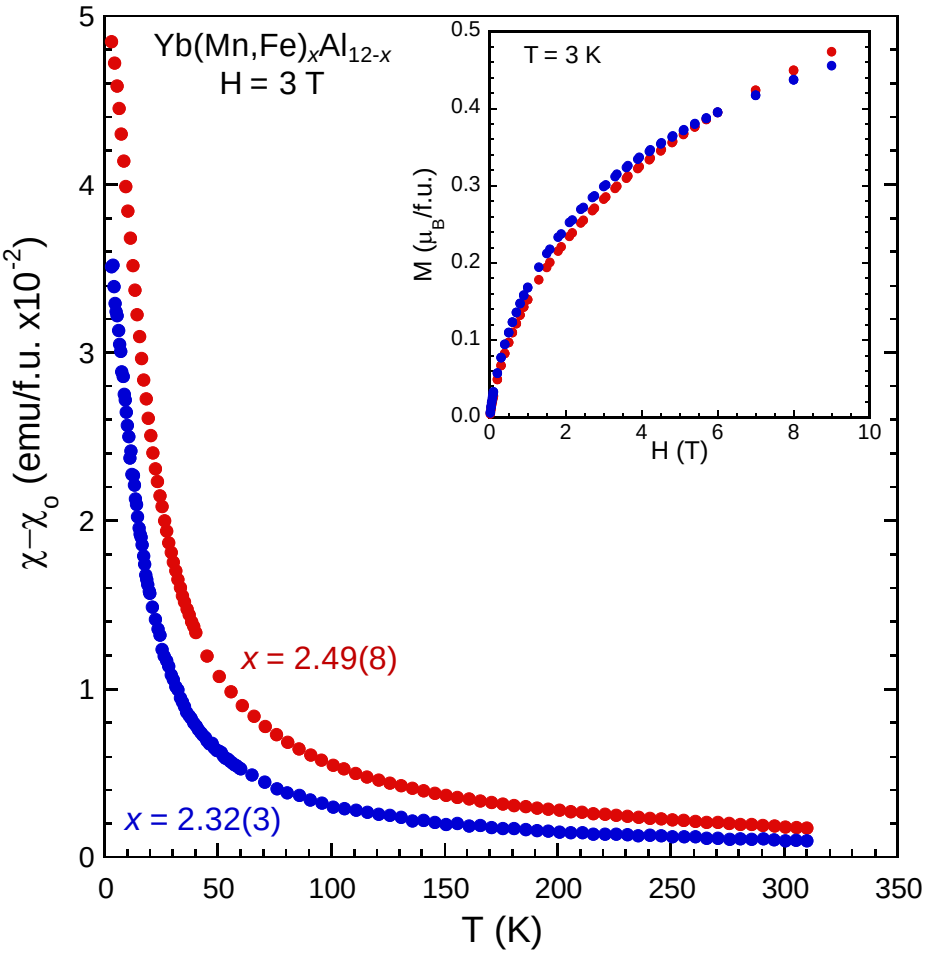

Figure 3.5. Magnetic susceptibility (emu/f.u.) of compounds **1** ($ThMn_{12}$-type, red) and **2** ($CaCr_2Al_{10}$-type, blue) as a function of temperature at an applied field of 3 T. The inset shows magnetization as a function of applied field for both compounds.

could be in a divalent state in compounds **1** ($ThMn_{12}$-type) and **2** ($CaCr_2Al_{10}$-type). It is interesting to note that the reported value of μ_{eff} for compound **1** (2.11(12) μ_B/f.u.) is significantly lower than what was reported for $YbMn_{2.55(4)}Al_{9.45(4)}$ (4.2(4) μ_B/f.u.), when the two compounds are isostructural ($ThMn_{12}$-type) and contain virtually the same amount of transition metal. Given that the La analogue of compound **1** has paramagnetic contributions from Mn and that the unit cell volume for compound **1** is larger than what is expected for an analogue containing trivalent Yb, it is likely that Mn is magnetic in compound **1**. The addition of non-magnetic Fe would account for the reduction of μ_{eff} from 4.2(4) μ_B/f.u. in $YbMn_{2.55(4)}Al_{9.45(4)}$ to

2.11(12) μ_B/f.u. in compound **1**. Alternatively, in the case that Yb is in a trivalent state in compound **1**, it is possible that the presence of Fe promotes valence instability in Yb, which would explain the reduction of μ_{eff} from the non-Fe-containing analogue. Magnetization as a function of applied field at 3 K is shown for both compounds (**1** and **2**) as an inset in Figure 3.5. No hysteresis or saturation is observed up to an applied field of 9 T.

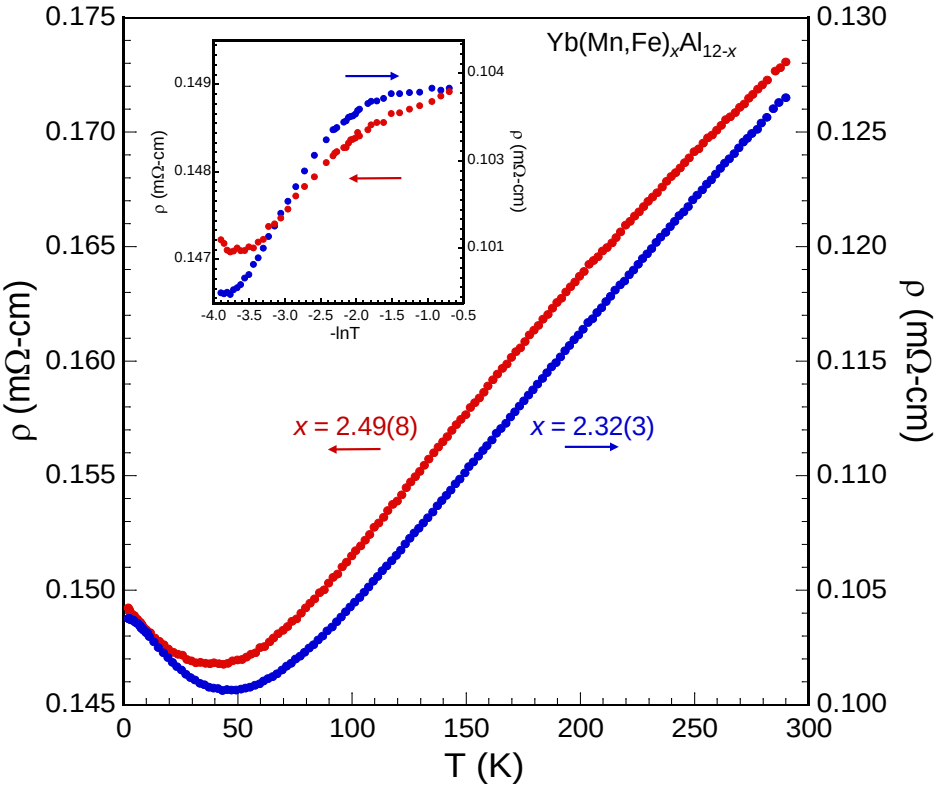

Figure 3.6. Electrical resistivity of compounds **1** ($ThMn_{12}$-type, red) and **2** ($CaCr_2Al_{10}$-type), blue). The inset shows electrical resistivity as a function of –lnT.

The electrical resistivity as a function of temperature for compounds **1** ($ThMn_{12}$-type) and **2** ($CaCr_2Al_{10}$-type) is shown in Figure 3.6. The overall trends in both compounds are similar; resistivity decreases as a function of temperature from the highest measured value of *T* down to about 43 K for compound **1** and about 47 K for compound **2**, at which point the resistivity increases with decreasing temperature. This behavior has been observed in similar $LnMn_{2+x}Al_{10-x}$ compounds (Ln = La,[16] Yb[24]) and has been explained as a possible development

of magnetic correlations at low temperatures.[16] The resistivity values below T = 50 K exhibit regions of linear behavior when plotted against –lnT (shown in inset of Figure 3.6), indicating possible Kondo interactions. Comparing the resistivity of compound **1** to that of its isostructural analogue $YbMn_{2.55(4)}Al_{9.45(4)}$,[24] the minimum in the resistivity decreases from around 100 K in $YbMn_{2.55(4)}Al_{9.45(4)}$ (un-doped) to around 43 K in compound **1** (Fe-doped). This can be explained in two ways. First, if Yb is closer to a divalent state in both compounds as suggested by larger than expected unit cell dimensions and volumes, Mn is contributing to the magnetism. When Fe is doped into the system, the magnetic moment is reduced from 4.2(4) μ_B/f.u. (for $YbMn_{2.55(4)}Al_{9.45(4)}$) to 2.11(12) μ_B/f.u (for compound **1**). Second, if Yb is in a trivalent state in the un-doped analogue, then the addition of Fe can potentially promote valence instability in Yb, thereby lowering the effective moment.

Temperature dependent magnetic susceptibility for compound **3** ($YbFe_2Al_{10}$-type) is shown in Figure 3.7. The data were fit to the modified Curie-Weiss equation, and the magnetic parameters are given in Table 3.3. The susceptibility exhibits paramagnetic behavior down to 3 K, and the calculated μ_{eff} is 0.66(10) μ_B/f.u. which is far below the calculated moment for Yb^{3+} (4.54 μ_B), and the reported μ_{eff} for a polycrystalline sample of isostructural $YbFe_2Al_{10}$ is 4.69 μ_B/f.u.[20] Such a large reduction in the magnetic moment is perhaps indicative of valence instability in Yb, as was shown for another growth of single crystalline $YbFe_2Al_{10}$, where the reported μ_{eff} was 0.6(1) μ_B/f.u.[15] Alternatively, the small μ_{eff} value reported here could be due to itinerant contributions from Mn and Fe if Yb is in a divalent state. Magnetization as a function of applied field at 3 K is shown for compound **3** in the inset of Figure 3.7. No hysteresis or saturation is observed up to an applied field of 9 T.

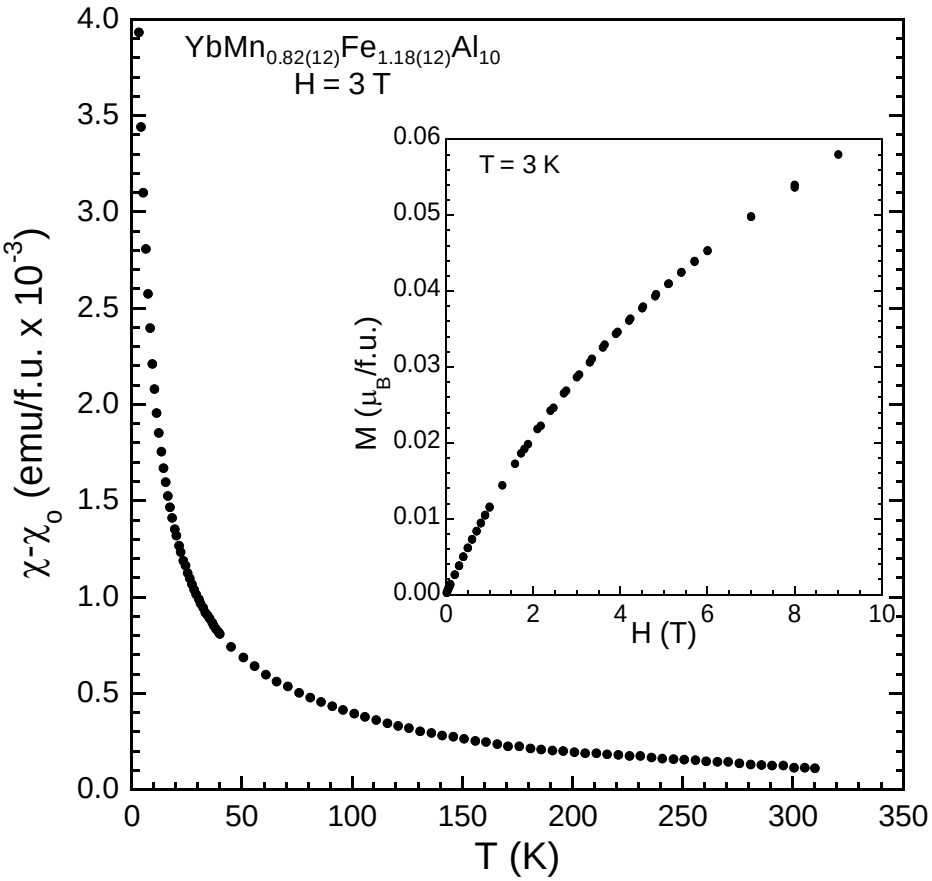

Figure 3.7. Magnetic susceptibility for compound **3** ($YbFe_2Al_{10}$-type) at an applied field of 3 T. Magnetization as a function of applied field is shown in the inset.

Electrical resistivity as a function of temperature for compound **3** ($YbFe_2Al_{10}$-type) is given in Figure 3.8. Resistivity shows metallic behavior from 290 K down to approximately 43 K, where a minimum in the resistivity is observed. Below 43 K the resistivity increases as temperature decreases. This trend is not unlike that observed for isostructural $YbFe_2Al_{10}$, which is postulated to exhibit weak Kondo coupling starting around 30 K.[20] Linear behavior can be observed in a plot of resistivity as a function of –lnT where T < 43 K (shown in inset of Figure 3.8), which indicates that compound **3** possibly displays the Kondo effect as well.

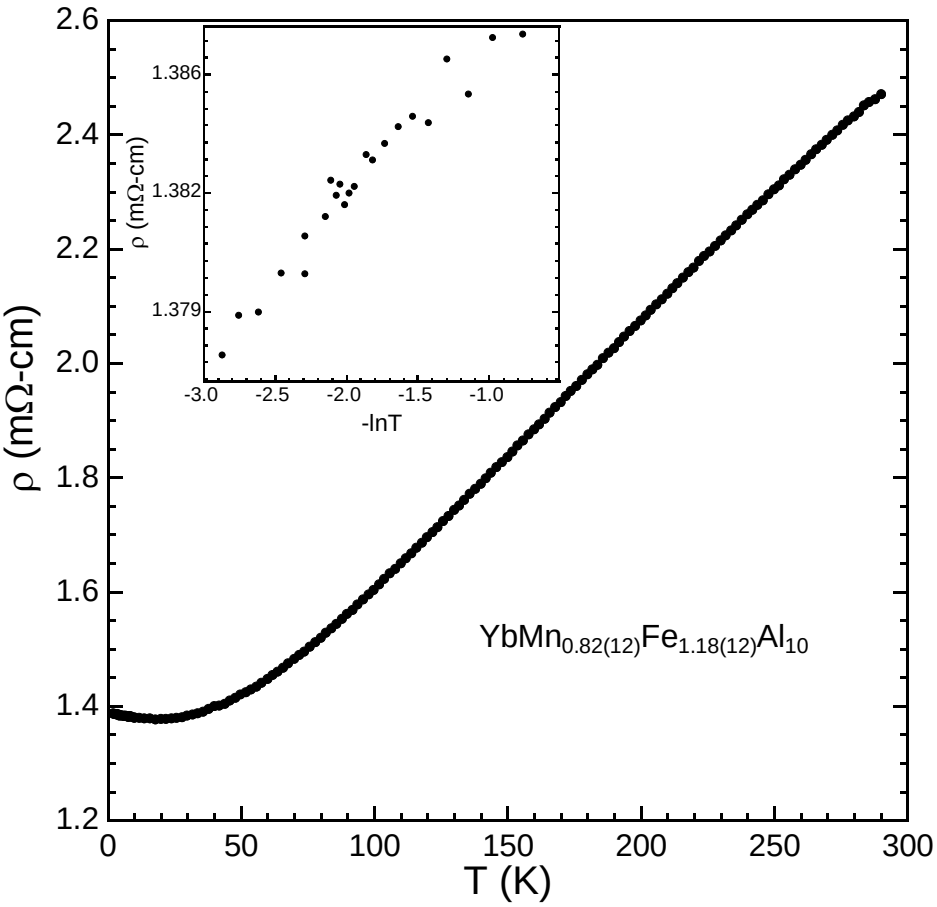

Figure 3.8. Electrical resistivity of compound **3** ($YbFe_2Al_{10}$-type). The inset shows electrical resistivity as a function of –lnT.

3.4 Summary

We have synthesized $Yb(Mn,Fe)_xAl_{12-x}$ compounds that crystallize in three structure types based on altering reaction ratios. Reaction ratios of 1:4 of Yb:M form compounds in the $ThMn_{12}$ structure, while reaction ratios of 1:3 Yb:M form compounds adopting the $CaCr_2Al_{10}$ or $YbFe_2Al_{10}$ structure types. Reaction ratios that are sufficiently rich in Mn (2.5:0.5 of Mn:Fe) form products adopting the $CaCr_2Al_{10}$ structure type, while reaction ratios of 1:1 of Mn:Fe form products in the $YbFe_2Al_{10}$ structure type. This indicates that the presence of Fe in the reaction ratio heavily influences the product towards the $YbFe_2Al_{10}$ structure type. Similar trends are

observed for the synthesis of $Yb(Mn,Ru)_xAl_{12-x}$ compounds. Reaction ratios of 2.5:0.5 of Mn:Ru are required to obtain compounds adopting the $CaCr_2Al_{10}$ structure type, while reaction ratios that are less Mn-rich (2:1, 1:1 of Mn:Ru) produce compounds that adopt the $YbFe_2Al_{10}$ structure type. Magnetic data follow modified Curie-Weiss behavior at temperatures above 50 K, with all μ_{eff} falling well below what is expected for Yb^{3+}. In the case of compound **1** ($ThMn_{12}$-type), this differs from a μ_{eff} value of 4.2(4) for $YbMn_{2.55(4)}Al_{9.45(4)}$,[24] which could be an indication of valence instability of Yb in this compound. In all cases, the possibility of Yb being in an intermediate or divalent state in these compounds cannot be discounted without further experiments. All compounds discussed exhibit metal-like resistivity to ~ 43-47 K, where values of resistivity increase as temperature decreases. These upturns in resistivity are attributed to the Kondo effect.

3.5 References

(1) Suski, W. In *Handbook on the Physics and Chemistry of Rare Earths*; Gschneidner, K. A., Eyring, L., Ed.; Elsevier: New York, 1996; Vol. 22, p 143.

(2) Buschow, K. H. J.; Van, V. J. H. N.; Van, d. H. W. W. *J. Less-Common Met.* **1976**, *50*, 145.

(3) Coldea, M.; Coldea, R.; Borodi, G. *IEEE Trans. Magn.* **1994**, *30*, 855.

(4) Coldea, M.; Neumann, M.; Lutkehoff, S.; Mahl, S.; Coldea, R. *J. Alloys Comp.* **1998**, *278*, 72.

(5) Coldea, R.; Coldea, M.; Pop, I. *IEEE Trans. Magn.* **1994**, *30*, 852.

(6) Dmitriev, V. M.; Terekhov, A. V.; Suski, W.; Ishchenko, L. A.; Cwik, J.; Palewski, T.; Kotur, B. Y.; Talik, E. *J. Alloys Comp.* **2008**, *452*, 217.

(7) Drake, B. L.; Capan, C.; Cho, J. Y.; Nambu, Y.; Kuga, K.; Xiong, Y. M.; Karki, A. B.; Nakatsuji, S.; Adams, P. W.; Young, D. P.; Chan, J. Y. *J. Phys.: Condens. Matter* **2010**, *22*, 066001/1.

(8) Duong, N. P.; Klaasse, J. C. P.; Brück, E.; de Boer, F. R.; Buschow, K. H. J. *J. Alloys Comp.* **2001**, *315*, 28.

(9) Duong, N. P.; Klaasse, J. C. P.; Brück, E.; Hagmusa, I. H.; de Boer, F. R.; Buschow, K. H. J. *J. Alloys Comp.* **2000**, *309*, L10.

(10) Felner, I., Nowik, I. *Phys. Chem. Solids* **1979**, *40*, 1035.

(11) Hagmusa, I. H.; Klaasse, J. C. P.; Bruck, E.; De, B. F. R.; Buschow, K. H. J. *J. Alloys Comp.* **2000**, *297*, 21.

(12) Florio, J. V.; Rundle, R. E.; Snow, A. I. *Acta Cryst.* **1952**, *5*, 449.

(13) Cordier, G.; Czech, E.; Ochmann, H.; Schäfer, H. *J. Less-Common Met.* **1984**, *99*, 173.

(14) Niemann, S.; Jeitschko, W. *Z. Kristallogr.* **1995**, *210*, 338.

(15) Thiede, V. M. T.; Ebel, T.; Jeitschko, W. *J. Mater. Chem.* **1998**, *8*, 125.

(16) Sefat, A. S.; Li, B.; Bud'ko, S. L.; Canfield, P. C. *Phys. Rev. B* **2007**, *76*, 174419/1.

(17) Thiede, V. M. T.; Jeitschko, W. *Z. Naturforsch. B* **1998**, *53* , 673.

(18) Strydom, A.M. *Physica B:* **2009**, *404*, 2981.

(19) Nishioka, T.; Hirai, D.; Kawamura, Y.; Kato, H.; Matsumurta, M.; Tanida, H.; Sera, M.; Matsubayashi, K.; Uwatoko, Y. *J. Phys.: Conf. Ser.* **2011**, *273*, 012046/1.

(20) Strydom, A. M.; Peratheepan, P. *Phys. Status Solidi RRL* **2010**, *4*, 356.

(21) Takesaka, T.; Oe, K.; Kobayashi, R.; Kawamura, Y.; Nishioka, T.; Kato, H.; Matsumura, M.; Kodama, K. *J. Phys.: Conf. Ser.* **2010**, *200*.

(22) Felner, I.; Nowik, I. *J. Phys. Chem. Solids* **1982**, *43*, 463.

(23) Amako, Y.; Saoka, S.; Yoshie, H.; Nagai, H.; Adachi, K. *J. Phys. Soc. Jpn.* **1995**, *64*, 1860.

(24) Fulfer, B. W.; Haldolaarachchige, N.; Young, D. P.; Chan, J. Y. *J. Solid State Chem.* **2012**, *194*, 143.

(25) Phelan, W. A.; Menard, M. C.; Kangas, M. J.; McCandless, G. T.; Drake, B. L.; Chan, J. Y. *Chem. Mater.* **2012**, *24*, 409.

(26) Felner, I.; Seh, M.; Rakavy, M.; Nowik, I. *J. Phys. Chem. Solids* **1981**, *42*, 369.

(27) Buschow, K. H. J.; Van, d. K. A. M. *J. Phys. F* **1978**, *8*, 921.

(28) Pique, C.; Abad, E.; Blanco, J. A.; Burriel, R.; Fernandez-Diaz, M. T. *Phys. Rev. B* **2005**, *71*, 174422/1.

(29) Shelyapina, M. G.; Morales, M.; Bacmann, M.; Baudelet, F.; Fruchart, D.; Giorgetti, C.; Hlil, E. K.; Krill, G.; Wolfers, P. *J. Alloys Comp.* **2004**, *368*, 84.

(30) Kerschl, P.; Rößler, U. K.; Grenèche, J. M.; Idzikowski, B.; Eckert, D.; Müller, K.-H.; Schultz, L. *J. Magn. Magn. Mater.* **2004**, *272–276, Part 1*, 627.

(31) Dmitriev, V. M.; Stępień–Damm, J.; Suski, W.; Talik, E.; Prentslau, N. N. *Phys. Status Solidi C* **2004**, *1*, 1824.

(32) Gonçalves, A. P.; Pereira, L. C. J.; Waerenborgh, J. C.; Rojas, D. P.; Almeida, M.; Havela, L.; Noël, H. *Physica B* **2006**, *373*, 8.

(33) Sério, S.; Waerenborgh, J. C.; Gonçalves, A. P.; Almeida, M.; Godinho, M. *J. Magn. Magn. Mater.* **2006**, *302*, 282.

(34) Toliński, T.; Andrzejewski, B.; Kowalczyk, A.; Chełkowska, G.; Szlaferek, A.; Frąckowiak, J. *J. Phys. Chem. Solids* **2006**, *67*, 751.

(35) Sério, S.; Pereira, L. C. J.; Cruz, M. M.; Godinho, M.; Waerenborgh, J. C. *J. Alloys Comp.* **2008**, *454*, 16.

(36) Andreev, A. V.; Tereshina, E. A.; Šantavá, E.; Šebek, J.; Koyama, K.; Watanabe, K. *J. Alloys Comp.* **2010**, *492*, 52.

(37) Altomare, A.; Burla, M. C.; Camalli, M.; Cascarano, G. L.; Giacovazzo, C.; Guagliardi, A.; Moliterni, A. G. G.; Polidori, G.; Spagna, R. *J. Appl. Crystallogr.* **1999**, *32*, 115.

(38) Sheldrick, G. *Acta Crystallogr., Sect. A: Found. Crystallogr.* **2008**, *64*, 112.

(39) Cho, J. Y.; Capan, C.; Young, D. P.; Chan, J. Y. *Inorg. Chem.* **2008**, *47*, 2472.

(40) Drake, B. L.; Grandjean, F.; Kangas, M. J.; Okudzeto, E. K.; Karki, A. B.; Sougrati, M. T.; Young, D. P.; Long, G. J.; Chan, J. Y. *Inorg. Chem.* **2010**, *49*, 445.

CHAPTER 4. FILLING IN THE HOLES: STRUCTURAL AND MAGNETIC PROPERTIES OF SINGLE CRYSTALLINE $LnMn_xGa_3$ (Ln = Ho-Tm; $x < 0.15$)

4.1 Introduction

$LnGa_3$ (Ln = Sc, Ho-Tm, Lu)[1-2] and $AnGa_3$ (An = U-Np)[3-5] compounds adopting the cubic $AuCu_3$ structure type are of particular interest because of the unusual magnetic behavior discovered in compounds of this structure type. The end member of the Ce_nMIn_{3n+2} homologous family of compounds, $CeIn_3$, is the first magnetically mediated superconductor with a T_N of 10 K at ambient pressure.[6-7] This discovery led to the investigation of $LnGa_3$ compounds and of structurally related Ln_4MGa_{12} (M = Cr, Fe, Ni, Pd, Pt, Ag)[8-13] compounds adopting the cubic Y_4PdGa_{12} structure type. Our effort to grow single crystals of compounds containing the $AuCu_3$ subunit led us to discover unusually large magnetoresistance in Er_4PtGa_{12} and Ho_4PtGa_{12} which display magnetoresistance values of 220 and 900 %, respectively.[11] More recently as part of our effort to study competing magnetic interactions in rare earth and transition metal sublattices, we grew Ln_4FeGa_{12} (Ln = Y, Tb-Er)[12] and found that the Y_4FeGa_{12} analogue is a weak itinerant ferromagnet with an ordering temperature of 36 K.

Ln_4MGa_{12} is viewed as $LnGa_3$ with M occupying the interstitial site in the body center of the $LnGa_3$ unit cell with an occupancy of 0.25. Though this representation of the Ln_4MGa_{12} structure is relatively simple, there are multiple reports of complex structural behavior for Ln_4MGa_{12} compounds. Ln_4FeGa_{12} (Ln = Y, Tb-Er) adopt the ordered Y_4PdGa_{12} structure type except for $Er_4Fe_{0.67}Ga_{12}$, which exhibits Ga site splitting and two Fe sites that are partially occupied.[12] For $Y_4Mn_{1-x}Ga_{12-y}Ge_y$ (x = 0-0.26, y = 0-4.0), Mn occupancy varies as a function of Ge concentration.[14] At a Ge concentration of y = 4.0, the Mn site is near full occupancy, with x = 0.05, and $Y_4Mn_{1-x}Ga_{12-y}Ge_y$ is paramagnetic, whereas at a decreased Ge concentration of y = 1.0, the occupancy of the Mn site also decreases, with x = 0.10, and $Y_4Mn_{1-x}Ga_{12-y}Ge_y$ exhibits

strong ferromagnetism with T_C = 223 K.[14] Ln_4CrGa_{12} (Ln = Tb-Tm)[13] were recently reported where there is evidence in single crystal X-ray diffraction data of the adoption of superstructures of the Y_4PdGa_{12} structure. A combination of band structure calculations on the hypothetical Y_4CrGa_{12} coupled with investigation of the magnetic properties of Ln_4CrGa_{12} indicate that long range magnetic order is due to Ln-Ln interactions and that Cr carries no local moment. Given the variety of structural tendencies and the assortment of magnetic behavior of the above mentioned Ln_4MGa_{12} compounds, we were interested in synthesizing novel Ln_4MnGa_{12} analogues. To investigate structural stability between $LnGa_3$ and Ln_4MGa_{12} compounds as a function of transition metal concentration, we have grown high quality single crystals of $LnMn_xGa_3$ (Ln = Ho-Tm; $x < 0.15$) and report the crystal growth parameters, structural characterization, and magnetic properties.

4.2 Experimental

4.2.1 Synthesis

Single crystals of $LnMn_xGa_3$ (Ln = Ho-Tm) were grown from their constituent elements (> 99.9 % purity and used as received). Elements (Ln:Mn:Ga) were combined in three different reaction ratios – 1:0:15, 1:0.1:20, and 1:0.2:20 (combined weight of reactants was ~ 1 g) – to study the effect of varying Mn concentration. Elements were placed in an alumina crucible, covered in quartz wool, and backfilled with ~ 1/5 atm of Ar in a fused silica tube prior to sealing the tube closed. All samples were heated to 1150 °C at a rate of 100 °C/h, held at 1150 °C for 5 h, slowly cooled to 550 °C at a rate of 5 °C/h, and finally cooled to 300 °C at a rate of 100 °C/h. When the temperature reached 300 °C, the samples were removed from the furnace, inverted with the crucible opening facing down, and centrifuged to remove excess Ga flux. Additional Ga flux was removed by repeated sonication in hot water. Synthesis yielded high quality single

crystals with cubic morphology, the largest of which were approximately 3 mm across a crystalline face.

4.2.2 Elemental Analysis

Elemental analysis of $LnMn_xGa_3$ (Ln = Ho-Tm; $x < 0.15$) single crystals was performed via energy-dispersive spectroscopy (EDS) using an EDAX detector equipped to a FEI Quanta 200 scanning electron microscope with an accelerating voltage of 15 kV. Single crystals were thoroughly polished prior to analysis in order to minimize the presence of possible surface impurities. At least 3 polished single crystals were taken per batch, and at least 7 spots from multiple points on a single crystal were analyzed for a period of no less than 30 s to ensure good crystal homogeneity. The atomic percentages were normalized to Ln. The results for compounds grown from reaction ratios of 1:0.2:20 (Ln:Mn:Ga) are $Ho_{1.00(2)}Mn_{0.12(1)}Ga_{2.80(5)}$, $Er_{1.00(6)}Mn_{0.09(3)}Ga_{2.67(10)}$, and $Tm_{1.00(8)}Mn_{0.10(3)}Ga_{2.70(16)}$, while normalized results for compounds from the 1:0.1:20 ratio are $Ho_{1.00(7)}Mn_{0.071(18)}Ga_{2.75(12)}$, $Er_{1.00(6)}Mn_{0.087(17)}Ga_{2.69(13)}$, and $Tm_{1.00(5)}Mn_{0.087(17)}Ga_{2.70(10)}$. Standard deviation in the measurements of atomic percentages is reported as uncertainty. While there is some deviation from the compositions determined from single crystal X-ray refinement, the data obtained from elemental analysis exhibit the general trend of decreasing Mn concentration with decreasing ionic radii of the lanthanide.

4.2.3 Structure Determination

Initially, structural characterization was conducted via single crystal X-ray diffraction using an Enraf Nonius KappaCCD single crystal diffractometer equipped with Mo Kα radiation (λ = 0.71073 Å). Single crystal samples were cut to appropriate sizes (exact dimensions given in Table 4.1-3), mounted on glass fibers with epoxy, and then mounted on the goniometer head. Preliminary structural models were obtained via direct methods using SIR97[15] and were refined

using SHELXL97.[16] All models were indexed to the ~ 4 Å cubic unit cell of the $AuCu_3$ structure type. Additional data with higher intensities were collected to check the samples for evidence of supercell formation, which has been reported in the literature with other Ln-M-Ga compounds.[13-14] This additional data were collected with a Bruker Kappa Apex II diffractometer equipped with a Mo Kα (λ = 0.71073) radiation source and a Triumph monochromator, which provides a marked increase in X-ray intensity. Collection of additional data, cell refinement, and data reduction were accomplished with the Bruker APEX2 software package. Diffraction data from samples grown with the reaction ratio 1:0.2:20 of Ln:Mn:Ga were indexed to ~ 4 Å unit cell of the $AuCu_3$ structure type and, in a small number of cases, to ~ 8 Å cubic unit cell indicative of the Y_4PdGa_{12} structure type. Samples grown from all other reaction ratios were only indexed to primitive ~ 4 Å cubic unit cells, indicative of the $AuCu_3$ structure type. Preliminary crystallographic models were obtained via direct methods with SIR97[15] and were refined with SHELXL97.[16] Systematic absences were consistent with compounds crystallizing in the $Pm\bar{3}m$ space group (of the $AuCu_3$ structure type) rather than the $Im\bar{3}m$ space group (of the Y_4PdGa_{12} structure type). Finally, even more data were collected with a Bruker APEXII Quazar equipped with an IμS Mo Kα source and multilayer mirror optics, which provides even higher intensities than the sealed Mo source equipped with the Triumph monochomator. Data collected with the Quazar were indexed to ~ 4 Å unit cells only. We suspect that the diffraction data used to index the 8 Å unit cells was a result of λ/2 contamination, which is present in area-detector CCD data collected using Mo radiation.[17] The results of the data collections and structural refinements are given in Tables 4.1-3. The implications of these results are discussed in detail later in this manuscript.

Table 4.1a. Crystallographic parameters for $LnGa_3$ (data collected using the Enraf Nonius diffractometer)

Crystal data		
Formula	**$ErGa_3$**	**$TmGa_3$**
Space group	$Pm\bar{3}m$	$Pm\bar{3}m$
a (Å)	4.2149(10)	4.2027(10)
V (Å^3)	74.88(3)	74.23(3)
Z	1	1
Crystal size (mm^3)	0.05 x 0.05 x 0.10	0.10 x 0.10 x 0.15
θ Range (°)	4.84-33.56	2.55-33.73
μ (mm^{-1})	54.087	56.176
Data Collection and Refinement		
Collected reflections	1440	1155
Unique reflections	71	69
R_{int}	0.056	0.074
h	$-6 \le h \le 6$	$-6 \le h \le 6$
k	$-4 \le k \le 4$	$-4 \le k \le 4$
l	$-4 \le l \le 4$	$-3 \le l \le 4$
$\Delta\rho_{max}$ (e Å^{-3})	0.798	1.375
$\Delta\rho_{min}$ (e Å^{-3})	-0.796	-1.690
GoF	1.413	1.291
Extinction coefficient	0.039(5)	0.035(11)
[a] $R_1(F)$ for $F_o^2 > 2\sigma(F_o^2)$	0.0134	0.0266
[b] $R_w(F_o^2)$	0.0360	0.0765

[a] $R_1 = \Sigma||F_o| - |F_c||/\Sigma|F_o|$
[b] $wR_2 = [\Sigma w(F_o^2 - F_c^2)^2/\Sigma w(F_o^2)^2]^{1/2}$; w = $1/[\sigma^2(F_o^2) + (0.0190\ P)^2 + 0.1417\ P]$ and w = $1/[\sigma^2(F_o^2) + (0.0547\ P)^2]$; P = $(F_o^2 + 2\ Fc^2)/3$ for $ErGa_3$ and $TmGa_3$, respectively.

Table 4.1b. Atomic positions for $LnGa_3$

Atom	Wyckoff position	Symmetry	x	y	z	Occupancy	[a] U_{eq} (Å^2)
$ErGa_3$							
Er	1*a*	*m*3*m*	0	0	0	1	0.0054(2)
Ga	3*c*	4/*mmm*	0	1/2	1/2	1	0.0097(3)
$TmGa_3$							
Tm	1*a*	*m*3*m*	0	0	0	1	0.0058(5)
Ga	3*c*	4/*mmm*	0	1/2	1/2	1	0.0099(7)

Table 4.1c. Selected interatomic distances (Å) of $LnGa_3$

Interatomic distance	**$ErGa_3$**	**$TmGa_3$**
Ln-Ga (x12)	2.9804(2)	2.9718(5)
Ln-Ln (x6)	4.2149(10)	4.2027(10)

Table 4.2a. Crystallographic parameters of $LnMn_xGa_3$ ($x \sim 0.05$, data collected with the Bruker Kappa APEXII diffractometer)

Crystal data			
Formula	**$HoMn_{0.077(11)}Ga_3$**	**$ErMn_{0.041(12)}Ga_3$**	**$TmMn_{0.049(8)}Ga_3$**
Space group	$Pm\bar{3}m$	$Pm\bar{3}m$	$Pm\bar{3}m$
a (Å)	4.2387(2)	4.2303(3)	4.2085(4)
V (Å^3)	76.155(6)	75.703(9)	75.539(12)
Z	1	1	1
Crystal size (mm^3)	0.04 x 0.04 x 0.12	0.04 x 0.04 x 0.10	0.10 x 0.10 x 0.15
θ Range (°)	4.81-30.66	4.82-30.73	4.84-30.91
μ (mm^{-1})	55.571	53.618	56.147
Data Collection and Refinement			
Collected reflections	986	1032	924
Unique reflections	42	42	42
R_{int}	0.0392	0.087	0.083
h	$-5 \le h \le 6$	$-6 \le h \le 6$	$-6 \le h \le 5$
k	$-6 \le k \le 6$	$-5 \le k \le 6$	$-5 \le k \le 6$
l	$-6 \le l \le 6$	$-4 \le l \le 4$	$0 \le l \le 6$
$\Delta\rho_{max}$ (e Å^{-3})	0.956	1.244	0.579
$\Delta\rho_{min}$ (e Å^{-3})	-0.584	-0.951	-0.596
GoF	1.384	1.186	1.140
Extinction coefficient	0.181(12)	0.001(6)	0.046(4)
[a] $R_1(F)$ for $F_o^2 > 2\sigma(F_o^2)$	0.0106	0.0202	0.0087
[b] $R_w(F_o^2)$	0.0256	0.0484	0.0152

[a] $R_1 = \Sigma||F_o| - |F_c||/\Sigma|F_o|$

[b] $wR_2 = [\Sigma w(F_o^2 - F_c^2)^2/\Sigma w(F_o^2)^2]^{1/2}$; w = $1/[\sigma^2(F_o^2) + (0.0154\ P)^2 + 0.0367\ P]$, w = $1/[\sigma^2(F_o^2) + 0.6347\ P]$, and w = $1/[\sigma^2(F_o^2) + (0.0473\ P)^2 + 0.0202\ P]$; P = $(F_o^2 + 2\ Fc^2)/3$ for $HoMn_{0.077(11)}Ga_3$, and $ErMn_{0.041(12)}Ga_3$, and $TmMn_{0.049(8)}Ga_3$ respectively.

Table 4.2b. Atomic positions of $LnMn_xGa_3$ ($x \sim 0.05$)

Atom	Wyckoff position	Symmetry	x	y	z	Occupancy	[a] U_{eq} (Å^2)
$HoMn_{0.077(11)}Ga_3$							
Ho	1*a*	*m*3*m*	0	0	0	1	0.0067(2)
Mn	1*b*	*m*3*m*	1/2	1/2	1/2	0.077(11)	0.012(7)
Ga	3*c*	4/*mmm*	0	1/2	1/2	1	0.0154(3)
$ErMn_{0.041(12)}Ga_3$							
Er	1*a*	*m*3*m*	0	0	0	1	0.076(5)
Mn	1*b*	*m*3*m*	1/2	1/2	1/2	0.041(12)	0.076(5)
Ga	3*c*	4/*mmm*	0	1/2	1/2	1	0.0150(5)
$TmMn_{0.049(8)}Ga_3$							
Tm	1*a*	*m*3*m*	0	0	0	1	0.00578(15)
Mn	1*b*	*m*3*m*	1/2	1/2	1/2	0.049(8)	0.010(8)
Ga	3*c*	4/*mmm*	0	1/2	1/2	1	0.01276(19)

Table 4.2c. Selected interatomic distances (Å) for $LnMn_xGa_3$ ($x \sim 0.05$)

Interatomic distance	**$HoMn_{0.077(11)}Ga_3$**	**$ErMn_{0.041(12)}Ga_3$**	**$TmMn_{0.049(8)}Ga_3$**
Ln-Ga (x12)	2.9934(3)	2.9913(2)	2.9759(2)
Ln-Mn (x8)	3.6661(3)	3.6635(2)	3.6447(2)
Ln-Ln (x6)	4.2333(6)	4.2303(3)	4.2085(4)
Mn-Ga (x6)	2.1166(3)	2.1153(2)	2.1042(2)

Table 4.3a. Crystallographic parameters for $LnMn_xGa_3$ (x = 0.10-0.15, data collected with the Bruker Kappa APEXII diffractometer)

Crystal data			
Formula	**$HoMn_{0.158(9)}Ga_{3.07(12)}$**	**$ErMn_{0.128(4)}Ga_{2.92(8)}$**	**$TmMn_{0.104(5)}Ga_{2.9(1)}$**
Space group	$Pm\bar{3}m$	$Pm\bar{3}m$	Pm-3m
a (Å)	4.2351(2)	4.2351(2)	4.2195(2)
V (Å^3)	75.961	75.961(6)	75.125(6)
Z	1	1	1
Crystal size (mm^3)	0.01 x 0.06 x 0.06	0.01 x 0.05 x 0.06	0.01 x 0.06 x 0.08
θ Range (°)	4.79-31.01	4.81-30.69	4.83-36.97
μ (mm^{-1})	55.067	53.754	59.528
Data Collection and Refinement			
Collected reflections	2870	1416	1512
Unique reflections	44	42	61
R_{int}	0.0554	0.0406	0.0434
h	$-5 \le h \le 6$	$-5 \le h \le 6$	$-7 \le h \le 6$
k	$-6 \le k \le 5$	$-6 \le k \le 5$	$-6 \le k \le 6$
l	$-6 \le l \le 6$	$-6 \le l \le 6$	$-5 \le l \le 6$
$\Delta\rho_{max}$ (e Å^{-3})	0.436	0.298	0.844
$\Delta\rho_{min}$ (e Å^{-3})	-0.882	-0.344	-0.695
GoF	1.216	1.413	1.118
Extinction coefficient	0.25(3)	0.088(6)	0.065(6)
[a] $R_1(F)$ for $F_o^2 > 2\sigma(F_o^2)$	0.0089	0.0051	0.0090
[b] $R_w(F_o^2)$	0.0197	0.0096	0.0143

[a] $R_1 = \Sigma||F_o| - |F_c||/\Sigma|F_o|$

[b] $wR_2 = [\Sigma w(F_o^2 - F_c^2)^2/\Sigma w(F_o^2)^2]^{1/2}$; w = $1/[\sigma^2(F_o^2) + (0.0155\ P)^2]$ for $HoMn_{0.158(9)}Ga_{3.07(12)}$, w = $1/[\sigma^2(F_o^2) + (0.0045\ P)^2]$ for $ErMn_{0.128(4)}Ga_{2.92(8)}$, and w = $1/[\sigma^2(F_o^2) + (0.0071\ P)^2]$ for $TmMn_{0.104(5)}Ga_{2.9(1)}$; P = $(F_o^2 + 2\ Fc^2)/3$.

4.2.4 Magnetic Property Measurement

Magnetic properties for $LnMn_xGa_3$ (Ln = Ho-Tm; $x < 0.15$) compounds were measured with a Quantum Design Magnetic Property Measurement System (MPMS). All samples used for magnetic measurements possess cubic morphology and were polished on all crystal faces prior to measurements. The samples were also oriented using a single crystal X-ray diffractometer.

Table 4.3b. Atomic positions of $LnMn_xGa_3$ (x = 0.10-0.15)

Atom	Wyckoff position	Symmetry	x	y	z	Occupancy	$^aU_{eq}$ (Å^2)
$HoMn_{0.158(9)}Ga_{3.07(12)}$							
Ho	1*a*	*m*3*m*	0	0	0	1	0.0058(5)
Mn	1*b*	*m*3*m*	1/2	1/2	1/2	0.158(9)	0.009(2)
Ga	3*c*	4/*mmm*	0	1/2	1/2	0.68(2)	0.0104(11)
Ga'	6*f*	4*mm*	0.082(2)	1/2	1/2	0.171(10)	0.0082(13)
$ErMn_{0.128(4)}Ga_{2.92(8)}$							
Er	1*a*	*m*3*m*	0	0	0	1	0.00797(19)
Mn	1*b*	*m*3*m*	1/2	1/2	1/2	0.128(4)	0.0100(17)
Ga	3*c*	4/*mmm*	0	1/2	1/2	0.684(13)	0.0084(5)
Ga'	6*f*	4*mm*	0.0810(15)	1/2	1/2	0.145(6)	0.0067(10)
$TmMn_{0.104(5)}Ga_{2.9(1)}$							
Tm	1*a*	*m*3*m*	0	0	0	1	0.00712(16)
Mn	1*b*	*m*3*m*	1/2	1/2	1/2	0.104(5)	0.011(2)
Ga	3*c*	4/*mmm*	0	1/2	1/2	0.678(16)	0.0067(5)
Ga'	6*f*	4*mm*	0.0761(19)	1/2	1/2	0.141(8)	0.0079(1)

Table 4.3c. Selected interatomic distances (Å) for $LnMn_xGa_3$ (x = 0.10-0.15)

Interatomic distance	**$HoMn_{0.158(9)}Ga_{3.07(12)}$**	**$ErMn_{0.128(4)}Ga_{2.92(8)}$**	**$TmMn_{0.104(5)}Ga_{2.9(1)}$**
Ln-Ga (x12)	3.0063(2)	2.9947(2)	2.9836(2)
Ln-Ga' (x12)	3.0265(4)	3.0143(2)	3.0009(2)
Ln-Mn (x8)	3.6820(2)	3.6677(2)	3.6542(2)
Ln-Ln (x6)	4.2516(2)	4.2351(2)	4.2195(2)
Mn-Ga' (x6)	2.4744(4)	2.4606(2)	2.4309(2)

Magnetization as a function of temperature was measured in zero field cooled conditions from 1.8 – 30 K under an applied field of 100 Oe and from 1.8 – 390 K under an applied field of 1000 Oe. Field-dependent magnetization measurements were conducted at 2 K from 0 – 7 T.

4.3 Results and Discussion

4.3.1 Structure

Results from single crystal X-ray diffraction indicate that $LnMn_xGa_3$ (Ln = Ho-Tm) form with a range of Mn concentrations. Reaction ratios of Ln:Ga (1:15) and Ln:Mn:Ga (1:0.1:20 and 1:0.2:20) produced single crystals adopting the $AuCu_3$ structure type. The $AuCu_3$ structure type consists of a primitive cubic lattice with ~ 4 Å dimension with Ln atoms occupying the corners and Ga atoms occupying the face centers. There is a void space in the

body center of the unit cell in $LnGa_3$ compounds that a transition metal can occupy. Such is the case with products grown from reaction ratios containing Mn. Refinements of the occupancies of these compounds converge to ~ 0.05 on the 1*b* site for samples grown with a ratio of 1:0.1:20 (see Table 4.2b for exact occupancies) and to ~ 0.10-0.15 on the 1*b* site (1/2, 1/2, 1/2) for samples grown with a ratio of 1:0.2:20 (see Table 4.3b for exact occupancies). Increasing the amount of Mn to 1:0.4:20 or 1:1:20 of Ln:Mn does not lead to an increased Mn concentration, which seems to reach a maximum value of $x \sim 0.15$ for $LnMn_xGa_3$. Introducing Mn to $LnGa_3$ is consistent with the larger unit cell parameters and is reflected in the Ln-Ln and Ln-Ga (Ln = Ho-Tm) distances. To effectively model the Mn-stuffed $LnGa_3$ compounds, two separate Ga positions were refined when $x \sim 0.10$-0.15 (see Table 4.3). The first Ga site (0, 1/2, 1/2) is occupied when Mn is not present while the second Ga site, or "Ga´" at (x, 1/2, 1/2), is occupied when Mn is present, resulting in Mn-Ga´ distances ~ 2.4 Å (see Table 4.3c for exact distances). These Mn-Ga´ distances are very similar to M-Ga distances reported for Ln_4MGa_{12} (Ln = Tb-Er; M = Cr, Fe) compounds (see Figure 4.1), as are Ln-Ln distances (see Figure 4.2).[12-13] Unfortunately, application of the modeling techniques used above to describe $LnMn_{0.15}Ga_3$ were not suitable in describing $LnMn_{0.05}Ga_3$. In $LnMn_{0.05}Ga_3$, modeling two separate Ga sites led to higher R_1 values than did modeling a single Ga site with elongated anisotropic atomic displacement parameters (ADPs). Of course, modeling a single Ga site with ADPs that are elongated in the direction of Mn has similar physical meaning to modeling Ga and Ga´ sites; when Mn is present, Ga is forced away to a reasonable distance of approximately 2.4 Å (Ga´). It is interesting to note that Mn-containing Ho reaction ratios stabilize the cubic $AuCu_3$-type analogue of $HoMn_xGa_3$, whereas β-$HoGa_3$,[2] which crystallizes with a hexagonal unit cell, is stabilized from non-Mn-containing Ho reaction ratios. No Ho:Ga reaction of 1:15 was attempted

due to the fact that such a reaction produces β-$HoGa_3$ instead of $HoGa_3$ in the $AuCu_3$ structure type.

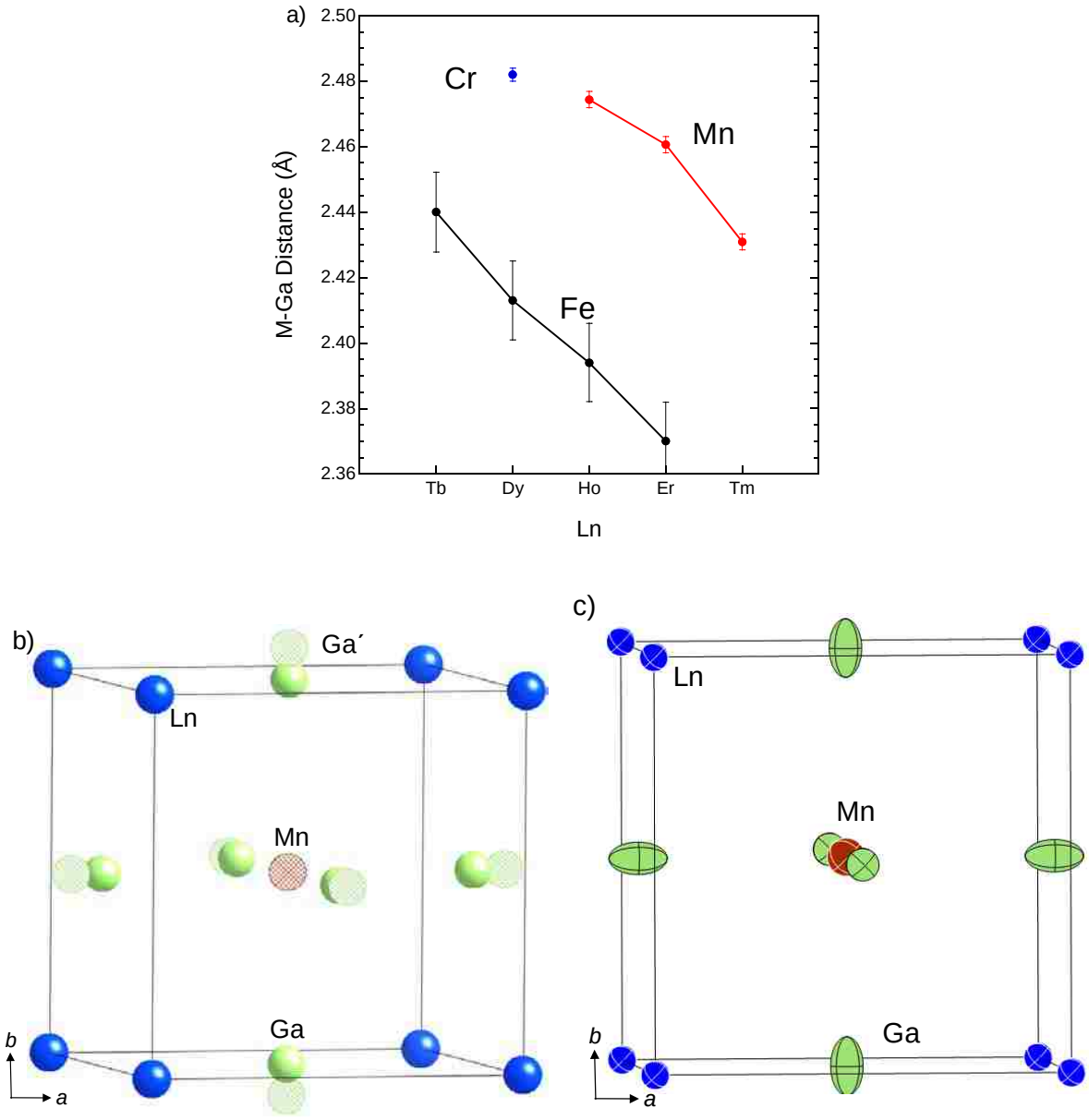

Figure 4.1. a) M-Ga distances for Ln-M-Ga compounds. Note: Cr and Fe distances were obtained from B.R. Slater *et al.*[13] and B.L. Drake *et al.*,[12] respectively. b) $LnMn_{0.15}Ga_3$ (Ln = Ho-Tm) unit cell, where Ln atoms are blue spheres, Mn are red hatched circles, Ga (3*c*) are green spheres, and Ga´ (6*f*) are green hatched circles. c) $LnMn_{0.05}Ga_3$ unit cell, where Ln atoms are blue, Mn are red, and Ga are green.

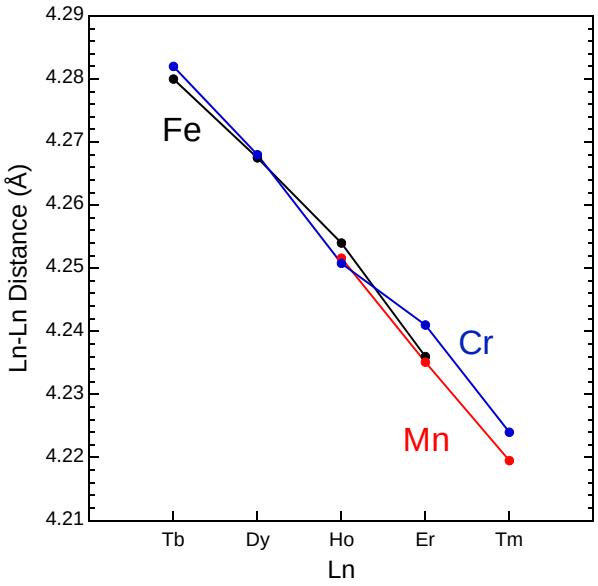

Figure 4.2. Ln-Ln distances for Ln_4MGa_{12} (M = Cr, Fe) and $LnMn_{0.15}Ga_3$ compounds (shown in red). Note: Cr distances (shown in blue) are derived from unit cell lengths reported by B.R. Slater *et al.*,[13] and Fe distances (shown in black) are reported by B.L. Drake *et al.*[12]

The crystallographic model outlined above describes compounds that do not adopt the ordered Y_4PdGa_{12} structure type due to insufficient Mn incorporation. In a recent report regarding Ln_4CrGa_{12} (Ln = Tb-Tm) compounds, the authors conjectured that $LnGa_3$ and Ln_4CrGa_{12} can form intergrowths with each other.[13] Essentially, $LnMn_xGa_3$ are described as intergrowths between $LnGa_3$ and a hypothetical "Ln_4MnGa_{12}". Given the similarities between these compounds and previously reported Ln_4CrGa_{12}, it is possible that these same modeling techniques could be successfully applied to Ln_4CrGa_{12} as well, which would lend credence to the hypothesis of Slater *et al.*[13] that $LnGa_3$ and Ln_4CrGa_{12} are indeed forming intergrowths.

To further explore the structural preferences of compounds adopting the $AuCu_3$ and Y_4PdGa_{12} structure types, we attempted to synthesize $ScFe_xGa_3$. $Er_4Fe_{0.67}Ga_{12}$, adopting the Y_4PdGa_{12} structure type, is the end member of the series of Ln_4FeGa_{12} (Ln = Y, Tb-Er) compounds.[12] We substituted Sc for Er in a reaction ratio of 1:1:20 (Sc:Fe:Ga), and we

hypothesized that such a reaction would yield a product adopting the stuffed $AuCu_3$ structure type instead of the Y_4PdGa_{12} structure type, by virtue of Sc having a smaller atomic radius (162 pm) than Er (176 pm). Instead, the reaction produced single crystals of $ScFeGa_5$ adopting the $HoCoGa_5$ structure type,[18] which is structurally related to the $AuCu_3$ and Y_4PdGa_{12} structure types as shown in Figure 4.3. $ScFeGa_5$ is a new compounds adopting the $HoCoGa_5$ structure type and additional experimental details regarding the synthesis and physical properties of $ScFeGa_5$ will be reported elsewhere.

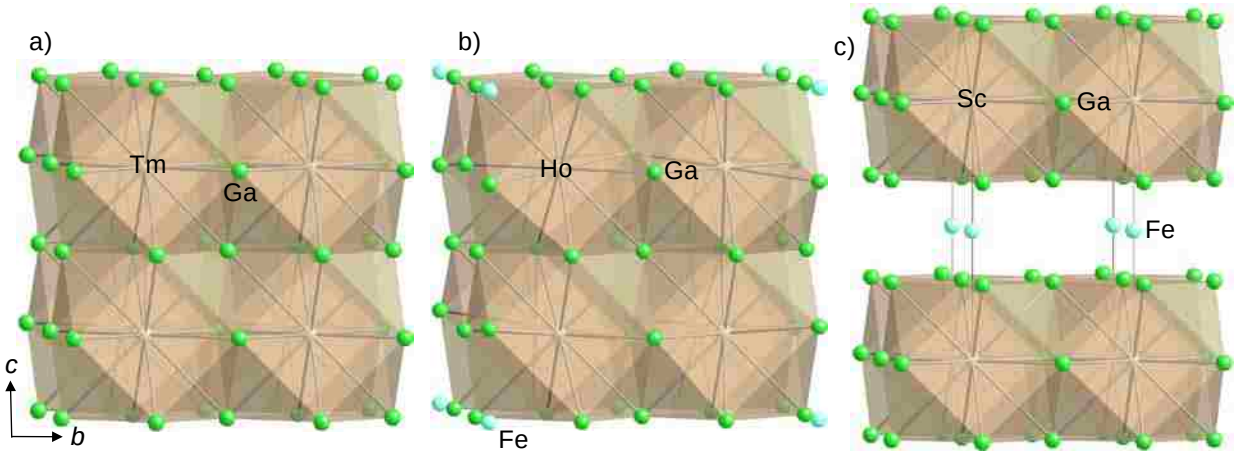

Figure 4.3. a)$TmGa_3$, b)Ho_4FeGa_{12}, and c)$ScFeGa_5$ of the $AuCu_3$, Y_4PdGa_{12}, and $HoCoGa_5$ structure types, respectively, are shown for comparison. Each crystal structure is depicted with cuboctahedra consisting of Ga atoms (green spheres) drawn around the Tm, Ho, and Sc atoms (tan spheres). The Fe atoms (light blue spheres) occupy the octahedral holes in the Y_4PdGa_{12} structure type and form a layer in the *ab*-plane in the $HoCoGa_5$ structure type.

4.3.2 Magnetic Properties

4.3.2.1 $HoMn_xGa_3$ ($x < 0.15$)

Temperature-dependent magnetic susceptibilities of single crystalline $HoMn_xGa_3$ are shown in Figure 4.4. The magnetic susceptibility data were fit from 50-390 K with the modified Curie-Weiss equation $\chi(T) = \chi_o + C/(T - \theta)$, where C is the Curie constant, θ is the Weiss temperature, and χ_o is the temperature independent contribution to the susceptibility. The

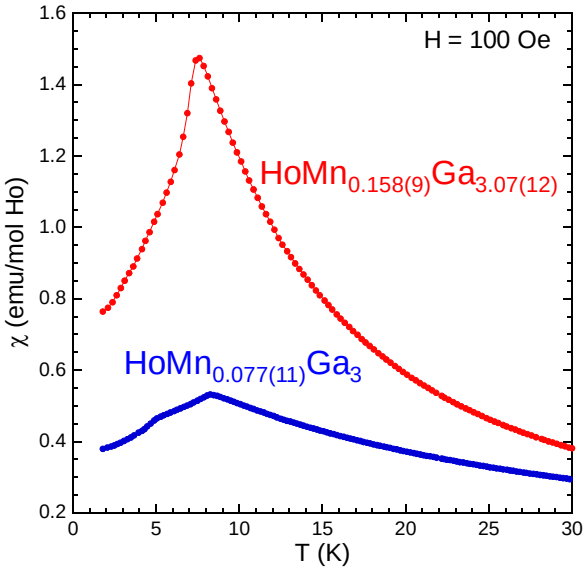

Figure 4.4. Temperature-dependent magnetic susceptibility for $HoMn_xGa_3$ at an applied field of 100 Oe.

Table 4.4. Magnetic parameters for single crystalline $HoMn_xGa_3$

Compound	Fit range (K)	χ_o (x 10^{-4})	θ_W (K)	T_N (K)	μ_{eff} (μ_B/Ho)
$HoMn_{0.077(11)}Ga_3$	50-390	-8.1(4)	-17.26(5)	8.4	10.616(4)
$HoMn_{0.158(9)}Ga_{3.07(12)}$	50-390	19.9(9)	-7.56(12)	7.7	10.15(1)

Ho^{3+} μ_{calc} = 10.61 μ_B

magnetic parameters derived from this fit are summarized in Table 4.4. The effective magnetic moments are μ_{eff} = 10.616(4) μ_B/Ho for $HoMn_{0.077(11)}Ga_3$ and μ_{eff} = 10.15(1) μ_B/Ho for $HoMn_{0.158(9)}Ga_{3.07(12)}$, compared to effective moments reported for Ho_4CrGa_{12} (10.75 μ_B/Ho) and Ho_4FeGa_{12} (10.87 μ_B/Ho). The effective moment of $HoMn_{0.077(11)}Ga_3$ is very close to that of the Ho^{3+} free ion (μ_{calc} = 10.61 μ_B), while the effective moment of $HoMn_{0.158(9)}Ga_{3.07(12)}$ is approximately 0.5 μ_B/Ho less than that of the Ho^{3+} free ion. This reduction of the effective moment with increasing Mn concentration is puzzling when paired with the fact that magnetization values increase as Mn concentration increases. Values of θ_W similarly decrease as Mn increases. One explanation for this decrease of effective moment and θ_W with increasing Mn could be that the addition of Mn decreases the interaction strength between Ho atoms by

increasing the Ho-Ho interatomic distance. Also, cubic $LnGa_3$ (Ln = Er, Tm) adopting the $AuCu_3$ structure type are known to exhibit unique magnetic properties resulting from crystal electric field effects.[19-24] Specifically, $ErGa_3$ and $TmGa_3$ have attracted significant attention because they exhibit strong crystalline electric field (CEF) effects and quadrupolar ordering.[20-28] For $TmGa_3$, two first order transitions occur in a very narrow temperature range: a tetragonal distortion driven by quadrupolar ordering at T_Q = 4.29 K followed by an antiferromagnetic transition at T_N = 4.26 K. At temperatures below 4 K, CEF splitting of the Tm^{3+} states results in a nonmagnetic ground state. Certainly the presence of Mn in the body center of the unit cell in $LnMn_xGa_3$ compounds would affect the CEF of the lanthanide, though the specific consequences of such affectation cannot be resolved without further experimentation. The reduction in the effective moments of the $HoMn_xGa_3$ with increasing Mn concentration could simply be an artifact resulting from CEF effects, which the Curie-Weiss equation does not account for. Maxima are present in the susceptibilities at T_N = 8.4 K for $HoMn_{0.077(11)}Ga_3$ and T_N = 7.7 K for $HoMn_{0.159(9)}Ga_3$, indicating the onset of long range antiferromagnetic order. These ordering temperatures compare well with the antiferromagnetic ordering temperatures of Ho_4CrGa_{12} (T_N = 7.5 K) and Ho_4FeGa_{12} (T_N = 9 K). When comparing these $HoMn_xGa_3$ analogues with β-$HoGa_3$, it is apparent that the ordering temperature is higher for the Mn-containing analogues (β-$HoGa_3$ T_N = 6.15 K).[29] This could be a result of an increased concentration of conduction electrons that are provided by Mn, which would positively affect RKKY interactions and increase the ordering temperature in Mn-containing samples.

Field-dependent magnetization data at 2 K are shown for $HoMn_xGa_3$ samples in Figure 4.5. The magnetization of $HoMn_{0.077}Ga_3$ increases smoothly with applied field up to ~ 7 T and does not exhibit any saturation behavior. The magnetization of $HoMn_{0.158}Ga_3$ likewise increases

with applied field up to ~ 5.5 T, at which point the magnetization values begin to saturate. This behavior is similar to isothermal field-dependent magnetization data of Ho_4MGa_{12} (M = Cr, Pd, Pt)[11,13] analogues. At this point it is useful to compare the data presented here with field-dependent magnetization data of β-$HoGa_3$.[29] β-$HoGa_3$ exhibits multiple metamagnetic transitions at T = 1.37 K when a magnetic field is applied along the *c*-axis. This is caused by interplanar and intraplanar antiferromagnetic couplings between Ho atoms in the hexagonal β-$HoGa_3$ structure. The addition of Mn stabilizes the cubic variant of $HoGa_3$, which leads to a breakdown of metamagnetic behavior in field-dependent magnetization. The artifacts of metamagnetism can be seen in the non-linearity of the data for $HoMn_{0.077}Ga_3$, and these artifacts are absent for the magnetization of $HoMn_{0.158}Ga_3$ which displays linear field dependence to ~ 5.5 T.

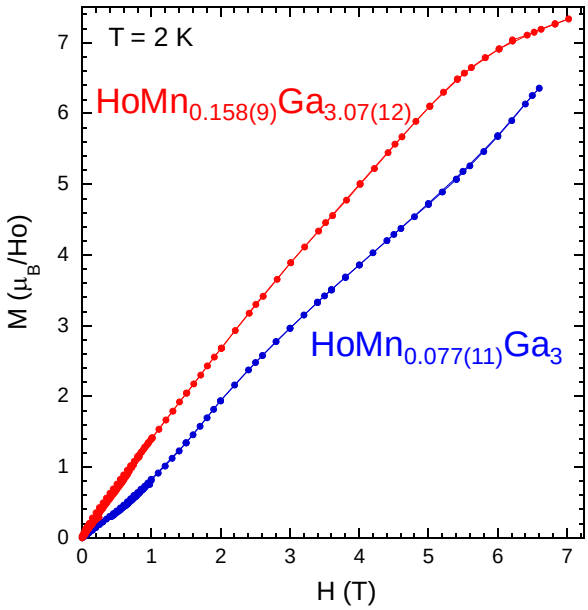

Figure 4.5. Field-dependent magnetization for $HoMn_xGa_3$ collected at 2 K.

4.3.2.2 $ErMn_xGa_3$ (x < 0.15)

Temperature-dependent magnetic susceptibilities of single crystalline $ErMn_xGa_3$ are shown in Figure 4.6 and the magnetic parameters derived from the fit of the modified Curie-

Weiss equation are given in Table 4.5. $ErGa_3$, $ErMn_{0.041(12)}Ga_3$, and $ErMn_{0.128(4)}Ga_{2.92(8)}$ order antiferromagnetically at 2.9 K, 3.3 K, and 3.1 K, respectively. The effective magnetic moments are μ_{eff} = 10.095(4) μ_B/Er for $ErGa_3$, μ_{eff} = 9.522(4) μ_B/Er for $ErMn_{0.041(12)}Ga_3$, and μ_{eff} = 9.494(7) μ_B/Er for $ErMn_{0.128(4)}Ga_{2.92(8)}$, compared to the effect moments reported for Er_4CrGa_{12} (9.76 μ_B/Er) and $Er_4Fe_{0.67}Ga_{12}$ (9.55 μ_B/Er). Similar to the Ho analogues, the effective magnetic moments of $ErMn_xGa_3$ decrease with increasing Mn concentration, while magnetization values are largest for the compound with the highest Mn concentration. The effective moment of

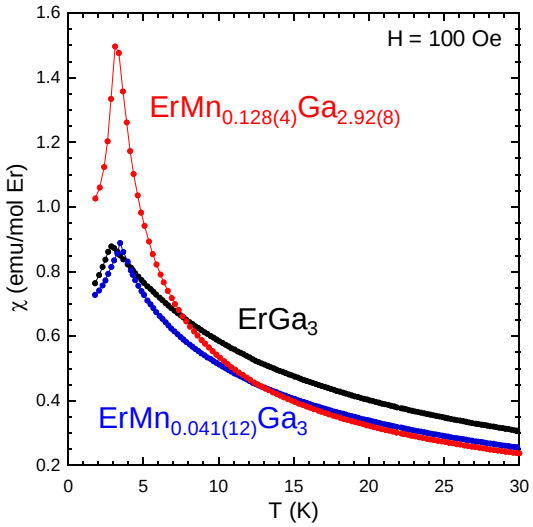

Figure 4.6. Temperature-dependent magnetic susceptibility for $ErMn_xGa_3$ at an applied field of 100 Oe.

Table 4.5. Magnetic parameters for single crystalline $ErMn_xGa_3$

Compound	Fit range (K)	χ_o (x 10^{-4})	θ_W (K)	T_N (K)	μ_{eff} (μ_B/Er)
$ErGa_3$	50-390	0.3(4)	-10.95(5)	2.9	10.095(4)
$ErMn_{0.041(12)}Ga_3$	50-390	-2.2(3)	-9.59(5)	3.3	9.522(4)
$ErMn_{0.128(4)}Ga_{2.92(8)}$	50-390	8.3(6)	-8.59(9)	3.1	9.494(7)

Er^{3+} μ_{calc} = 9.58 μ_B

$ErMn_{0.041(12)}Ga_3$ is the closest to the calculated moment of the Er^{3+} free ion (9.58 μ_B), while the effective moment of $ErGa_3$ is significantly larger and the effective moment of $ErMn_{0.128(4)}Ga_{2.92(8)}$ is significantly smaller. As in the case of $HoMnxGa_3$, this could be from increased Er-Er distances in Mn-containing analogues or crystal electric field effects. The same

trend that was seen for the Ho analogues of increased ordering temperatures for Mn-containing compounds over non-Mn-containing compounds is also seen for the Er analogues, though the magnitudes of the increases are much less pronounced. As with the Ho analogues, the increase in T_N could be due to the additional conduction electrons introduced by Mn. Field-dependent magnetization curves collected at 2K are shown for $ErMn_xGa_3$ in Figure 4.7. No hysteresis or saturation is observed up to an applied field of 7 T.

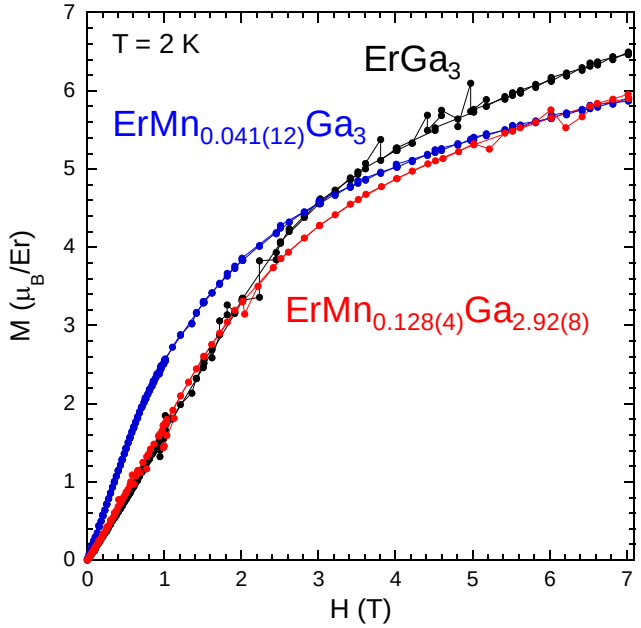

Figure 4.7. Field-dependent magnetization for $ErMn_xGa_3$ collected at 2 K.

4.3.2.3 $TmMn_xGa_3$ ($x < 0.15$)

Temperature-dependent magnetic susceptibilities of single crystalline $TmMn_xGa_3$ are shown in Figure 4.8 and the magnetic parameters derived from the fit of the modified Curie-Weiss equation are given in Table 4.6. The effective moments are μ_{eff} = 7.563(4) μ_B/Tm for $TmGa_3$, μ_{eff} = 7.464(1) μ_B/Tm for $TmMn_{0.049(8)}Ga_3$, and 7.407(3) μ_B/Tm for $TmMn_{0.104(4)}Ga_{2.9(1)}$. As with $HoMn_xGa_3$ and $ErMn_xGa_3$ compounds, the effective magnetic moments of $TmMn_xGa_3$ compounds decrease with increasing Mn concentration, with $TmGa_3$ having the closest effective moment to the calculated moment of the Tm^{3+} free ion (7.56 μ_B).

This decrease in effective moment could be a result of increased Tm-Tm distances as a result of Mn incorporation or CEF effects. It is interesting to note that unlike the Ho and Er analogues, magnetization values for

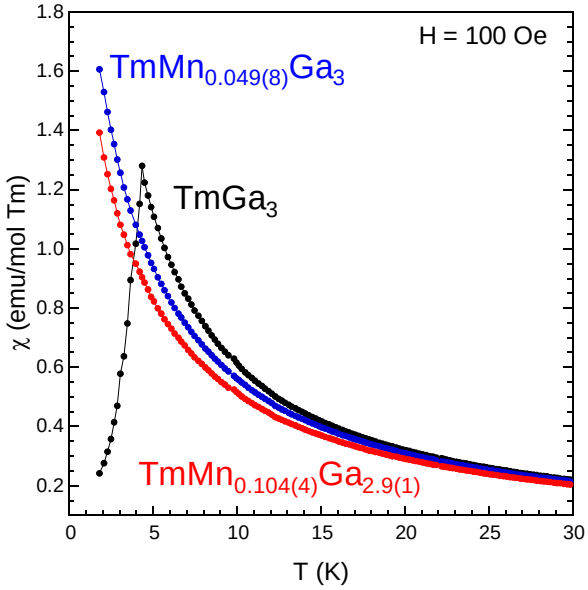

Figure 4.8. Temperature-dependent magnetic susceptibility for $TmMn_xGa_3$ at an applied field of 100 Oe.

Table 4.6. Magnetic parameters for single crystalline $TmMn_xGa_3$

Compound	Fit range (K)	χ_o (x 10^{-4})	θ_W (K)	T_N (K)	μ_{eff} (μ_B/Tm)
$TmGa_3$	50-390	-3.30(9)	-2.70(2)	4.2	7.563(2)
$TmMn_{0.049(8)}Ga_3$	50-390	-2.72(8)	-2.641(16)	-	7.464(1)
$TmMn_{0.104(4)}Ga_{2.9(1)}$	50-390	-3.0(2)	-2.67(4)	-	7.407(3)

Tm^{3+} μ_{calc} = 7.56 μ_B

$TmMn_xGa_3$ decrease as Mn concentration increases. It is also interesting to note that $TmGa_3$ exhibits antiferromagnetic ordering at ~ 4.2 K, while $TmMn_{0.049(8)}Ga_3$ and $TmMn_{0.104(4)}Ga_{2.9(1)}$ are paramagnetic down to 1.8 K, which indicates that the addition of Mn to $TmGa_3$ disrupts long range magnetic order. This behavior varies from that of the Ho and Er analogues previously discussed where the addition of Mn results in an increase of T_N. Expected behavior for a series of Ln-containing compounds is that ordering temperatures scale with the de Gennes factor,

which is not the case for $LnGa_3$ (Ln = Ho-Tm). Rather, $TmGa_3$ orders at a higher temperature than $ErGa_3$. Previous studies of $TmGa_3$ have ascribed the unusual magnetic order it exhibits to the mixing of CEF levels as a result of quadrupolar ordering (T_Q = 2.49 K).[19-21,23,25] This suggests that the addition of Mn disrupts the CEF effects that cause $TmGa_3$ to order by distorting the local environment of Tm.

Field-dependent magnetization data collected at 2 K are shown for $TmMn_xGa_3$ in Figure 4.9. The magnetization of $TmGa_3$ exhibits a large and sudden increase from a value of about 0.3 μ_B/Tm to about 4 μ_B/Tm at an applied field of ~ 0.8 T. This increase is followed by a smooth linear increase all the way through 7 T. This is attributed to a structural transition driven by quadrupolar pair interactions.[19-21,25,28] This feature is distinctly absent from the field-dependent magnetization curves of Mn-containing $TmMn_{0.049(8)}Ga_3$ and $TmMn_{0.104(5)}Ga_{2.9(1)}$, both of which show no hysteresis or saturation up to an applied field of 7 T. This is consistent with the disruption of local environment of Tm that is caused by the addition of Mn.

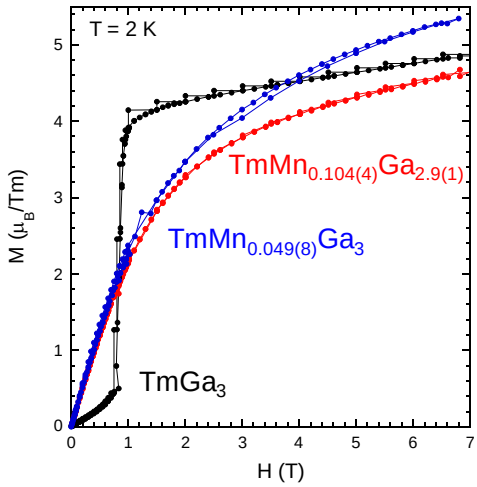

Figure 4.9. Field-dependent magnetization for $TmMn_xGa_3$ collected at 2 K.

4.4 Summary

We have grown single crystals of $LnMn_xGa_3$ (Ln = Ho-Tm; $x < 0.15$). These compounds adopt a "stuffed" variant of the $AuCu_3$ structure type when Mn is present, where Mn fractionally

occupies the body center position of the unit cell causing the Ga atoms to have either slight disorder (causing elongated Ga ADPs) or position disorder (using two separate Ga positions). Subtle changes are identified in the magnetic parameters of $LnMn_xGa_3$ (Ln = Ho-Tm; $x < 0.15$) as the concentration of Mn changes. A decrease in the effective magnetic moments of these compounds occurs with increasing Mn concentration. The decrease in effective magnetic moment is accompanied by an increase in magnetic susceptibility with increasing Mn concentration for Ho and Er analogues. This is attributed either to increases in the Ln-Ln interatomic distances as a function of Mn incorporation or to changing the CEF of Ln by adding Mn, though additional experiments such as inelastic neutron scattering would be required to elucidate crystal electric fields in these compounds. Mn-containing Ho and Er analogues order antiferromagnetically at slightly higher temperatures ($T_N > 7.7$ K and 3.1 K for $HoMn_xGa_3$ and $ErMn_xGa_3$, respectively) than do the non-Mn-containing analogues ($T_N = 6.2$ K and 2.9 K for β-$HoGa_3$ and $ErGa_3$, respectively), indicating that the addition of Mn to these systems slightly increases the strength of the magnetic interactions between the Ln atoms. $TmGa_3$ exhibits antiferromagnetic order around 4.2 K due to CEF effects, whereas $TmMn_xGa_3$ compounds are paramagnetic down to 1.8 K. This is attributed to a distortion of the Tm local environment upon the addition of Mn, which necessarily alters the crystal electric field of Tm. Due to the range of Mn concentrations possible for $LnMn_xGa_3$ (Ln = Ho-Tm; $x < 0.15$) and the fact that CEF effects lead to interesting magnetic features in $LnMn_xGa_3$, these compounds present a good opportunity to study how crystal electric fields are affected by varying Mn concentrations.

4.5 References

(1) Yatsenko, S. P.; Semyannikov, A. A.; Semenov, B. G.; Chuntonov, K. A. *J. Less-Common Met.* **1979**, *64*, 185.

(2) Cirafici, S.; Franceschi, E. *J. Less-Common Met.* **1981**, *77*, 269.

(3) Buschow, K. H. J. *J. Less-Common Met.* **1973**, *31*, 165.

(4) Russell, A. M.; Roof, R. B.; Elliott, R. O.; Giessen, B. C. *J. Appl. Crystallogr.* **1976**, *9*, 244.

(5) Bouillet, M. N.; Charvolin, T.; Blaise, A.; Burlet, P.; Fournier, J. M.; Larroque, J.; Sanchez, J. P. *J. Magn. Magn. Mater.* **1993**, *125*, 113.

(6) Mathur, N. D.; Grosche, F. M.; Julian, S. R.; Walker, I. R.; Freye, D. M.; Haselwimmer, R. K. W.; Lonzarich, G. G. *Nature* **1998**, *394*, 39.

(7) Thompson, J. D.; Movshovich, R.; Fisk, Z.; Bouquet, F.; Curro, N. J.; Fisher, R. A.; Hammel, P. C.; Hegger, H.; Hundley, M. F.; Jaime, M.; Pagliuso, P. G.; Petrovic, C.; Phillips, N. E.; Sarrao, J. L. *J. Magn. Magn. Mater.* **2001**, *226-230*, 5.

(8) Vasilenko, L. O.; Noga, A. S.; Grin, Y. N.; Koterlin, M. D.; Yarmolyuk, Y. P. *Russ. Metall.* **1988**, 216.

(9) Gumeniuk, R. V.; Stel'makhovych, B. M.; Kuz'ma, Y. B. *J. Alloys Comp.* **2003**, *352*, 128.

(10) Williams, W. M.; Moldovan, M.; Young, D. P.; Chan, J. Y. *J. Solid State Chem.* **2005**, *178*, 52.

(11) Cho, J. Y.; Moldovan, M.; Young, D. P.; Chan, J. Y. *J. Phys.: Condens. Matter* **2007**, *19*, 266224.

(12) Drake, B. L.; Grandjean, F.; Kangas, M. J.; Okudzeto, E. K.; Karki, A. B.; Sougrati, M. T.; Young, D. P.; Long, G. J.; Chan, J. Y. *Inorg. Chem.* **2010**, *49*, 445.

(13) Slater, B. R.; Bie, H.; Stoyko, S. S.; Bauer, E. D.; Thompson, J. D.; Mar, A. *J. Solid State Chem.* **2012**, *196*, 409.

(14) Francisco, M. C.; Malliakas, C. D.; Piccoli, P. M. B.; Gutmann, M. J.; Schultz, A. J.; Kanatzidis, M. G. *J. Am. Chem. Soc.* **2010**, *132*, 8998.

(15) Altomare, A.; Burla, M. C.; Camalli, M.; Cascarano, G. L.; Giacovazzo, C.; Guagliardi, A.; Moliterni, A. G. G.; Polidori, G.; Spagna, R. *J. Appl. Crystallogr.* **1999**, *32*, 115.

(16) Sheldrick, G. *Acta Cryst. A* **2008**, *64*, 112.

(17) Kirschbaum, K.; Martin, A.; Pinkerton, A. A. *J. Appl. Crystallogr.* **1997**, *30*, 514.

(18) Grin, Y. N.; Yarmolyuk, Y. P.; Gladyshevskii, E. I. *Kristallografiya* **1979**, *24*, 242.

(19) Banks, M. G.; Kremer, R. K.; Mannix, D.; Lapertot, G.; Murani, A. P. *Los Alamos Natl. Lab., Prepr. Arch., Condens. Matter* **2007**, 1.

(20) Czopnik, A.; Iliew, N.; Stalinski, B.; Maedge, H.; Bazan, C.; Pott, R. *Physica B* **1985**, *130*, 262.

(21) Morin, P.; Giraud, M.; Regnault, P. L.; Roudaut, E.; Czopnik, A. *J. Magn. Magn. Mater.* **1987**, *66*, 345.

(22) Murasik, A.; Czopnik, A.; Keller, L.; Fischer, P. *J. Magn. Magn. Mater.* **2000**, *213*, 101.

(23) Biasini, M.; Kontrym-Sznajd, G.; Monge, M. A.; Gemmi, M.; Czopnik, A.; Jura, A. *Phys. Rev. Lett.* **2001**, *86*, 4616.

(24) Samsel-Czekała, M.; Kontrym-Sznajd, G.; Biasini, M. *Phys. Status Solidi C* **2006**, *3*, 179.

(25) Gubbens, P. C. M.; Van, d. K. A. M.; Buschow, K. H. J. *Hyperfine Interact.* **1986**, *29*, 1343.

(26) Pluzhnikov, V. B.; Czopnik, A.; Grechnev, G. E. *J. Phys. Condens. Mat.* **1999**, *11*, 4507.

(27) Chen, Y. Y.; Yao, Y. D.; Wang, C. R.; Lin, S. H.; Czopnik, A.; Ali, M. R.; Ho, J. C. *Phys. Rev. B* **2002**, *66*, 212404/1.

(28) Deutz, A. F.; Brom, H. B.; Huiskamp, W. J.; De, J. L. J.; Buschow, K. H. J. *Physica B* **1989**, *160*, 83.

(29) Czopnik, A. *Phys. Status Solidi A* **1995**, *147*, K35.

CHAPTER 5. CONCLUSIONS

The work presented in this dissertation has illustrated how single crystal growth is strongly dependent on reaction conditions. Compounds adopting different structure types are obtained by making minor adjustments in reaction ratios, as exhibited by $Ln(Mn,Al)_{12}$ (Ln = Gd, Yb), $Yb(Mn,M)_xAl_{12-x}$ (M = Fe, Ru; $x \leq 2.5$), and $LnMn_xGa_3$ (Ln = Ho – Tm; x = 0 – 0.15). $Yb(Mn,Al)_{12}$ compounds can crystallize in either the $ThMn_{12}$ structure type, where Yb is trivalent, when the Yb:Mn ratio in the reaction ratio is 1:9, or the $CaCr_2Al_{10}$ structure type, where Yb is divalent and Mn is magnetic, when the ratio of Yb:Mn in the reaction ratio is 1:<9.[1] For $Yb(Mn,M)_xAl_{12-x}$ (M = Fe, Ru; $x \leq 2.5$), compounds may adopt the $ThMn_{12}$ structure type when the Yb:(Mn+Fe/Ru) ratio is 1:4, or the $CaCr_2Al_{10}$ or $YbFe_2Al_{10}$ structure type when the ratio of Yb:(Mn+Fe/Ru) is 1:3. Additionally, changes of the ratio of Mn:Fe/Ru determine whether the product will crystallize in the $CaCr_2Al_{10}$ structure type (5:1 reaction ratios of Mn:Fe/Ru) or the $YbFe_2Al_{10}$ structure type (2:1 and 1:1 reaction ratios of Mn:Fe/Ru).[2] When Fe is substituted for Mn in these compounds the products favor adoption of the $YbFe_2Al_{10}$ structure type, and for $Yb(Mn,Fe)_xAl_{12-x}$ adopting the $ThMn_{12}$ structure type the substitution of Fe for Mn destabilizes Yb from a +3 state to a +2 or intermediate valent state. Finally, $LnMn_xGa_3$ (Ln = Ho-Tm; $x < 0.15$) adopt the $AuCu_3$ structure type when Mn is not present, or the "stuffed" variant of the $AuCu_3$ structure type when Mn is present, which represents a structural bridge between $LnGa_3$ compounds adopting the $AuCu_3$ structure type and Ln_4MGa_{12} compounds adopting the Y_4PdGa_{12} structure type. These compounds exhibit interesting magnetic behavior, such as a simultaneous decrease of effective magnetic moments with increasing Mn concentration for Ho and Er analogues, while magnetization values increase with increasing Mn concentration. In every case presented in this work, the growth of high quality single crystals facilitated product characterization in terms of the elucidation of structural, magnetic, and

electrical properties. Additionally, synthesis of high quality single crystals of the aforementioned intermetallic compounds allowed us to uncover subtle differences in physical properties between those compounds. All these examples illustrate the importance of crystal growth in advancing the field of solid state chemistry and other related fields.

Related to this work, we recently grew single crystals of $ScFeGa_5$ adopting the $HoCoGa_5$ structure type.[3] This synthesis was performed in order to investigate the effect of decreasing the size of the Ln atom in Ln_4FeGa_{12} compounds, for which the series end-member is $Er_4Fe_{0.67}Ga_{12}$ adopting a disordered variant of the Y_4PdGa_{12} structure type.[4] We wished to investigate whether or not replacing Er with Sc in $Er_4Fe_{0.67}Ga_{12}$ would result in the growth of $ScMn_xGa_3$ in the stuffed $AuCu_3$ structure type. Instead, we grew $ScFeGa_5$. The $AuCu_3$ structure type and the $HoCoGa_5$ structure type are homologous series (Figure 5.1), and the discovery of $ScFeGa_5$ provides the opportunity to further study structural stabilities in competing intermetallic Ln-M-Ga phases.

This work also presents additional opportunities for future endeavors. The results of our synthetic work with $LnMn_xGa_3$ compounds adopting the stuffed $AuCu_3$ structure type have raised some interesting questions regarding what parameters most influence the formation of these compounds. A collection of synthetic work has been performed with related phases such as Ln_4CrGa_{12}[5] and Ln_4FeGa_{12}[4] compounds adopting the Y_4PdGa_{12} structure type, as well as $LnMGa_5$[3] compounds adopting the $HoCoGa_5$ structure type. Given the structural similarities between all these compounds and the wide range of lanthanides and transition metals these compounds may accommodate, it would be of interest theoretically to address questions about what parameters determine the formation of these phases. Indeed, such questions are already being addressed. Currently, theoretical work is being done in an attempt to explain in terms of

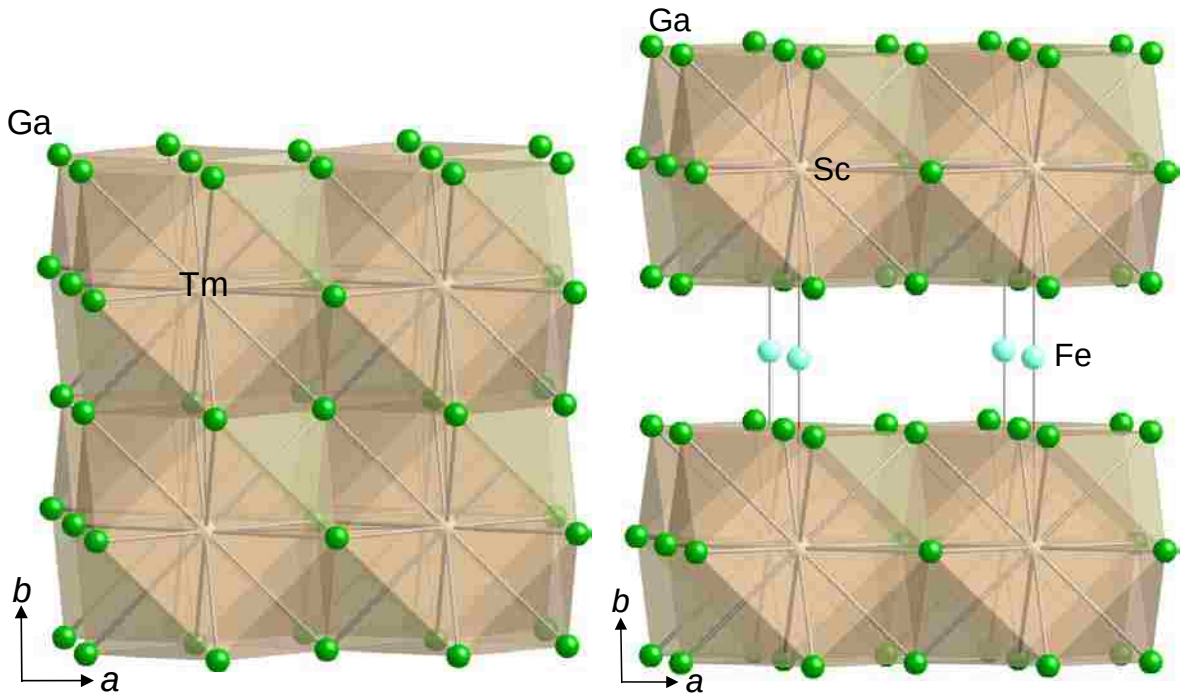

Figure 5.1. $TmGa_3$ of the $AuCu_3$ structure type (left, where Ga is green and Tm is tan) is shown in relation to $ScFeGa_5$ of the $HoCoGa_5$ structure type (right, where Ga is green, Sc is tan, and Fe is light blue). The face-sharing Ln-centered cuboctahedra of $TmGa_3$ are separated by a transition metal slab in $ScFeGa_5$.

chemical pressure the tendency of Ln_4FeGa_{12} compounds to adopt the Y_4PdGa_{12} structure type instead of a "stuffed" variant of the $AuCu_3$ structure type. Given the discoveries made with $LnMn_xGa_3$ compounds, and future discoveries involving compounds related to $ScFeGa_5$, theoretical efforts can grow to encompass a broad range of Ln-M-Ga-based phases. These potential avenues of research could yield exciting and meaning results for those researchers who are willing to examine them. Alternatively, there remain unanswered questions regarding the role played by crystal electric fields in the magnetic properties of the $LnMn_xGa_3$ compounds reported in this work. Given the experimental work done to elucidate the crystal electric field effects in compounds such as $ErGa_3$ and $TmGa_3$ (as mentioned in Chapter 4 of this document), combined with the groundwork of synthesis, structural characterization, and first order characterization of magnetic properties for $LnMn_xGa_3$ compounds, it would be of interest to

further investigate the electrical properties and anisotropic magnetic properties of $LnMn_xGa_3$ in order to uncover the physical reasons behind some of the unusual magnetic behavior of these compounds. In this fashion, the growth of single crystals discussed in this document can spur future research efforts to yield increased discoveries.

There is quite a large number of aluminum and gallium based intermetallic compounds reported in the literature, with a similarly wide variety of physical behavior. When taking into account intermetallic compounds grown from different metal fluxes (Sn, Pb, or In, for example) and mixed metal fluxes (eutectic fluxes), in addition to salt fluxes, the number of known intermetallic compounds grows even larger. Unfortunately, the ability of the solid state community to predict new intermetallic compounds is lagging behind the ability of the community to synthesize new compounds. This lag in the ability to predict new compounds points to a need for increased understanding about how elements come together in solid state materials. Identifying structural motifs that correlate with certain physical behavior is a vital stepping stone to achieving a deeper understanding about condensed matter physics and to technological advancement. Having the tools to preferentially synthesize a certain material is also an important part of advancing the field. However, perhaps the most effective way to advance our understanding of solid state chemistry is by continuing to search for new materials with exciting properties. Towards these ends, flux growth is a powerful technique that will continue to produce many kinds of novel materials. We will require these materials in order to increase our understanding of how structures and properties correlate in solid state matter, and perhaps to gain a more complete understanding of which combination of elements will yield materials with desirable properties.

5.2 References

(1) Fulfer, B. W.; Haldolaarachchige, N.; Young, D. P.; Chan, J. Y. *J. Solid State Chem.* **2012**, *194*, 143.

(2) Fulfer, B. W.; McAlpin, J. D.; Haldolaarachchige, N.; Young, D. P.; Chan, J. Y. *Cryst. Growth Des.* **2013**, *13*, 1543.

(3) Grin, Y. N.; Yarmolyuk, Y. P.; Gladyshevskii, E. I. *Kristallografiya* **1979**, *24*, 242.

(4) Drake, B. L.; Grandjean, F.; Kangas, M. J.; Okudzeto, E. K.; Karki, A. B.; Sougrati, M. T.; Young, D. P.; Long, G. J.; Chan, J. Y. *Inorg. Chem.* **2010**, *49*, 445.

(5) Slater, B. R.; Bie, H.; Stoyko, S. S.; Bauer, E. D.; Thompson, J. D.; Mar, A. *J. Solid State Chem.* **2012**, *196*, 409.

APPENDIX A. STRUCTURAL CHARACTERIZATION OF MnGe SINGLE CRYSTALS

A.1 Objective

To determine if a structural distortion was occurring around 170 K from a primitive cubic unit cell to a primitive orthorhombic unit cell in a sample of single crystalline MnGe,[1] we performed multiple collections of intensity data via single crystal X-ray diffraction at several temperatures above and below 170 K.

A.2 Procedure and Results

A small crystal was cut from the single crystalline MnGe sample provided by the Department of Physics and Astronomy at Louisiana State University. This small crystal was mounted on a glass fiber using vacuum grease and fixed to a goniometer head. Diffraction data were collected using an Enraf Nonius Kappa CCD single crystal X-ray diffractometer equipped with a Mo Ka radiation source ($\lambda = 0.71073$ Å). Temperature was controlled using a Cryostream Controller 700 manufactured by Oxford Cryosystems. Intensity data were collected at 180 K, 175 K, 170 K, 165 K, 160 K, and 165 K in order to determine if an orthorhombic distortion was occuring in the vicinity of 170 K. Unit cell parameters derived from these data are summarized in Figures A.1a-d. Unit cell parameters exhibit an unexpected decrease at 160 K, and are otherwise unremarkable. Structural models were solved by direct methods using SIR97[2] and were refined using SHELLXL97.[3] Crystallographic parameters and atomic positions are given for the structural model of MnGe derived from intensity data collected at 160 K in Tables A.1 and A.2. Analysis of all the crystallographic data collected on MnGe indicates cubic cell symmetry. The uncertainties associated with the unit cell parameters make it impossible to come to any meaningful conclusions regarding the possible orthorhombic distortion of MnGe.

However, given the small change in unit cell parameters that have been reported for MnGe[1] (volume reduction from ~110.0 to 109.6 Å^3) and the large uncertainties of our lattice parameters based on our data collections, it is probable that we lack the requisite resolution to identify such a minute distortion of cubic symmetry.

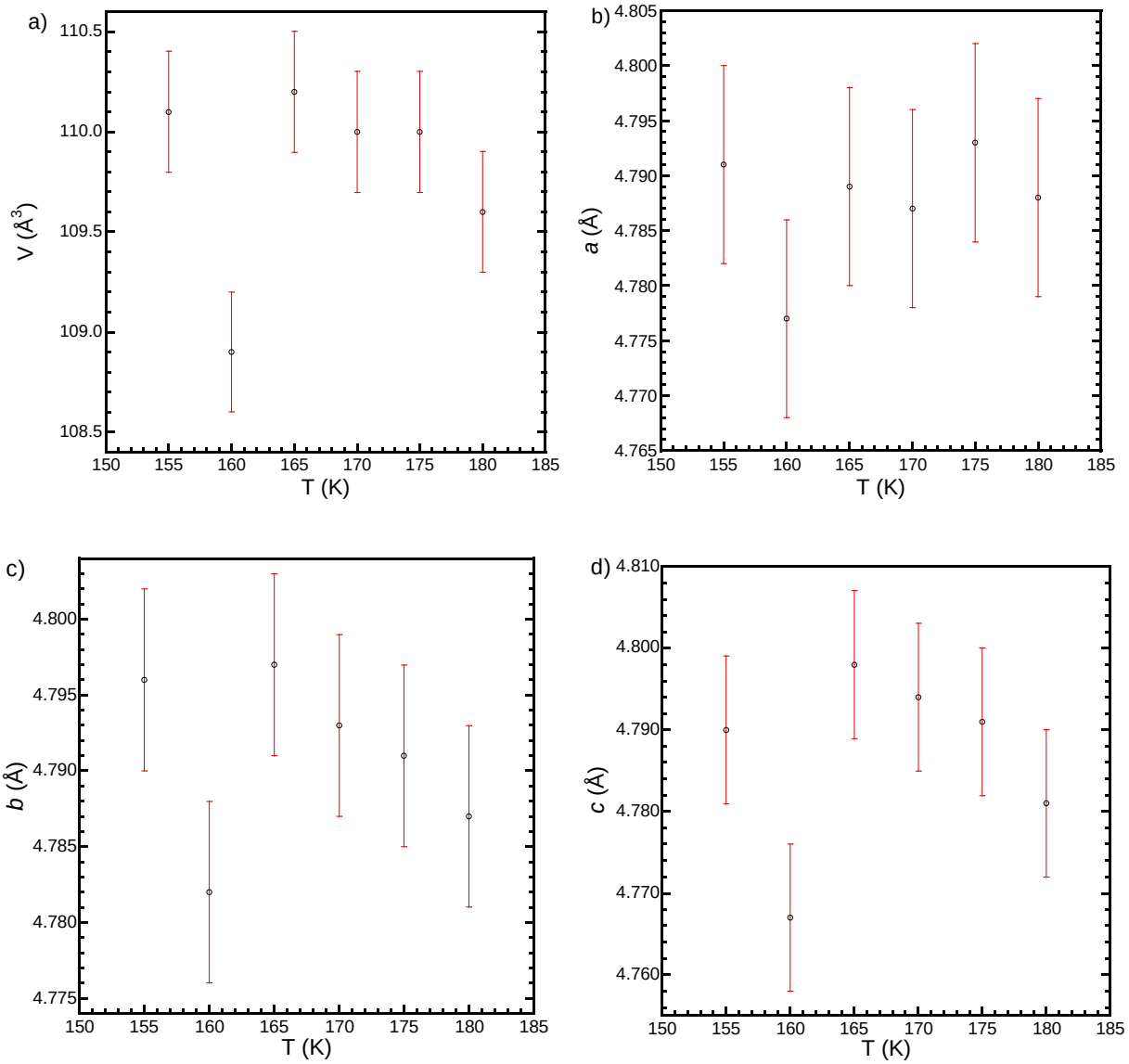

Figure A.1. Temperature dependencies of the a) unit cell volume, and the lattice parameters b) *a*, c) *b*, and d) *c*.

Table A.1. Crystallographic parameters for data collected at 160 K

Crystal data		
Formula	**MnGe(ortho)**	**MnGe(cubic)**
Space group	$P2_12_12_1$	$P2_13$
a (Å)	4.788(3)	4.787(2)
b (Å)	4.786(3)	4.787(2)
c (Å)	4.784(3)	4.787(2)
V (Å^3)	109.65(11)	109.71(8)
Z	4	4
Crystal size (mm^3)	0.02 x 0.04 x 0.04	0.02 x 0.04 x 0.04
Temperature (K)	165(1)	165(1)
Density (g cm^{-3})	7.726	7.721
θ Range (°)	6.03-33.08	6.03-34.12
μ (mm^{-1})	37.940	37.918
Data Collection and Refinement		
Collected reflections	2657	2653
Unique reflections	288	99
R_{int}	0.113	0.119
h	$-7 \le h \le 7$	$-5 \le h \le 5$
k	$-7 \le k \le 7$	$-7 \le k \le 7$
l	$-7 \le l \le 7$	$-4 \le l \le 4$
$\Delta\rho_{max}$ (e Å^{-3})	2.263	1.030
$\Delta\rho_{min}$ (e Å^{-3})	-1.789	-0.918
GoF	1.099	1.105
Extinction coefficient	0.000(3)	0.002(5)
[a] $R_1(F)$ for $F_o^2 > 2\sigma(F_o^2)$	0.0462	0.0319
[b] $R_w(F_o^2)$	0.0889	0.0685

[a] $R_1 = \Sigma||F_o| - |F_c||/\Sigma|F_o|$
[b] $wR_2 = [\Sigma w(F_o^2 - F_c^2)^2/\Sigma w(F_o^2)^2]^{1/2}$; $w = 1/[\sigma^2(F_o^2) + (0.0404P)^2 + 1.5589P]$ and $w = 1/[\sigma^2(F_o^2) + (0.0303P)^2 + 1.3085P]$ at 160 K for MnGe(ortho) and MnGe(cubic), respectively.

Table A.2. Atomic positions for MnGe characterized at 160 K

Atom	Wyckoff position	x	y	z	Occ.	U_{eq} (Å^2)
MnGe(ortho)						
Mn	4*a*	0.1382(3)	0.1374(3)	0.1375(3)	1.00	0.0054(3)
Ge	4*a*	0.8439(2)	0.8438(2)	0.8437(2)	1.00	0.0058(3)
MnGe(cubic)						
Mn	4*a*	0.1377(2)	*x*	*x*	1.00	0.0056(4)
Ge	4*a*	0.84388(15)	*x*	*x*	1.00	0.0059(3)

A.3 References

(1) Makarova, O. L.; Tsvyashchenko, A. V.; Andre, G.; Porcher, F.; Fomicheva, L. N.; Rey, N.; Mirebeau, I. *Phys. Rev. B* **2012**, *85*, 205205/1.

(2) Altomare, A.; Burla, M. C.; Camalli, M.; Cascarano, G. L.; Giacovazzo, C.; Guagliardi, A.; Moliterni, A. G. G.; Polidori, G.; Spagna, R. *J. Appl. Crystallogr.* **1999**, *32*, 115.

(3) Sheldrick, G. *Acta Cryst. A* **2008**, *64*, 112.

APPENDIX B. STRUCTURAL CHARACTERIZATION OF $Bi_2Ir_2O_7$ PYROCHLORE*

B.1 Objective

To study the electronic structure of the metallic pyrochlore $Bi_2Ir_2O_7$ via infrared spectroscopy, high quality single-crystalline $Bi_2Ir_2O_7$ was characterized via single crystal X-ray diffraction at Louisiana State University and at the Advanced Light Source at the Lawrence Berkeley National Laboratory.

B.2 Procedure and Results

Crystallographic data were collected initially at room temperature on a Nonius KappaCCD single crystal diffractometer using Mo Kα radiation (λ = 0.71073 Å). The crystal structure of $Bi_2Ir_2O_7$ was solved by direct methods using SIR97[1] and refined using SHELXL97.[2] The final model contains anisotropically modeled atomic displacement parameters and extinction corrections. Crystallographic parameters, atomic positions, anisotropic thermal parameters, and interatomic distances are given in Tables B.1-3.

Diffraction images collected on the Nonius diffractometer showed very low intensity peaks resulting from high absorption of Mo Kα radiation by the sample. Consequential refinement of crystallographic models contained unreasonably large and directionally anisotropic thermal parameter values for the oxygen atoms. Increasing sample size and X-ray beam exposure time proved to be an inefficient means of solving this problem, and so single crystal diffraction data were also collected at the Advanced Light Source at the Lawrence Berkeley National Laboratory for further structural elucidation.

---

*Reprinted with permission from Lee, Y. S.; Moon, S. J.; Riggs, S. C.; Shapiro, M. C.; Fisher, I. R.; Fulfer, B. W.; Chan, J. Y.; Kemper, A. F.; Basov, D. N., Infrared study of the electronic structure of the metallic pyrochlore iridate $Bi_2Ir_2O_7$. *Phys. Rev. B* **2013,** *87,* 195143.

Crystallographic data were also collected at 150 K on a D8 goniostat equipped with APEXII CCD detector at Beamline 11.3.1 at the Advanced Light Source at the Lawrence Berkeley National Laboratory using synchrotron radiation tuned to λ = 0.7749 Å. Frames were measured for 3 s at 0.5° intervals of ω with a maximum 2θ of ~60°. Data were collected using the APEX2 program and processed using the SAINT program routine within the APEX2 software. The data were corrected for adsorption and beam corrections based on the multi-scan technique as implemented by SADABS. Structural models were refined using the SHELXL97[2] program. Structural models were corrected for extinction and refined with anisotropic atomic displacement parameters. Crystallographic parameters, atomic positions and displacement parameters, anisotropic thermal parameters, and interatomic distances are given in Tables B.1-3.

$Bi_{1.94(1)}Ir_2O_{6.91(3)}$ adopts the pyrochlore structure type ($Fd\bar{3}m$ space group) and has the lattice parameter a = 10.312(7) Å. Upon refinement of the model solved from data collected at the Advanced Light Source, it was found that occupancies on the Bi and O2 sites return slight deviations from full occupancy, giving the compound the chemical formula $Bi_{1.94(1)}Ir_2O_{6.91(3)}$. The occupancy is similar to the previously reported structure solved from neutron diffraction data.[3] The increased radiation intensity at the ALS proved crucial in determining the oxygen vacancies present in this compound, as no partial occupancy on any site was discernable for all crystallographic models solved using data collected on the laboratory instrument. Values for Bi-O and Ir-O bond distances are in agreement with previously reported distances[3] and indicate that Ir is in the +4 oxidation state and that Bi is in the +3 oxidation state.

Table B.1. Crystallographic parameters for $Bi_2Ir_2O_7$

Crystal data		
Formula	**$Bi_2Ir_2O_7$**	**$Bi_{1.94(1)}Ir_2O_{6.91(3)}$ (synch)**
Space group	$Fd\bar{3}m$	$Fd\bar{3}m$
a (Å)	10.314(3)	10.312(7)
V (Å^3)	1197.3(5)	1196.6(12)
Z	8	8
Crystal size (mm)	0.10 x 0.10 x 0.10	0.002 x 0.005 x 0.10
Temperature (K)	294(2)	150(2)
Density (g cm^{-3})	11.070	10.910
θ Range (°)	5.59-33.67	3.73-30.92
μ (mm^{-1})	112.297	125.486
Data Collection and Refinement		
Collected reflections	6470	2306
Unique reflections	170	85
R_{int}	0.072	0.1102
h	$2 \le h \le 15$	$-13 \le h \le 13$
k	$0 \le k \le 10$	$-13 \le k \le 13$
l	$0 \le l \le 10$	$-13 \le l \le 13$
$\Delta\rho_{max}$ (e Å^{-3})	1.658	2.180
$\Delta\rho_{min}$ (e Å^{-3})	-1.563	-4.001
Goodness of fit	1.287	1.199
Extinction coefficient	0. 23(10)	0. 00033(8)
[a] $R_1(F)$ for $F_o^2 > 2\sigma(F_o^2)$	0.0256	0.0391
[b] $R_w(F_o^2)$	0.0845	0.0814

[a] $R_1 = \Sigma||F_o| - |F_c||/\Sigma|F_o|$
[b] $wR_2 = [\Sigma w(F_o^2 - F_c^2)^2/\Sigma w(F_o^2)^2]^{1/2}$; $w = 1/[\sigma^2(F_o^2) + 0.0443P^2 + 35.4143P]$ at 294 K for $Bi_2Ir_2O_7$ and $w = 1/[\sigma^2(F_o^2) + 0.0353P^2 + 2.7862P]$ at 150 K for $Bi_{1.94(1)}Ir_2O_{6.91(3)}$.

Table B.2. Atomic positions and displacement parameters for $Bi_2Ir_2O_7$

Atom	Wyckoff position	x	y	z	Occ.	U_{eq} ($Å^2$)
$Bi_2Ir_2O_7$						
Bi	16*d*	1/2	1/2	1/2	1.00	0.0136(9)
Ir	16c	0	0	0	1.00	0.0150(10)
O1	48*f*	0.340 (2)	1/8	1/8	1.00	0.069(11)
O2	8*b*	3/8	3/8	3/8	1.00	0.056(17)
$Bi_{1.94(1)}Ir_2O_{6.91(3)}$						
Bi	16*d*	1/2	1/2	1/2	0.971(3)	0.0149(8)
Ir	16*c*	0	0	0	1.00	0.0049(7)
O1	48*f*	0.3305(5)	1/8	1/8	1.00	0.0097(12)
O2	8*b*	3/8	3/8	3/8	0.91(3)	0.023(4)

Note: The top set is modeled from the data taken at LSU, the bottom set is modeled from the data taken at the ALS.

Table B.3. Interatomic distances for $Bi_2Ir_2O_7$

Interatomic distance	**$Bi_2Ir_2O_7$**	**$Bi_{1.94(1)}Ir_2O_{6.91(3)}$**
Bi-O2 (x2)	2.234(2)	2.2326(9)
Bi -O1 (x6)	2.460(14)	2.526(4)
Ir-O1(x6)	2.046(13)	2.003(3)

B.3 References

(1) Altomare, A.; Burla, M. C.; Camalli, M.; Cascarano, G. L.; Giacovazzo, C.; Guagliardi, A.; Moliterni, A. G. G.; Polidori, G.; Spagna, R. *J. Appl. Crystallogr.* **1999**, *32*, 115.

(2) Sheldrick, G. *Acta Cryst. A* **2008**, *64*, 112.

(3) Kennedy, B. J. *J. Solid State Chem.* **1996**, *123*, 14.

APPENDIX C. STRUCTURAL CHARACTERIZATION OF $(Mg,Yb)_{19}S_{19}$

C.1 Objective

To elucidate the crystal structure of single crystals of an unidentified Mg-Yb-S based compound, single crystal X-ray diffraction data were collected at Louisiana State University.

C.2 Procedure and Results

Single crystals of an unknown Mg-Yb-S based compound were received from the group of Dr. Satoru Nakatsuji from the University of Tokyo. The crystals are yellow and translucent, and adopt a triangular plate-like morphology. The crystals are moderately reactive to water, and prolonged exposure to ambient atmosphere results in crystal decomposition. Select single crystal samples were cut to appropriate sizes and fixed to thin glass fibers using epoxy. The crystals were mounted on a goniometer head of an Enraf Nonius single crystal X-ray diffractometer equipped with Mo Kα radiation (λ = 0.71073 Å) and a Kappa CCD detector. Intensity data were collected at room temperature and at 100 K. Analysis of the data reveal that the compounds crystallizes in a trigonal unit cell with lattice parameters $a \sim 16.6$ Å, $c \sim 9.3$ Å, $\alpha = 90°$, and $\gamma = 120°$. Structural models were obtained via direct methods using SIR97[1] and structural models were refined with SHELXL97.[2] Structural models were further improved by modeling atomic displacement parameters anisotropically and by correcting for extinction. Crystallographic parameters and data collection parameters, atomic positions and displacement parameters, and interatomic distances are given in Tables C.1-4.

Table C.1. Crystallographic parameters, collection parameters, and refinement parameters for $Mg_{14.03(7)}Yb_{4.97(7)}S_{19}$ and $Mg_{14.68(5)}Yb_{4.32(5)}S_{19}$.

Formula	$Mg_{14.03(7)}Yb_{4.97(7)}S_{19}$	$Mg_{14.68(5)}Yb_{4.32(5)}S_{19}$
Crystal System	Trigonal	Trigonal
Space Group	*R*-3	*R*-3
a (Å)	16.637(4)	16.6075(2)
b(Å)	16.637(4)	16.6075(2)
c (Å)	9.336(4)	9.3054(15)
V (Å^3)	2237.9(12)	2222.7(4)
Z	3	3
Crystal dimensions (mm)	0.05 x 0.05 x 0.075	0.05 x 0.05 x 0.075
Temperature (K)	295(1)	100(1)
θ range (º)	2.6 - 30.02	3.58 - 30
μ (mm^{-1})	17.066	15.181
Data Collection		
Measured Reflections	10386	19823
Unique Reflections	1453	1437
Reflections with I>2σ(I)	864	1181
R_{int}	0.0708	0.0248
h	-23 to 23	-23 to 23
k	-19 to 19	-19 to 19
l	-13 to 13	-13 to 13
Refinement		
$\Delta\rho_{max}$ (eÅ^{-3})/$\Delta\rho_{min}$ (eÅ^{-3})	1.817 / -1.172	2.508 / -1.276
GoF	0.978	1.115
Extinction coefficient	0.00154(13)	0.0036(2)
Reflections/Parameters	1453 / 63	1437 / 63
R_1 ($F^2 > 2\sigma F^2$) [a]	0.0578	0.0413
wR_2 (F^2) [b]	0.1117	0.0898

Table C.2. Atomic positions for $Mg_{14.03(7)}Yb_{4.97(7)}S_{19}$ taken at 295 K.

Atom	Site	*x*	*y*	*z*	Occ.	*U*eq (Å^2) [a]
Yb1	3*a*	0	0	0	1	0.0186(3)
Mg2/Yb2	18*f*	0.03516(5)	0.27565(7)	0.32977(8)	0.774(4)/0.226(4)	0.0149(5)
Mg3/Yb3	18*f*	0.01830(5)	0.14499(7)	0.66477(8)	0.767(4)/0.233(4)	0.0190(5)
Mg4/Yb4	18*f*	0.15989(6)	0.26577(6)	0.00213(9)	0.798(4)/0.202(4)	0.0164(6)
S1	3*b*	0	0	0.5	1	0.0459(15)
S2	18*f*	0.01752(11)	0.13676(12)	0.16233(16)	1	0.0214(5)
S3	18*f*	0.07012(13)	0.56134(12)	0.16735(18)	1	0.0341(7)
S4	18*f*	0.05175(14)	0.42116(14)	0.49985(19)	1	0.0373(7)

[a]U_{eq} is defined as one-third of the trace of the orthagonalized U_{ij} tensor.

Table C.3. Atomic positions for $Mg_{14.68(5)}Yb_{4.32(5)}S_{19}$ taken at 100 K.

Atom	Site	*x*	*y*	*z*	Occ.	*U*eq (Å^2) [a]
Yb1	3*a*	0	0	0	1	0.01281(16)
Mg2/Yb2	18*f*	0.03505(3)	0.27481(5)	0.32916(6)	0.806(3)/0.194(3)	0.0099(4)
Mg3/Yb3	18*f*	0.01849(4)	0.14598(5)	0.66450(5)	0.804(3)/0.196(3)	0.0135(4)
Mg4/Yb4	18*f*	0.16018(4)	0.26615(4)	0.00249(6)	0.836(3)/0.164(3)	0.0101(4)
S1	3*b*	0	0	0.5	1	0.0422(10)
S2	18*f*	0.01737(7)	0.13638(7)	0.16240(10)	1	0.0177(4)
S3	18*f*	0.07032(7)	0.56137(8)	0.16786(12)	1	0.0307(6)
S4	18*f*	0.05126(9)	0.42079(9)	0.49984(13)	1	0.0339(6)

[a] U_{eq} is defined as one-third of the trace of the orthagonalized U_{ij} tensor.

Table C.4. Select interatomic distances for $(Mg,Yb)_{19}S_{19}$ compounds.

Bond distance (Å)	$\mathbf{Mg_{14.03(7)}Yb_{4.97(7)}S_{19}}$	$\mathbf{Mg_{14.68(5)}Yb_{4.32(5)}S_{19}}$
Yb1-S2 (x6)	2.626(2)	2.6161(15)
Mg2/Yb2		
-S3	2.680(3)	2.6740(10)
-S2	2.682(2)	2.6655(15)
-S3	2.6884(18)	2.6748(10)
-S3	2.7100(18)	2.7117(10)
-S4	2.716(3)	2.7059(15)
-S4	2.791(3)	2.7965(15)
Mg3/Yb3		
-S3	2.6534(18)	2.6343(10)
-S4	2.656(3)	2.6446(15)
-S3	2.665(3)	2.6537(10)
-S2	2.7361(17)	2.7375(10)
-S2	2.742(2)	2.7396(10)
-S1	2.7465(12)	2.7515(15)
Mg4/Yb4		
-S3	2.657(2)	2.6449(15)
-S4	2.6657(19)	2.6536(10)
-S4	2.694(3)	2.6891(10)
-S4	2.710(3)	2.7086(10)
-S2	2.7148(17)	2.7153(15)
-S2	2.741(2)	2.7416(15)

We report $(Mg,Yb)_{19}S_{19}$ crystallizing in the trigonal space group $R\bar{3}$ (space group 148). This compound consists of edge sharing octahedra that extend in three dimensions (Figure C.1). Every S anion is coordinated to six Mg or Yb cations and every Mg or Yb cation is coordinated

by six S anions. There is evidence in data collected at room temperature and at 100 K for mixing of Mg and Yb on all cationic sites except for the Yb1 site. According to modeled site occupancies, the stoichiometry of the compound is $Mg_{14.4(9)}Yb_{4.6(9)}S_{19}$ (found by averaging occupancies of structural refinements from data collected at room temperature and at 100 K). Interatomic distances are close to the sum of Shannon's ionic radii[3] for 6-coordinate S^{2-} (1.84 Å) and 6-coordinate Yb^{2+} (1.02 Å) or 6-coordinate S^{2-} and 6-coordinate Mg^{2+} (0.72 Å). To the best of our knowledge, this compound has not yet been reported.

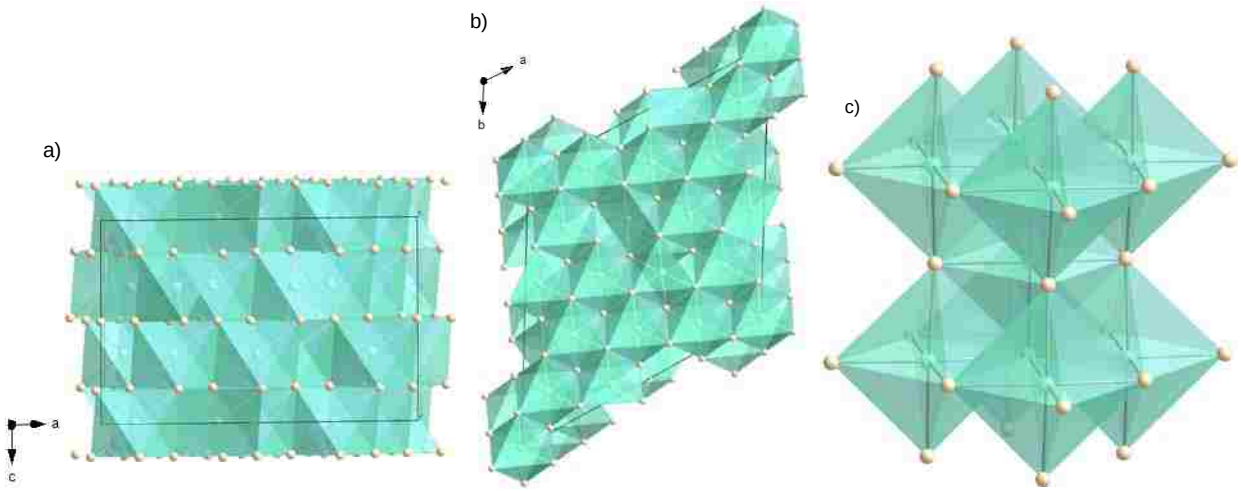

Figure C.1. Depiction of the crystal structure of $(Mg,Yb)_{19}S_{19}$ a) down the *b* axis and b) down the *c* axis, where light blue spheres represent cations and tan spheres represent anions. Edge-sharing octahedra are also shown in c).

C.3 References

(1) Altomare, A.; Burla, M. C.; Camalli, M.; Cascarano, G. L.; Giacovazzo, C.; Guagliardi, A.; Moliterni, A. G. G.; Polidori, G.; Spagna, R. *J. Appl. Crystallogr.* **1999**, *32*, 115.

(2) Sheldrick, G. *Acta Cryst. A* **2008**, *64*, 112.

(3) Shannon, R. *Acta Cryst. A* **1976**, *32*, 751.

APPENDIX D. STRUCTURAL CHARACTERIZATION OF ZrM_xZn_{22-x} (M = Cr-Cu) WITH SINGLE CRYSTAL X-RAY DIFFRACTION

D.1 Objective

To investigate structural trends and transition metal concentrations over a range of transition metal analogues of ZrM_xZn_{22-x} (M = Cr-Cu) compounds, we characterized single crystalline samples via single crystal X-ray diffraction.

D2. Procedure and Results

Single crystalline samples of ZrM_xZn_{22-x} (M = Cr-Cu) were obtained from the group of Emilia Morosan in the Department of Physics and Astronomy at Rice University. Single crystals suitable for X-ray diffraction experiments were obtained by cutting the samples with pliers in order to access crystalline material on the interior of the sample ingots. In the process of cutting the samples, multiple fractured single crystals were obtained that were of the appropriate size for data collection (~ 100 μm^3). These single crystals were a dark silver color and possessed metallic luster. Crystals were fixed to thin glass fibers with epoxy, then mounted on the goniometer head of an Enraf Nonius single crystal X-ray diffractometer equipped with a Kappa CCD detector and a Mo Kα radiation source (λ = 0.71073 Å). All intensity data were collected at room temperature. Structural models were obtained with direct methods using SIR97[1] and models were refined with SHELXL97.[2] Final models include extinction corrections and anisotropically modeled atomic displacement parameters. Crystallographic parameters and data collection parameters, atomic positions and displacement parameters, and selected interatomic distances are given in Tables D.1-3.

Table D.1a. Crystallographic parameters for annealed ZrM_xZn_{22-x} compounds

Formula	**$ZrCr_{0.98(4)}Zn_{21.02(4)}$**	**$ZrMn_{1.78(10)}Zn_{20.22(10)}$**	**$ZrFe_2Zn_{20}$**	**$ZrCo_2Zn_{20}$**	**$ZrNi_2Zn_{20}$**	**$ZrCu_2Zn_{20}$**
EDS Composition	$Zr_{1.0(3)}Cr_{0.59(12)}Zn_{15(2)}$	$Zr_{1.0(3)}Mn_{1.1(2)}Zn_{12(2)}$	$Zr_{1.0(3)}Fe_{1.3(3)}Zn_{10.5(16)}$	$Zr_{1.0(8)}Co_{1.7(8)}Ga_{16(7)}$	$Zr_{1.0(4)}Ni_{1.2(3)}Zn_{10(2)}$	$Zr_{1.0(3)}Cu_{1.2(3)}Zn_{12(2)}$
Synthesis	EJ845(annealed)	EJ650(annealed)	EJ651(annealed)	EJ562(annealed)	EJ833(annealed)	EJ834(annealed)
Space group	$Fd\bar{3}m$	$Fd\bar{3}m$	$Fd\bar{3}m$	$Fd\bar{3}m$	$Fd\bar{3}m$	$Fd\bar{3}m$
a (Å)	14.1208(10)	14.0640(15)	13.9554(10)	13.9071(10)	13.9041(15)	14.0116(15)
V (Å^3)	2815.6(3)	2781.8(5)	2717.9(3)	2689.7(3)	2688.0(5)	2750.8(5)
Z	8	8	8	8	8	8
Crystal size (mm^3)	0.08 x 0.08 x 0.16	0.03 x 0.05 x 0.08	0.05 x 0.05 x 0.08	0.03 x 0.05 x 0.05	0.02 x 0.06 x 0.08	0.02 x 0.06 x 0.06
Temperature (K)	295(1)	295(1)	295(1)	295(1)	295(1)	295(1)
Density (g cm^{-3})	7.154	7.204	7.382	7.490	7.492	7.368
θ Range (°)	4.08-33.14	1.02-31.51	2.53-32.41	4.14-32.54	4.15-32.54	4.11-32.26
μ (mm^{-1})	36.422	36.152	37.279	37.978	38.336	37.816
Data Collection and Refinement						
Collected reflections	12376	10413	10029	10466	10413	10027
Unique reflections	508	440	463	460	463	463
R_{int}	0.068	0.097	0.061	0.073	0.092	0.102
h	$-21 \le h \le 21$	$-20 \le h \le 20$	$-21 \le h \le 21$	$-21 \le h \le 21$	$-21 \le h \le 21$	$-21 \le h \le 21$
k	$-15 \le k \le 15$	$-14 \le k \le 14$	$-14 \le k \le 14$	$-14 \le k \le 14$	$-14 \le k \le 14$	$-14 \le k \le 14$
l	$-14 \le l \le 14$	$-13 \le l \le 13$	$-13 \le l \le 13$	$-13 \le l \le 13$	$-13 \le l \le 13$	$-13 \le l \le 13$
$\Delta\rho_{max}$ (e Å^{-3})	0.940	1.426	0.747	1.253	1.102	1.159
$\Delta\rho_{min}$ (e Å^{-3})	-0.787	-1.105	-0.682	-0.919	-1.211	-1.052
GoF	1.183	1.350	1.298	1.345	1.183	1.104
Extinction coefficient	0.00067(3)	0.00009(2)	0.000152(12)	0.00120(5)	0.00013(2)	0.000007(12)
[a] $R_1(F)$ for $F_o^2 > 2\sigma(F_o^2)$	0.0218	0.0259	0.0182	0.0204	0.0246	0.0264
[b] $R_w(F_o^2)$	0.0535	0.0624	0.0440	0.0545	0.0613	0.0586

[a] $R_1 = \Sigma||F_o| - |F_c||/\Sigma|F_o|$

[b] $wR_2 = [\Sigma w(F_o^2 - F_c^2)^2/\Sigma w(F_o^2)^2]^{1/2}$; $w = 1/[\sigma^2(F_o^2) + (0.0213P)^2 + 49.5837P]$ for $ZrCr_{0.98(4)}Zn_{21.02(4)}$, $w = 1/[\sigma^2(F_o^2) + (0.0269P)^2 + 188.5081P]$ for $ZrMn_{1.78(10)}Zn_{20.22(10)}$, $w = 1/[\sigma^2(F_o^2) + (0.0101P)^2 + 61.8000P]$ for $ZrFe_2Zn_{20}$, $w = 1/[\sigma^2(F_o^2) + (0.0209P)^2 + 35.6318P]$ for $ZrCo_2Zn_{20}$, $w = 1/[\sigma^2(F_o^2) + (0.0295P)^2 + 29.2981P]$ for $ZrNi_2Zn_{20}$, and $w = 1/[\sigma^2(F_o^2) + (0.0279P)^2 + 54.6030P]$ for $ZrCu_2Zn_{20}$.

Table D.2a. Atomic positions for annealed ZrM_xZn_{22-x} compounds

Atom	Wyckoff position	x	y	z	Occ.	U_{eq} (Å^2)
$ZrCr_{0.98(4)}Zn_{21.02(4)}$						
Zr	8*a*	1/8	1/8	1/8	1.00	0.0053(2)
Zn1	96*g*	0.06111(2)	*x*	0.32068(4)	1.00	0.0162(2)
Zn2	48*f*	0.48717(5)	1/8	1/8	1.00	0.0106(2)
M3 (51(2)%Zn+49(2)%Cr)	16*d*	1/2	1/2	1/2	1.00	0.0071(4)
Zn4	16*c*	0	0	0	1.00	0.0173(3)
$ZrMn_{1.78(10)}Zn_{20.22(10)}$						
Zr	8*a*	1/8	1/8	1/8	1.00	0.0051(5)
Zn1	96*g*	0.06027(5)	*x*	0.32280(7)	1.00	0.0125(3)
Zn2	48*f*	0.48820(9)	1/8	1/8	1.00	0.0078(3)
M3 (89(5)%Mn+11(5)%Zn)	16*d*	1/2	1/2	1/2	1.00	0.0033(7)
Zn4	16*c*	0	0	0	1.00	0.0141(5)
$ZrFe_2Zn_{20}$						
Zr	8*a*	1/8	1/8	1/5	1.00	0.0026(2)
Zn1	96*g*	0.05969(2)	*x*	0.32408(3)	1.00	0.00843(16)
Zn2	48*f*	0.48877(4)	1/8	1/8	1.00	0.00542(17)
Fe3	16*d*	1/2	1/2	1/2	1.00	0.0023(2)
Zn4	16*c*	0	0	0	1.00	0.0109(3)
$ZrCo_2Zn_{20}$						
Zr	8*a*	1/8	1/8	1/8	1.00	0.0030(3)
Zn1	96*g*	0.05987(2)	*x*	0.32373(3)	1.00	0.0088(2)
Zn2	48*f*	0.48841(4)	1/8	1/8	1.00	0.0057(2)
Co3	16*d*	1/2	1/2	1/2	1.00	0.0030(3)
Zn4	16*c*	0	0	0	1.00	0.0113(3)
$ZrNi_2Zn_{20}$						
Zr	8*a*	1/8	1/8	1/8	1.00	0.0048(3)
Zn1	96*g*	0.06023(2)	*x*	0.32305(4)	1.00	0.0111(2)
Zn2	48*f*	0.48817(5)	1/8	1/8	1.00	0.0079(2)
Ni 3	16*d*	1/2	1/2	1/2	1.00	0.0068(4)
Zn4	16*c*	0	0	0	1.00	0.0141(3)
$ZrCu_2Zn_{20}$						
Zr	8*a*	1/8	1/8	1/8	1.00	0.0040(3)
Zn1	96*g*	0.06105(3)	*x*	0.32089(4)	1.00	0.0127(2)
Zn2	48*f*	0.48755(6)	1/8	1/8	1.00	0.0081(2)
Cu3	16*d*	1/2	1/2	1/2	1.00	0.0069(3)
Zn4	16	0	0	0	1.00	0.0154(4)

Table D.3a. Interatomic distances (in Å) for annealed ZrM_xZn_{20-x} compounds

Interatomic distance	**$ZrCr_{0.98(4)}Zn_{21.02(4)}$**	**$ZrMn_{1.78(10)}Zn_{20.22(10)}$**	**$ZrFe_2Zn_{20}$**	**$ZrCo_2Zn_{20}$**	**$ZrNi_{1.62(14)}Zn_{20.38(14)}$**	**$ZrCu_2Zn_{20}$**
Zr environment						
Zr-Zn4 (x4)	3.0572(4)	3.0449(10)	3.0214(5)	3.0110(5)	3.0103(6)	3.0336(6)
Zr-Zn1 (x12)	3.0435(6)	3.0640(10)	3.0627(8)	3.0462(5)	3.0340(6)	3.0231(6)
Zn4 environment						
Zn4-Zn1 (x12)	2.9758(5)	2.9809(10)	2.9692(8)	2.9557(5)	2.9487(6)	2.9542(6)
Zn4-Zr (x2)	3.0572(4)	3.0449(10)	3.0214(5)	3.0110(5)	3.0103(6)	3.0336(6)
M3 environment						
M3-Zn2 (x6)	2.5028(5)	2.4916(10)	2.4720(4)	2.4637(5)	2.4634(6)	2.4831(6)
M3-Zn1 (x6)	2.8109(5)	2.7668(10)	2.7230(8)	2.7195(5)	2.7305(6)	2.7860(6)
Zn2 environment						
Zn2-M3 (x2)	2.5028(5)	2.4916(10)	2.4720(4)	2.4637(5)	2.4634(6)	2.4831(6)
Zn2-Zn1 (x2)	2.6749(7)	2.6620(15)	2.6351(6)	2.6241(5)	2.6254(7)	2.6568(6)
Zn2-Zn2 (x4)	2.7524(7)	2.7191(14)	2.6886(6)	2.6864(5)	2.6905(7)	2.7236(6)
Zn2-Zn1 (x4)	2.8213(6)	2.7916(10)	2.7478(5)	2.7512(5)	2.7582(6)	2.7990(6)
Zn1 environment						
Zn1-Zn1	2.5517(4)	2.5769(10)	2.5779(8)	2.5619(5)	2.5472(4)	2.5344(6)
Zn1-Zn2	2.6749(6)	2.6620(15)	2.6351(6)	2.6241(5)	2.6254(7)	2.6568(6)
Zn1-Zn1 (x2)	2.6318(6)	2.6429(12)	2.6401(5)	2.6276(5)	2.6207(7)	2.6144(6)
Zn1-M3	2.8109(5)	2.7668(10)	2.7230(8)	2.7195(5)	2.7305(6)	2.7860(6)
Zn1-Zn2 (x2)	2.8213(7)	2.7916(10)	2.7578(5)	2.7512(5)	2.7582(6)	2.7990(6)
Zn1-Zn1 (x2)	2.9242(6)	2.8802(12)	2.8351(5)	2.8309(5)	2.8413(6)	2.8982(6)
Zn1-Zn4 (x2)	2.9458(5)	2.9809(10)	2.9692(6)	2.9557(5)	2.9487(6)	2.9542(6)
Zn1-Zr	3.0435(6)	3.0640(10)	3.0627(8)	3.0462(5)	3.0340(6)	3.0231(6)

Table D.1b. Crystallographic parameters for non-annealed ZrM_xZn_{22-x} compounds

Formula	$\mathbf{ZrCr_{1.00(6)}Zn_{21.00(6)}}$	$\mathbf{ZrNi_{1.6(2)}Zn_{20.4(2)}}$	$\mathbf{ZrCu_2Zn_{20}}$	
EDS Composition	-	-	-	
Synthesis	EJ845(non-annealed)	EJ833(non-annealed)	EJ834(non-annealed)	
Space group	$Fd\bar{3}m$	$Fd\bar{3}m$	$Fd\bar{3}m$	
a (Å)	14.1203(15)	13.908(2)	14.011(3)	
V (Å^3)	2815.3(5)	2690.0(7)	2750.2(10)	
Z	8	8	8	
Crystal size (mm^3)	?	0.02 x 0.08 x 0.08	?	
Temperature (K)	295(1)	295(1)	295(1)	
Density (g cm^{-3})	7.090	7.487	7.370	
θ Range (°)	4.08-31.99	4.14-31.91	4.11-31.98	
μ (mm^{-1})	35.471	38.307	37.824	
Data Collection and Refinement				
Collected reflections	12196	11794	10603	
Unique reflections	452	463	442	
R_{int}	0.071	0.072	0.112	
h	$-20 \le h \le 20$	$-21 \le h \le 21$	$-20 \le h \le 20$	
k	$-14 \le k \le 14$	$-14 \le k \le 14$	$-14 \le k \le 14$	
l	$-13 \le l \le 13$	$-13 \le l \le 13$	$-13 \le l \le 13$	
$\Delta\rho_{max}$ (e Å^{-3})	1.007	1.510	0.812	
$\Delta\rho_{min}$ (e Å^{-3})	-0.900	-0.994	-0.760	
GoF	1.128	1.236	1.226	
Extinction coefficient	0.00044(4)	0.00031(4)	0.000191(11)	
[a] $R_1(F)$ for $F_o^2 > 2\sigma(F_o^2)$		0.0239	0.0296	0.0264
[b] $R_w(F_o^2)$	0.0630	0.0829	0.0430	

[a] $R_1 = \Sigma||F_o| - |F_c||/\Sigma|F_o|$

[b] $wR_2 = [\Sigma w(F_o^2 - F_c^2)^2/\Sigma w(F_o^2)^2]^{1/2}$; $w = 1/[\sigma^2(F_o^2) + (0.0366P)^2 + 76.3929P]$ for $ZrCr_{1.00(6)}Zn_{21.00(6)}$, $w = 1/[\sigma^2(F_o^2) + (0.0053P)^2 + 78.4144P]$ for $ZrNi_{1.6(2)}Zn_{20.4(2)}$, and $w = 1/[\sigma^2(F_o^2) + (0.0340P)^2 + 31.8330P]$ for $ZrCu_2Zn_{20}$.

Table D.2b. Atomic positions for non-annealed ZrM_xZn_{22-x} compounds

Atom	Wyckoff position	x	y	z	Occ.	U_{eq} (Å^2)
$ZrCr_{1.00(6)}Zn_{21.0(6)}$						
Zr	8*a*	1/8	1/8	1/8	1.00	0.0099(4)
Zn1	96*g*	0.06115(3)	*x*	0.32057(5)	1.00	0.0208(3)
Zn2	48*f*	0.48719(7)	1/8	1/8	1.00	0.0154(3)
M3 (50(3)%Cr+50(3)%Zn)	16*d*	1/2	1/2	1/2	1.00	0.0117(6)
Zn4	16*c*	0	0	0	1.00	0.0220(4)
$ZrNi_{1.6(2)}Zn_{20.4(2)}$						
Zr	8*a*	1/8	1/8	1/8	1.00	0.0056(3)
Zn1	96*g*	0.06027(3)	*x*	0.32307(5)	1.00	0.0113(2)
Zn2	48*f*	0.48825(6)	1/8	1/8	1.00	0.0077(2)
M3 (78(2)%Ni+22(2)%Zn)	16*d*	1/2	1/2	1/2	1.00	0.0072(6)
Zn4	16*c*	0	0	0	1.00	0.0138(4)
$ZrCu_2Zn_{20}$						
Zr	8*a*	1/8	1/8	1/8	1.00	0.0083(3)
Zn1	96*g*	0.06103(3)	*x*	0.32084(4)	1.00	0.0167(2)
Zn2	48*f*	0.48759(5)	1/8	1/8	1.00	0.0124(2)
Cu3	16*d*	1/2	1/2	1/2	1.00	0.0113(3)
Zn4	16*c*	0	0	0	1.00	0.0197(3)

Table D.3b. Interatomic distances (in Å) for non-annealed ZrM_xZn_{20-x} compounds

Interatomic distance	$\mathbf{ZrCr_{1.00(6)}Zn_{21.00(6)}}$	$\mathbf{ZrNi_{1.6(2)}Zn_{20.4(2)}}$	$\mathbf{ZrCu_2Zn_{20}}$
Zr environment			
Zr-Zn4 (x4)	3.0571(2)	3.0112(6)	3.0335(4)
Zr-Zn1 (x12)	3.0416(7)	3.0347(7)	3.0225(8)
Zn4 environment			
Zn4-Zn1 (x12)	2.9748(7)	2.9493(7)	2.9540(7)
Zn4-Zr (x2)	3.0571(2)	3.0112(6)	3.0335(4)
M3 environment			
M3-Zn2 (x6)	2.5027(7)	2.4640(6)	2.4829(6)
M3-Zn1 (x6)	2.8125(7)	2.7314(7)	2.7863(7)
Zn2 environment			
Zn2-M3 (x2)	2.5027(7)	2.4640(6)	2.4829(4)
Zn2-Zn1 (x2)	2.6760(10)	2.6265(9)	2.6580(9)
Zn2-Zn2 (x4)	2.7519(10)	2.6897(9)	2.7227(8)
Zn2-Zn1 (x4)	2.8223(8)	2.7598(8)	2.7988(7)
Zn1 environment			
Zn1-Zn1	2.5501(6)	2.5463(6)	2.5351(7)
Zn1-Zn2	2.6760(10)	2.6265(9)	2.6580(9)
Zn1-Zn1 (x2)	2.6303(8)	2.6226(9)	2.6129(8)
Zn1-M3	2.8125(7)	2.7314(7)	2.7863(7)
Zn1-Zn2 (x2)	2.8223(8)	2.7598(8)	2.7988(7)
Zn1-Zn1 (x2)	2.9259(8)	2.8418(8)	2.8989(8)
Zn1-Zn4 (x2)	2.9748(7)	2.9493(7)	2.9540(7)
Zn1-Zr	3.0416(7)	3.0112(6)	3.0225(8)

ZrM_xZn_{22-x} (M = Cr-Cu) compounds crystallize in the $ZrZn_{22}$ structure type ($Fd\bar{3}m$ space group).[3] This structure is described as a series of interconnected corner sharing Zr- and M-centered polyhedra shown in Figure D.1. Zr atoms are each coordinated by 16 Zn atoms and M atoms are coordinated by 12 Zn atoms that make bi-capped pentagonal antiprisms. Zr-Zn distances within the 16 coordinate environment range from 3.02-3.03 Å in Cu analogues to 3.04-3.05 Å in the Cr analogues, and M-Zn distances in the bi-capped pentagonal antiprisms range from 2.48-2.79 Å for Cu analogues to 2.50-2.81 Å in Cr analogues. Unit cells parameters, unit cell volumes, and interatomic distances decrease as a function of decreasing transition metal size.

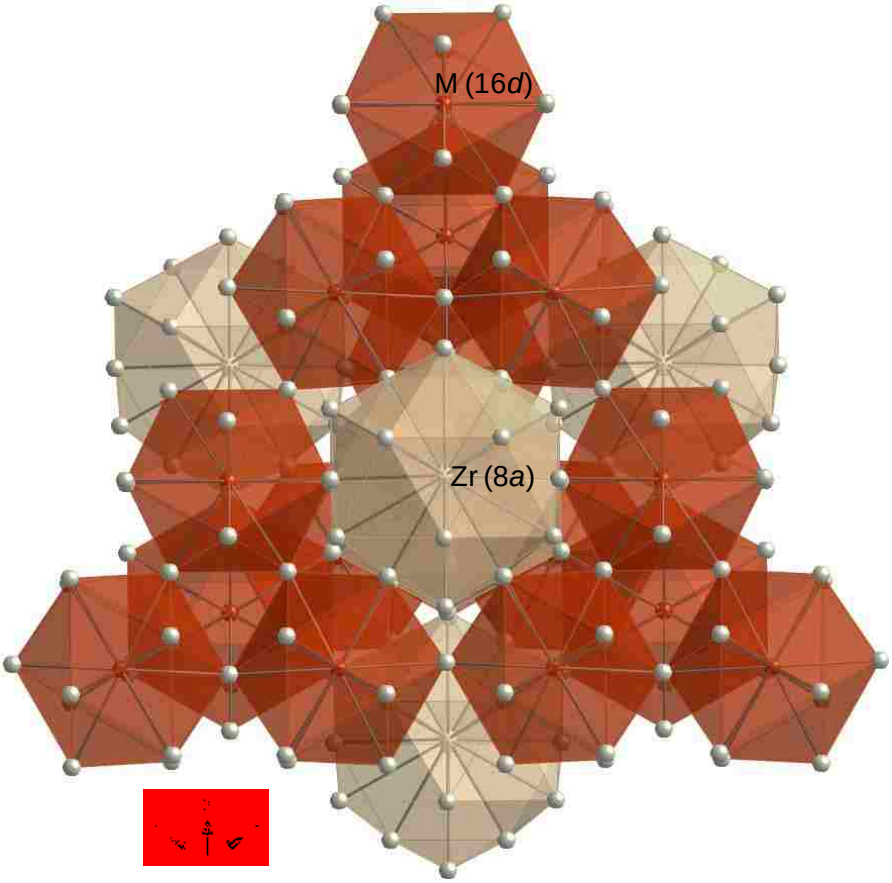

Figure D.1. The ZrM_xZn_{22-x} struture is shown as an interpenetrating network of corner sharing Zr (tan spheres) and M (red spheres) polyhedra. Zr is coordinated to 16 Zn atoms (grey), and M is coordinated to 12 Zn atoms.

Refinement of structural models for Cr and Mn analogues of annealed ZrM_xZn_{22-x} compounds and structural models of Cr and Ni analogues of non-annealed ZrM_xZn_{22-x} compounds reveals M/Zn mixing on the 16*d* position. The mixing in the Cr and Mn analogues of annealed samples is 49(2)% to 51(2) % of Cr to Zn and 89(5) % to 11(5) % of Mn to Zn, respectively, while the mixing in the Cr and Ni analogues of non-annealed samples is 50(3) % to 50(3) % of Cr to Zn and 78(2) % to 22(2) % of Ni to Zn, respectively. These trends indicate that there is an increase of M/Zn mixing on the 16*d* position as a function of increasing M size.

D.3 References

(1) Altomare, A.; Burla, M. C.; Camalli, M.; Cascarano, G. L.; Giacovazzo, C.; Guagliardi, A.; Moliterni, A. G. G.; Polidori, G.; Spagna, R. *J. Appl. Crystallogr.* **1999**, *32*, 115.

(2) Sheldrick, G. *Acta Cryst. A* **2008**, *64*, 112.

(3) Samson, S. *Acta Cryst.* **1961**, *14*, 1229.

APPENDIX E. CONSENT POLICIES

E.1 Elsevier (Approval for Chapter 2)

ELSEVIER LICENSE
TERMS AND CONDITIONS
Jun 05, 2013

This is a License Agreement between Bradford W Fulfer ("You") and Elsevier ("Elsevier") provided by Copyright Clearance Center ("CCC"). The license consists of your order details, the terms and conditions provided by Elsevier, and the payment terms and conditions.

All payments must be made in full to CCC. For payment instructions, please see information listed at the bottom of this form.

Supplier	Elsevier Limited The Boulevard,Langford Lane Kidlington,Oxford,OX5 1GB,UK
Registered Company Number	1982084
Customer name	Bradford W Fulfer
Customer address	Louisiana State University BATON ROUGE, LA 70820
License number	3162660410008
License date	Jun 05, 2013
Licensed content publisher	Elsevier
Licensed content publication	Journal of Solid State Chemistry
Licensed content title	Crystal growth and magnetic properties of*Ln*-Mn-Al (*Ln*=Gd, Yb) compounds of the CaCr2Al10and ThMn12structure types
Licensed content author	Bradford W. Fulfer,Neel Haldolaarachchige,David P. Young,Julia Y. Chan
Licensed content date	October 2012
Licensed content volume number	194
Licensed content issue number	
Number of pages	8
Start Page	143
End Page	150
Type of Use	reuse in a thesis/dissertation
Portion	full article
Format	both print and electronic
Are you the author of this Elsevier article?	Yes
Will you be translating?	No
Order reference number	
Title of your thesis/dissertation	Crystal Growth and an Investigation of Structural Stability: Synthesis, Structure, and Physical Properties of Intermetallic Aluminides and Gallides
Expected completion date	Jul 2013

Estimated size (number of pages)	100
Elsevier VAT number	GB 494 6272 12
Permissions price	0.00 USD
VAT/Local Sales Tax	0.0 USD / 0.0 GBP
Total	0.00 USD
Terms and Conditions	

INTRODUCTION

1. The publisher for this copyrighted material is Elsevier. By clicking "accept" in connection with completing this licensing transaction, you agree that the following terms and conditions apply to this transaction (along with the Billing and Payment terms and conditions established by Copyright Clearance Center, Inc. ("CCC"), at the time that you opened your Rightslink account and that are available at any time at http://myaccount.copyright.com).

GENERAL TERMS

2. Elsevier hereby grants you permission to reproduce the aforementioned material subject to the terms and conditions indicated.

3. Acknowledgement: If any part of the material to be used (for example, figures) has appeared in our publication with credit or acknowledgement to another source, permission must also be sought from that source. If such permission is not obtained then that material may not be included in your publication/copies. Suitable acknowledgement to the source must be made, either as a footnote or in a reference list at the end of your publication, as follows:

"Reprinted from Publication title, Vol /edition number, Author(s), Title of article / title of chapter, Pages No., Copyright (Year), with permission from Elsevier [OR APPLICABLE SOCIETY COPYRIGHT OWNER]." Also Lancet special credit - "Reprinted from The Lancet, Vol. number, Author(s), Title of article, Pages No., Copyright (Year), with permission from Elsevier."

4. Reproduction of this material is confined to the purpose and/or media for which permission is hereby given.

5. Altering/Modifying Material: Not Permitted. However figures and illustrations may be altered/adapted minimally to serve your work. Any other abbreviations, additions, deletions and/or any other alterations shall be made only with prior written authorization of Elsevier Ltd. (Please contact Elsevier at permissions@elsevier.com)

6. If the permission fee for the requested use of our material is waived in this instance, please be advised that your future requests for Elsevier materials may attract a fee.

7. Reservation of Rights: Publisher reserves all rights not specifically granted in the combination of (i) the license details provided by you and accepted in the course of this licensing transaction, (ii) these terms and conditions and (iii) CCC's Billing and Payment terms and conditions.

8. License Contingent Upon Payment: While you may exercise the rights licensed

immediately upon issuance of the license at the end of the licensing process for the transaction, provided that you have disclosed complete and accurate details of your proposed use, no license is finally effective unless and until full payment is received from you (either by publisher or by CCC) as provided in CCC's Billing and Payment terms and conditions. If full payment is not received on a timely basis, then any license preliminarily granted shall be deemed automatically revoked and shall be void as if never granted. Further, in the event that you breach any of these terms and conditions or any of CCC's Billing and Payment terms and conditions, the license is automatically revoked and shall be void as if never granted. Use of materials as described in a revoked license, as well as any use of the materials beyond the scope of an unrevoked license, may constitute copyright infringement and publisher reserves the right to take any and all action to protect its copyright in the materials.

9. Warranties: Publisher makes no representations or warranties with respect to the licensed material.

10. Indemnity: You hereby indemnify and agree to hold harmless publisher and CCC, and their respective officers, directors, employees and agents, from and against any and all claims arising out of your use of the licensed material other than as specifically authorized pursuant to this license.

11. No Transfer of License: This license is personal to you and may not be sublicensed, assigned, or transferred by you to any other person without publisher's written permission.

12. No Amendment Except in Writing: This license may not be amended except in a writing signed by both parties (or, in the case of publisher, by CCC on publisher's behalf).

13. Objection to Contrary Terms: Publisher hereby objects to any terms contained in any purchase order, acknowledgment, check endorsement or other writing prepared by you, which terms are inconsistent with these terms and conditions or CCC's Billing and Payment terms and conditions. These terms and conditions, together with CCC's Billing and Payment terms and conditions (which are incorporated herein), comprise the entire agreement between you and publisher (and CCC) concerning this licensing transaction. In the event of any conflict between your obligations established by these terms and conditions and those established by CCC's Billing and Payment terms and conditions, these terms and conditions shall control.

14. Revocation: Elsevier or Copyright Clearance Center may deny the permissions described in this License at their sole discretion, for any reason or no reason, with a full refund payable to you. Notice of such denial will be made using the contact information provided by you. Failure to receive such notice will not alter or invalidate the denial. In no event will Elsevier or Copyright Clearance Center be responsible or liable for any costs, expenses or damage incurred by you as a result of a denial of your permission request, other than a refund of the amount(s) paid by you to Elsevier and/or Copyright Clearance Center for denied permissions.

LIMITED LICENSE

The following terms and conditions apply only to specific license types:

15. **Translation**: This permission is granted for non-exclusive world **English** rights only unless your license was granted for translation rights. If you licensed translation rights you

may only translate this content into the languages you requested. A professional translator must perform all translations and reproduce the content word for word preserving the integrity of the article. If this license is to re-use 1 or 2 figures then permission is granted for non-exclusive world rights in all languages.

16. **Website**: The following terms and conditions apply to electronic reserve and author websites:
Electronic reserve: If licensed material is to be posted to website, the web site is to be password-protected and made available only to bona fide students registered on a relevant course if:
This license was made in connection with a course,
This permission is granted for 1 year only. You may obtain a license for future website posting,
All content posted to the web site must maintain the copyright information line on the bottom of each image,
A hyper-text must be included to the Homepage of the journal from which you are licensing at http://www.sciencedirect.com/science/journal/xxxxx or the Elsevier homepage for books at http://www.elsevier.com , and
Central Storage: This license does not include permission for a scanned version of the material to be stored in a central repository such as that provided by Heron/XanEdu.

17. **Author website** for journals with the following additional clauses:

All content posted to the web site must maintain the copyright information line on the bottom of each image, and the permission granted is limited to the personal version of your paper. You are not allowed to download and post the published electronic version of your article (whether PDF or HTML, proof or final version), nor may you scan the printed edition to create an electronic version. A hyper-text must be included to the Homepage of the journal from which you are licensing at http://www.sciencedirect.com/science/journal/xxxxx . As part of our normal production process, you will receive an e-mail notice when your article appears on Elsevier's online service ScienceDirect (www.sciencedirect.com). That e-mail will include the article's Digital Object Identifier (DOI). This number provides the electronic link to the published article and should be included in the posting of your personal version. We ask that you wait until you receive this e-mail and have the DOI to do any posting.

Central Storage: This license does not include permission for a scanned version of the material to be stored in a central repository such as that provided by Heron/XanEdu.

18. **Author website** for books with the following additional clauses:
Authors are permitted to place a brief summary of their work online only.
A hyper-text must be included to the Elsevier homepage at http://www.elsevier.com . All content posted to the web site must maintain the copyright information line on the bottom of each image. You are not allowed to download and post the published electronic version of your chapter, nor may you scan the printed edition to create an electronic version.

Central Storage: This license does not include permission for a scanned version of the material to be stored in a central repository such as that provided by Heron/XanEdu.

19. **Website** (regular and for author): A hyper-text must be included to the Homepage of the journal from which you are licensing at http://www.sciencedirect.com/science/journal/xxxxx. or for books to the Elsevier homepage at http://www.elsevier.com

20. **Thesis/Dissertation**: If your license is for use in a thesis/dissertation your thesis may be submitted to your institution in either print or electronic form. Should your thesis be published commercially, please reapply for permission. These requirements include permission for the Library and Archives of Canada to supply single copies, on demand, of the complete thesis and include permission for UMI to supply single copies, on demand, of the complete thesis. Should your thesis be published commercially, please reapply for permission.

21. **Other Conditions**:

v1.6

If you would like to pay for this license now, please remit this license along with your payment made payable to "COPYRIGHT CLEARANCE CENTER" otherwise you will be invoiced within 48 hours of the license date. Payment should be in the form of a check or money order referencing your account number and this invoice number RLNK501036850.
Once you receive your invoice for this order, you may pay your invoice by credit card. Please follow instructions provided at that time.

Make Payment To:
Copyright Clearance Center
Dept 001
P.O. Box 843006
Boston, MA 02284-3006

For suggestions or comments regarding this order, contact RightsLink Customer Support: customercare@copyright.com or +1-877-622-5543 (toll free in the US) or +1-978-646-2777.

Gratis licenses (referencing $0 in the Total field) are free. Please retain this printable license for your reference. No payment is required.

E.2 American Chemical Society (Approval for Chapter 3)

Title:	Synthesis, Structure, and Magnetic and Electrical Properties of Yb(Mn,M)xAl12–x (M = Fe, Ru; x ≤ 2.5) Phases
Author:	Bradford W. Fulfer, Jacob D. McAlpin, Neel Haldolaarachchige, David P. Young, and Julia Y. Chan
Publication:	Crystal Growth and Design
Publisher:	American Chemical Society
Date:	Apr 1, 2013
Copyright © 2013, American Chemical Society	

Logged in as:
Bradford Fulfer

PERMISSION/LICENSE IS GRANTED FOR YOUR ORDER AT NO CHARGE

This type of permission/license, instead of the standard Terms & Conditions, is sent to you because no fee is being charged for your order. Please note the following:

- Permission is granted for your request in both print and electronic formats, and translations.
- If figures and/or tables were requested, they may be adapted or used in part.
- Please print this page for your records and send a copy of it to your publisher/graduate school.
- Appropriate credit for the requested material should be given as follows: "Reprinted (adapted) with permission from (COMPLETE REFERENCE CITATION). Copyright (YEAR) American Chemical Society." Insert appropriate information in place of the capitalized words.
- One-time permission is granted only for the use specified in your request. No additional uses are granted (such as derivative works or other editions). For any other uses, please submit a new request.

E.3 American Physical Society (Approval for Appendix B)

Bradford Fulfer <bfulfe1@tigers.lsu.edu>

Reprint Permission

Associate Publisher <assocpub@aps.org> Thu, Jun 20, 2013 at 9:30 AM
To: Bradford Fulfer <bfulfe1@tigers.lsu.edu>

Dear Mr. Fulfer,

As the author of the APS paper, you have the right to use figures, tables, graphs, etc. in subsequent publications using files prepared and formatted by you or the APS-prepared versions. The appropriate bibliographic citation must be included.

Best wishes,

Alex Menendez

Publications Marketing Coordinator

American Physical Society

VITA

Bradford Wesley Fulfer was born in 1986 to Kenneth Fulfer and Cindy Fulfer in the city of Harlingen, Texas. He is the older of two children (Bryant Fulfer, brother). Bradford graduated from Cypress Falls High School in Houston, Texas in May of 2004. He then attended Abilene Christian University in Abilene, Texas from August of 2004 until May of 2008, where he graduated with his Bachelor of Science degree in Chemistry. In January of 2010, he joined the research group of Dr. Julia Y Chan at Louisiana State University and Agricultural and Mechanical College.

While at LSU, Bradford has attended several national scientific meetings. In the summer of 2011 he gave a talk at the national meeting of the American Crystallographic Association in New Orleans. In the summer of 2013, Bradford attended the Gordon Research Conference on Solid State Chemistry at Colby Sawyer College in New Hampshire, where he presented a research poster. Finally, in the spring of 2013 he presented a research poster at the national meeting of the American Chemical Society in New Orleans, Louisiana. He has received a teaching award for instructing CHEM3493 in the spring of 2013. He has taught one semester of general chemistry laboratory and three semesters of physical chemistry laboratory. Additionally, he has performed multiple demonstrations of chemistry experiments in Baton Rouge and the immediate areas for children in grades K-12.

In August of 2013, Bradford will graduate and be awarded with a Doctor of Chemistry degree in Chemistry.